Carrier lifetime instabilities in the bulk and at the surfaces of crystalline silicon solar cells triggered by fast-firing processes

Von der Fakultät für Mathematik und Physik
der Gottfried Wilhelm Leibniz Universität Hannover

zur Erlangung des akademischen Grades
Doktor der Naturwissenschaften
Dr. rer. nat.

genehmigte Dissertation von

M. Sc. Michael Winter
geboren am 27.11.1990 in Hildesheim

2024

Referent: Prof. Dr. Jan Schmidt
Korreferent: Prof. Dr. Tobias Wietler
Korreferent: Prof. Dr. Michael Seibt
Tag der Promotion: 27.03.2024

Kurzzusammenfassung

Instabilitäten der Ladungsträgerlebensdauer in kristallinen Silizium-Solarzellen unter Beleuchtung beeinträchtigen die Langzeitstabilität von Photovoltaik-Modulen im Hinblick auf den stetig steigenden Wirkungsgrad der in modernen Modulen verwendeten Solarzellen. In dieser Arbeit wird die Degradation und Regeneration der Ladungsträgerlebensdauer – sowohl im Volumen als auch an den Oberflächen verschiedener kristalliner Siliziummaterialien und daraus hergestellter Solarzellen – nach einem sogenannten Feuerschritt in einem Durchlaufofen (fast-firing) untersucht. Es wird gezeigt, dass der Feuerschritt der Auslöser von Degradationseffekten bei Beleuchtung ist. Das Feuern ist aber auch ein wichtiger Schritt bei der Kontaktbildung von siebgedruckten Kontakten, der heute vorherrschenden Metallisierungstechnik in der Solarzellproduktion.

Unabhängig vom Feuerschritt in einem Standard-Durchlaufofen wird die Volumen-Lebensdauer von Bor-dotiertem Czochralski-Silizium (Cz-Si:B) durch die lichtinduzierte Aktivierung eines Bor-Sauerstoff-Defekts (BO-Defekt) dominiert. Gallium-dotiertes Czochralski-Silizium (Cz-Si:Ga) und nach dem Float-Zone-Verfahren hergestelltes Bor-dotiertes Silizium (float-zone silicon, FZ-Si:B) – beide nicht anfällig für BO-verursachte Degradation – zeigen jedoch eine stark temperaturabhängige Degradation der Volumen-Lebensdauer bei Beleuchtung. Der sich einstellende Gleichgewichtszustand zwischen aktiviertem (rekombinationsaktivem) und deaktiviertem (rekombinationsinaktivem) Zustand des verantwortlichen Defekts ist abhängig von der Temperatur und die Aktivierung und Deaktivierung des Defekts sind reversible Prozesse. Es wird gezeigt, dass die Eindiffusion von Wasserstoff aus wasserstoffreichem Siliziumnitrid (SiN_y:H), das zur Oberflächenpassivierung und als Antireflexschicht eingesetzt wird, in das Silizium-Volumen während des Feuerschrittes eine Schlüsselrolle für die sogenannte „light- and elevated-temperature-induced degradation“ (LeTID) in allen drei Materialien – das sind Cz-Si:B, Cz-Si:Ga und FZ-Si:B – spielt. Experimente auf FZ-Si:B-Material, das im Allgemeinen sehr defektarm ist, deuten darüber hinaus darauf hin, dass es neben Wasserstoff einen weiteren Teilnehmer an der Defektreaktion von LeTID gibt.

LeTID wird auch auf sogenannten „polycrystalline silicon on oxide” (POLO) back-junction (BJ) Solarzellen mit einer Cz-Si:Ga-Basis beobachtet. Die relative Degradation des Wirkungsgrades η von maximal nur $2\%_{\mathrm{rel}}$ unter Beleuchtung bei 140 °C und einer Beleuchtungsintensität äquivalent zu einer Sonne zeigt jedoch, dass POLO BJ-Zellen bemerkenswert stabil gegenüber lichtinduzierter Degradation sind. Durch längere Beleuchtung bei erhöhten Temperaturen ist eine anteilige dauerhafte Deaktivierung des LeTID-Defekts möglich.

Zusätzlich zur Degradation im Silizium-Volumen werden thermisch induzierte Instabilitäten von Phosphor-dotierten POLO-Passivierungsschichten nach einem Feuerschritt beschrieben. Die Degradation und die anschließende Regeneration der Oberflächen-Passivierung – beschrieben durch die Sättigungsstromdichte J_0 – ist mit ho-

her Wahrscheinlichkeit korreliert mit der Wasserstoffpassivierung von Grenzflächenzuständen.

Abstract

Carrier lifetime instabilities in crystalline silicon solar cells under illumination affect the long-term stability of photovoltaic modules in view of the steadily increasing conversion efficiency of the solar cells used in state-of-the-art modules. This thesis examines carrier lifetime degradation and regeneration – both in the bulk and at the surfaces of different crystalline silicon materials and solar cells made thereof – after a fast-firing step has been applied in a conveyor belt furnace. It is shown that fast-firing triggers degradation effects under illumination. However, fast-firing is also a key step in the contact formation of screen-printed contacts, which is the dominating metalization technique applied today in the solar cell production.

Independent of fast-firing in a standard conveyor belt furnace, the bulk carrier lifetime of boron-doped Czochralski-grown silicon (Cz-Si:B) is dominated by the light-induced activation of a boron-oxygen (BO) defect. Gallium-doped Czochralski-grown silicon (Cz-Si:Ga) and boron-doped float-zone silicon (FZ-Si:B) – both not prone to BO-related degradation –, however, show a strongly temperature-dependent degradation of the bulk lifetime activated under simultaneous illumination. The equilibrium state establishing between activated (recombination-active) and deactivated (recombination-inactive) state of the defect is dependent on the temperature and the activation and deactivation of the defect are reversible processes. It is shown that the in-diffusion of hydrogen from hydrogen-rich silicon nitride layers (SiN_y:H), used for the surface passivation and as antireflection coating, into the silicon bulk during fast firing plays a key role for the so-called "light- and elevated-temperature-induced degradation" (LeTID) in all three materials – namely Cz-Si:B, Cz-Si:Ga, and FZ-Si:B. Experiments on the very defect-lean FZ-Si:B material furthermore suggest a second participant in the defect reaction of LeTID besides hydrogen.

LeTID is also observed on "polycrystalline silicon on oxide" (POLO) backjunction (BJ) solar cells fabricated on Cz-Si:Ga. The maximum relative degradation extent of the conversion efficiency η of only $2\%_{\mathrm{rel}}$ at 140 °C and 1 sun, however, shows that POLO BJ cells are remarkably stable regarding light-induced degradation. Through prolonged illumination at elevated temperatures a partial permanent deactivation of the LeTID defect is possible.

In addition to bulk degradation, thermally-induced instabilities of the phosphorus-doped POLO passivation layers after fast-firing are discovered. The degradation and the following regeneration of the surface passivation quality – described by the saturation current density J_0 – is correlated with high probability with the hydrogen passivation of interface states.

Schlagwörter: Degradation, Gallium, Ladungsträgerlebensdauer, Langzeitstabilität, LeTID, Silizium, Solarzelle, Wasserstoff.

Keywords: degradation, gallium, carrier lifetime, long-term stability, LeTID, silicon, solar cell, hydrogen.

Contents

1 Introduction

The transformation of our energy system towards 100 percent renewable energy sources for our primary energy consumption is one of the biggest challenges of our generation. With the gradual elimination of fossil energy sources, such as oil, coal, and gas, the demand for electrically generated energy will increase exponentially in the next decades [1]. Already the cheapest alternative to generate electrical power in a significant majority of countries worldwide [2], photovoltaics (PV) will be one of the key technologies for the necessary transformation of our energy system. The efficient and sustainable use of resources to produce high-performance and long-term stable (25-40 years) PV modules will be required of the solar industry [3].

As the conversion efficiency steadily increases, the carrier lifetime (i.e., the average time span free electron-hole pairs exist before they recombine) in the bulk of solar cells has become a crucial factor. Furthermore, the long-term stability of the carrier lifetime depends on the passivation of existing defects (e.g., non-intentional impurities or impurity complexes which affect the carrier lifetime) in the silicon base material. Carrier lifetime instabilities in the bulk of solar cells due to defect formation under illumination (i.e., light-induced degradation, LID) has been an important field of PV research for decades. In addition, the long-term stability of surface passivation quality has attracted more and more attention only recently.

Fast-firing is a key step in the contact formation of screen-printed contacts, which is the dominating metalization technique applied in the solar industry. This thesis aims at improving the understanding of firing-triggered carrier lifetime degradation and regeneration behavior, both in the bulk and at the surfaces of different crystalline silicon materials – namely boron-doped Czochralski-grown silicon (Cz-Si:B), gallium-doped Cz-Si (Cz-Si:Ga), and boron-doped float-zone silicon (FZ-Si:B) – and of solar cells made thereof. The focus is on investigating the impact of different experimental conditions, which are the temperature during illumination and the illumination intensity, on the degradation behavior, and on how critical parameters of the fast-firing step and the deposition of various surface passivation layers affect the degradation behavior and the maximum degradation extent. It is demonstrated that the in-diffusion of hydrogen into the silicon bulk plays a key role in all our experiments.

1.1 Status of research at the beginning of this thesis

Prior to starting the work on this thesis in 2018, the two most prominent defects known to form under illumination and affect the carrier lifetime in monocrystalline p-type silicon were the iron-boron (FeB) pair dissociation [4, 5] and the boron-oxygen (BO) defect formation [6–9]. After passivated emitter and rear cells (PERC) with screen printed and fired contacts were introduced into the solar cell production, a new type of defect causing a so-called "light- and elevated-temperature-induced

degradation" (LeTID) of the bulk carrier lifetime and hence solar cell efficiency has become a steadily growing area of research. The effect was first observed under illumination at elevated temperatures higher than 50 °C on PERC solar cells made from block-cast multicrystalline silicon (mc-Si) passivated at the rear side with a stack consisting of aluminum oxide (AlO_x) and silicon nitride (SiN_y) and on solar cells with a full-area aluminum back surface field (Al-BSF) [10–12]. After complete degradation with demonstrated power losses above 10%, a complete regeneration of the cell performance was observed under prolonged illumination, e.g., at 95 °C for 700 h [12]. The high-temperature firing step used for the screen-printed and fired metal contacts was identified to trigger the LeTID effect [13, 14].
Shortly before this thesis, there have been publications indicating that a similar defect could exist in monocrystalline silicon materials (mono-Si) as well. Whereas Fertig et al. [15] reported a power loss of up to 6% on BO-stabilized Cz-Si:B PERC cells at 75 °C under charge carrier injection equivalent to an illumination at $1\,\mathrm{kW\,m^{-2}}$, Chen et al. [16] observed a similar degradation and regeneration of the carrier lifetime within 200 h on mc-Si:B and Cz-Si:B wafers under annealing in the dark at 175 °C. Comparing certain defect characteristics with carrier-induced degradation on mc-Si:B, the authors concluded that LeTID can occur on Cz-Si:B as well, but is masked by BO-related degradation. On FZ-Si:B, which is usually not prone to BO-related degradation due to a significantly lower oxygen concentration, a degradation and regeneration of the carrier lifetime within only 10 h has been reported under one-sun equivalent illumination ($1\,\mathrm{kW\,m^{-2}}$) at 75 °C after applying a high-temperature firing step with a set-peak temperature >800 °C in the presence of symmetrically deposited SiN_y or AlO_x/SiN_y passivation layers on both wafer surfaces [17, 18].
In many publications on both mc-Si and mono-Si materials the hypothesis of an hydrogen involvement in the defect reaction was discussed [13, 14, 16, 17, 19]. Interestingly, Kersten et al. [20] reported the possibility of a temporary deactivation of the LeTID effect on boron-doped mc-Si (mc-Si:B) solar cells through low-temperature illumination for 24 h at 25 °C.
In the year 2017, 95 percent of the world market share of silicon wafers used in PV production were boron-doped mono-Si and mc-Si materials [21]. However, during the work on this thesis and within only a few years, gallium has overtaken boron as the dominant doping element in the production of p-type silicon and is now dominating the p-type mono-Si market. In 2023, boron as dopant for p-type material disappears according to data of the International Technology Roadmap for PV [22]. This very fast transition can be attributed to the absence of BO-related degradation of the carrier lifetime [23].
Shortly before this thesis, "polycrystalline silicon on oxide" (POLO) layers were rediscovered and attracted great attention to realize carrier-selective passivating contacts for solar cells. First proposals to use polycrystalline silicon(poly-Si) in solar cell production date back more than 30 years [24]. POLO contacts combine excellent passivation quality with saturation current densities J_0 down to $0.6\,\mathrm{fA/cm^2}$, as reported on planar test structures [25, 26], with very low contact resistivities ($0.6\,\mathrm{m\Omega\,cm^2}$ for n^+ POLO junctions) [27].
Degradation of the surface passivation quality under illumination after a fast-firing step has not been an area of particular interest for a long time. Veith et al. [28] showed that the surface passivation quality of atomic-layer-deposited (ALD) AlO_x

and of AlO_x capped by plasma-enhanced chemical vapor deposited (PECVD) SiN_y changes under both annealing and illumination treatments. Furthermore, the stability of AlO_x passivation to fast-firing can be significantly improved by a PECVD SiN_y capping layer. Before this thesis, only Sperber et al. have conducted extensive research on the long-term stability of fired dielectric passivation schemes. Sperber et al. [29–31] observed surface-related degradation of the carrier lifetime at temperatures ranging from 80 to 250 °C under both illumination or in the dark using single-layer hydrogen-rich SiN_y:H and stacks consisting of silicon oxide SiO_2 or hydrogen-rich aluminum oxide AlO_x, respectively, capped by SiN_y:H. Furthermore, Sperber et al. [29, 30] observed a regeneration of the surface passivation quality at 250 °C after complete degradation at the same conditions. By conducting corona charging and capacitance voltage measurements as well as a chemical re-passivation, the authors attributed the degradation/regeneration behavior of SiN_y:H- and SiO_2/SiN_y:H-passivated samples to changes in the chemical passivation while the field effect passivation remained rather unchanged [30, 31]. However, an AlO_x-interlayer significantly slows down surface-related degradation, which, according to Sperber et al. [30], could be related to a different band structure.

1.2 Brief overview of the thesis

Chapter 2: Fundamentals of carrier recombination in silicon
Chapter 2 discusses the recombination of excess carriers (i.e., electron-hole pairs) with special attention to the various recombination processes existing in semiconductors. This thesis focuses on instabilities of the carrier lifetime through activation, deactivation, and passivation of existing defects in the bulk and at the surfaces of crystalline silicon. The concepts of the capture time constant ratio and the effective defect concentration to characterize bulk defects and the characterization of the surface passivation quality via the saturation current density of a pseudo-emitter are introduced in this chapter.

Chapter 3: Characterization methods
Chapter 3 describes the characterization techniques applied in this thesis to measure the carrier lifetime, namely the photoconductance decay (PCD) method and the spatially-resolved photoluminescence (PL) technique. Furthermore, a contactless technique to measure the resistivity of silicon lifetime samples based on eddy-current measurements is introduced. The chapter concludes with the current voltage (IV) measurement techniques needed to characterize solar cells. It includes a brief description of the operating principle of a backjunction solar cell examined in this thesis.

Chapter 4: Light- and elevated-temperature-induced degradation in boron-doped Czochralski-silicon
In Chapter 4, we examine the impact of a firing-triggered degradation phenomenon on the carrier lifetime in Cz-Si:B by separating it from a parallel occurring degradation due to the formation of the boron-oxygen defect, a defect well-known in oxygen-rich boron-doped materials such as Cz-Si:B. Through variations of the process parameters, experimental conditions, and by comparison with other materials

(i.e., mc-Si:B) and non-fired reference samples, the effect of the additional firing-triggered defect can be extracted.

Chapter 5: Light- and elevated-temperature-induced degradation in gallium-doped Czochralski-silicon
During the work on this thesis, Cz-Si:Ga has overtaken boron-doped materials (both Cz-Si:B and mc-Si:B) as the dominant p-type base material in the solar cell production. Until the beginning of this thesis, Cz-Si:Ga had been believed to not be affected by light-induced degradation due to the absence of boron-oxygen-related degradation. However, on fired lifetime samples, Chapter 5 describes a strongly temperature-dependent degradation of the carrier lifetime due to the formation of a bulk defect. Through variations of key process parameters – such as the peak firing temperature and the band velocity during fast-firing as well as the deposition of different SiN_y layers as hydrogen source prior to firing – the impact of hydrogen on the maximum degradation extent is quantified. The hydrogen-related formation and passivation of the defect is characterized, including the determination of the corresponding activation energy. The defect characteristics are compared with the activation of a similar defect in FZ-Si:B as a defect-lean reference material.

Chapter 6: Light- and elevated-temperature-induced degradation in poly-Si on oxide backjunction solar cells
Chapter 6 examines to what extent lifetime instabilities described in the previous chapter in Cz-Si:Ga affect the performance of solar cells. The solar cell type used for this study has been developed at ISFH and applies poly-Si passivating contacts at the rear side of a backjunction (BJ) solar cell. Through IV measurements in between illumination at different temperatures, a degradation of the energy conversion efficiency η is observed. These changes of η are ascribed to changes in the defining cell parameters, namely the open-circuit voltage V_{oc}, the short-circuit current density J_{sc}, and the fill factor FF. We show an identical degradation behavior on cell level as we have examined in detail on lifetime samples in the previous chapter.

Chapter 7: Degradation and regeneration of Poly-Si on oxide surface passivation quality
Shortly before the beginning of this thesis, poly-Si layers have attracted great attention to realize carrier-selective passivating contacts in solar cells. The implementation in solar cells with screen-printed and fired contacts, however, requires a high-temperature fast-firing step. Chapter 7 investigates the stability of in-situ doped n^+ POLO passivation layers to fast-firing by long-term annealing experiments under illumination and in the dark. The carrier lifetime over a wide range of the excess carrier concentration Δn and the extraction of the saturation current density J_0 as a measure of the surface passivation quality are used to characterize the lifetime instability. To identify the impact of the fast-firing step and localize the cause of the lifetime instability, a variety of samples with different thermal histories are examined.

2 Fundamentals of carrier recombination in silicon

The most important quantity in characterizing the electronic quality of crystalline silicon materials is the carrier lifetime, i.e., the average time span free electron-hole pairs exist before they recombine. In this thesis, we will use the carrier lifetime as a parameter to quantify defect activation processes in the bulk and at the surfaces of silicon wafers.

In thermal equilibrium, the mass-action law of electron concentration n_0 and hole concentration p_0 holds

$$n_0 \times p_0 = n_\mathrm{i}^2, \tag{2.1}$$

with n_i being the intrinsic carrier concentration in silicon. A disturbance of this equilibrium, e.g., by illumination with photon energies high enough to excite electrons from the valence band into the conduction band ($E > E_\mathrm{g}$, with E_g being the energy of the silicon band gap), generates additional carriers. As soon as the illumination is terminated, the equilibrium described in Eq. (2.1) is restored by recombination of electrons and holes. The net recombination rate U, defined as the difference between the total recombination rate U_tot and the thermal generation rate G_th, $U \equiv U_\mathrm{tot} - G_\mathrm{th}$, is given by the rate equation:

$$\frac{\partial \Delta n(t)}{\partial t} = -U(\Delta n, n_0, p_0), \tag{2.2}$$

with $\Delta n(t)$ being the excess carrier concentration at the time t. Note that U is always the sum of several recombination rates of different recombination processes and that in general U is dependent on Δn. The ratio of Δn and U defines the effective carrier lifetime:

$$\tau_\mathrm{eff}(\Delta n, n_0, p_0) \equiv \frac{\Delta n}{U(\Delta n, n_0, p_0)}. \tag{2.3}$$

The different recombination processes that add up to the recombination rate U and how these contribute to $\tau_\mathrm{eff}(\Delta n)$ will be outlined in the following. Furthermore, the concepts of the capture time constant ratio and the effective defect concentration to characterize bulk defects and the characterization of the surface passivation quality via the saturation current density are introduced.

2.1 Intrinsic recombination

Intrinsic recombination denotes a material property that cannot be avoided. Thus, the intrinsic lifetime τ_{intr} derived from Eq. (2.3) represents the limit of the carrier lifetime in silicon. Intrinsic recombination is the sum of radiative and Auger recombination.

Radiative recombination denotes the band-to-band recombination of an electron-hole pair under generation of a photon with the minimum energy corresponding to the band gap of silicon $E_{\mathrm{g}} = 1.12\,\mathrm{eV}$ at 300 K. It is the inverse process of the optical generation of electron-hole pairs (i.e., through illumination). The rate of radiative recombination U_{rad} depends on the electron and hole concentrations n and p, and on the coefficient of radiative recombination B_{rad}:

$$U_{\mathrm{rad}} = B_{\mathrm{rad}} \left(np - n_{\mathrm{i}}^2 \right) . \tag{2.4}$$

According to Eq. (2.3), U_{rad} can be translated into a corresponding lifetime of radiative recombination

$$\tau_{\mathrm{rad}} = \frac{\Delta n}{B_{\mathrm{rad}} \left(np - n_{\mathrm{i}}^2 \right)} = \frac{1}{B_{\mathrm{rad}} \left(n_0 + p_0 + \Delta n \right)}, \tag{2.5}$$

assuming $n = n_0 + \Delta n$ and $p = p_0 + \Delta n$ for the total electron and hole concentrations, respectively, and Eq. (2.1). Trupke et al. [32] determined the coefficient of radiative recombination at 300 K to be $B_{\mathrm{rad}} = 4.73 \times 10^{-15}\,\mathrm{cm}^3\,\mathrm{s}^{-1}$.

Auger recombination is a three-particle process. The energy released by the recombination of an electron-hole pair is passed to another electron (eeh process) or hole (ehh process) in the conduction band or valence band, respectively. The energy is released as phonons by interaction with the crystal lattice (thermalization). The Auger recombination rate U_{Auger} is either proportional to n^2p (eeh process) or np^2 (ehh process) and can be written as

$$U_{\mathrm{Auger}} = C_{\mathrm{n}} \left(n^2 p - n_0^2 p_0 \right) + C_{\mathrm{p}} \left(np^2 - n_0 p_0^2 \right) , \tag{2.6}$$

with C_{n} and C_{p} being the Auger coefficients of the eeh- and the ehh-processes, respectively. Equation (2.6) assumes quasi-free non-interacting carrier. However, the Auger recombination has been found to have a significantly higher impact on the carrier lifetime at lower carrier concentrations. Hangleiter and Häcker [33] proposed enhancement factors g_{eeh} and g_{ehh} taking into account Coulomb interactions and shielding effects, resulting in the new Auger coefficients $C_{\mathrm{n}}^* = g_{\mathrm{eeh}} \times C_{\mathrm{n}}$ and $C_{\mathrm{p}}^* = g_{\mathrm{ehh}} \times C_{\mathrm{p}}$. Later, empirical parametrizations of the enhancement factors were derived for a wide temperature range between 70 K and 400 K [34, 35].

Intrinsic recombination: The rate of intrinsic recombination U_{intr} is the sum of radiative and Auger recombination rate U_{rad} and U_{Auger}. The derived intrinsic lifetime is given by

$$\frac{1}{\tau_{\text{intr}}} = \frac{1}{\tau_{\text{rad}}} + \frac{1}{\tau_{\text{Auger}}}. \tag{2.7}$$

In this thesis, an empirical parametrization of τ_{intr} at 300 K by Richter et al. [36] is used. It is based on lifetime measurements on a large number of different silicon-wafers of various doping concentrations and surface passivation schemes. Figure 2.1 shows $\tau_{\text{intr}}(\Delta n)$ for four different base resistivities between 0.5 Ω cm and 4.0 Ω cm for p-type silicon at 300 K.

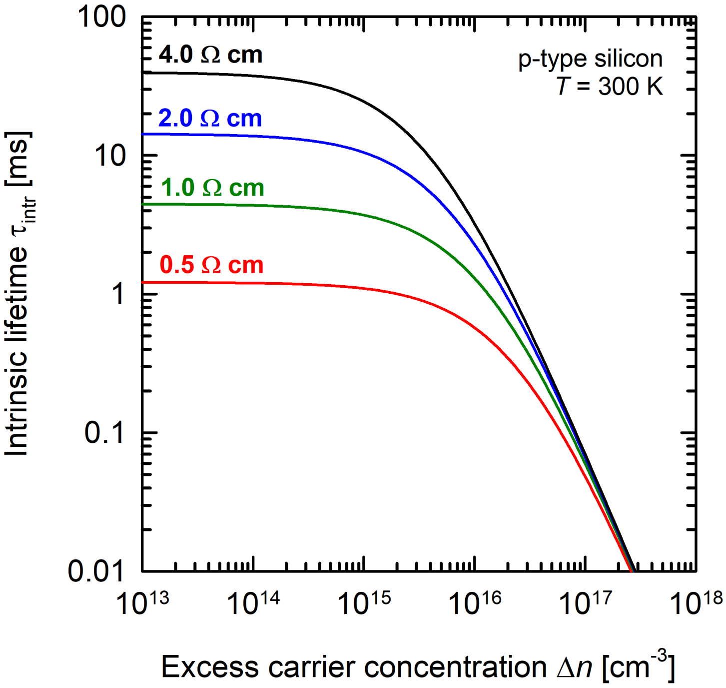

Figure 2.1: Intrinsic lifetime $\tau_{\text{intr}}(\Delta n)$ for four different base resistivities at 300 K according to Richter et al. [36].

Note, however, that a new physically motivated parametrization of the intrinsic lifetime has been published during work on this thesis [37]. Reports of measured lifetimes exceeding the parametrization by Richter et al. [36] indicated an overestimation in certain injection regimes. For consistency reasons, this new assessment has not been considered for the work in this thesis. The impact of the new parametrization [37] on the lifetimes reported in this thesis is expected to be negligible. The focus of this work is on industrially relevant Cz-Si materials instead of high-quality defect-lean materials and the reported lifetimes are mostly in the lower injection regimes (i.e., $\Delta n = 10^{15}\,\text{cm}^{-3}$). Furthermore, we are foremost interested in changes of the lifetime triggered by carrier injection and temperature and less in absolute lifetime values.

2.2 Extrinsic recombination

Extrinsic recombination of carriers denotes recombination due to impurities and crystallographic defects in the material. These defects create discrete energy levels within the band gap that can act as recombination centers. More precisely, the energy levels can be occupied by either an electron or a hole and interact with the conduction and valence band, thereby increasing extrinsic recombination. Unlike intrinsic recombination, extrinsic recombination can be reduced by use of materials with less built-in impurities or crystallographic defects due to the manufacturing process or by improving the purity of the material through processing steps (e.g., cleaning, gettering, passivation). In this thesis, we distinguish between two types of extrinsic recombination: Recombination due to defects in the silicon bulk and recombination due to defects located at the surfaces of the silicon wafers.

Shockley-Read-Hall recombination: Extrinsic recombination in the bulk that is dominated by a single monovalent energy level is usually referred to as Shockley-Read-Hall recombination or trap-assisted recombination. According to Shockley and Read [38] and Hall [39], the recombination can be described by

$$U_{\mathrm{SRH}} = \frac{np - n_{\mathrm{i}}^2}{\tau_{\mathrm{p0}}\left(n + n_1\right) + \tau_{\mathrm{n0}}\left(p + p_1\right)}, \tag{2.8}$$

with τ_{p0} and τ_{n0} being the capture time constants for holes and electrons, respectively, which are related to the capture cross sections σ_{p} and σ_{n} via

$$\begin{aligned} \tau_{\mathrm{p0}} &= \left(\sigma_{\mathrm{p}} v_{\mathrm{th}} N_{\mathrm{t}}\right)^{-1} \\ \tau_{\mathrm{n0}} &= \left(\sigma_{\mathrm{n}} v_{\mathrm{th}} N_{\mathrm{t}}\right)^{-1}, \end{aligned} \tag{2.9}$$

with the thermal carrier velocity v_{th} and the defect concentration N_{t}. The factors n_1 and p_1 in Eq. (2.8) are the so-called SRH densities and denote the carrier concentrations in conduction and valence band, respectively, if the Fermi energy would coincide with the defect energy level E_{t}:

$$\begin{aligned} n_1 &= N_{\mathrm{c}} \times \exp\left(-\frac{E_{\mathrm{c}} - E_{\mathrm{t}}}{k_{\mathrm{B}} T}\right) \\ p_1 &= N_{\mathrm{v}} \times \exp\left(-\frac{E_{\mathrm{t}} - E_{\mathrm{v}}}{k_{\mathrm{B}} T}\right), \end{aligned} \tag{2.10}$$

with N_{c} and N_{v} being the effective density of states in conduction and valence band, respectively, E_{c} and E_{v} being the corresponding energies of the band edges, k_{B} being the Boltzmann constant, and T being the absolute temperature.
Using Eq. (2.3) and assuming charge carrier neutrality, the recombination rate in Eq. (2.8) can be described by a corresponding SRH lifetime:

$$\tau_{\mathrm{SRH}} = \frac{\tau_{\mathrm{p0}}\left(n_0 + n_1 + \Delta n\right) + \tau_{\mathrm{n0}}\left(p_0 + p_1 + \Delta n\right)}{n_0 + p_0 + \Delta n}. \tag{2.11}$$

A useful notation has been proposed by Murphy et al. [40]. Under the assumption that the defect density N_{t} is much lower than the equilibrium hole concentration p_0, τ_{SRH} can be written as

$$\tau_{\mathrm{SRH}} = \tau_{\mathrm{n0}}\left(1 + \frac{Q n_1}{p_0} + \frac{p_1}{p_0} + \frac{n}{p}\left(Q - \frac{Q n_1}{p_0} - \frac{p_1}{p_0}\right)\right), \tag{2.12}$$

with $Q = {}^{\tau_{\mathrm{p0}}}/_{\tau_{\mathrm{n0}}}$ being the capture time constant ratio of the defect. The advantage of this notation is that a single defect manifests itself as a straight line, if τ_{SRH} is plotted versus the carrier concentration ratio ${}^{n}/_{p}$. Both representations of the SRH lifetime are shown in Fig. 2.2 for two different Q values of 10 and 20 and for two different defect energy levels E_{t} relative to the conduction band edge $E_{\mathrm{c}} - 0.4\,\mathrm{eV}$ and $E_{\mathrm{c}} - 0.25\,\mathrm{eV}$.

Importantly, under the assumption of a deep-level defect, i.e., the energy level of the defect is close to the middle of the band gap, n_1 and p_1 are negligible and Eq. (2.12) simplifies to

$$\tau_{\mathrm{SRH}} = \tau_{\mathrm{n0}} \left(1 + Q\frac{n}{p}\right), \tag{2.13}$$

with $\tau_{\mathrm{n0}}Q$ being the gradient and τ_{n0} the intercept with the lifetime axis of the linear representation (cf. Fig. 2.2, solid black and short-dashed blue line).

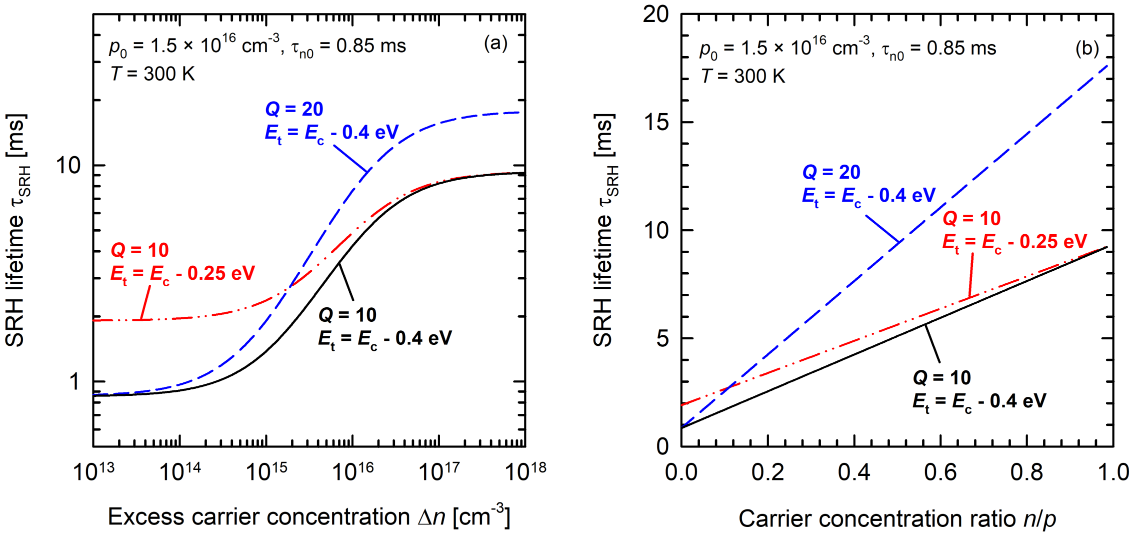

Figure 2.2: SRH lifetime of $1\,\Omega\,\mathrm{cm}$ p-type silicon at 300 K plotted for two different capture time constant ratios Q and energy levels of the single-level defect E_{t} at fixed τ_{n0}. (a) Injection-dependent SRH lifetime plotted versus Δn and (b) SRH lifetime versus ${}^{n}/_{p}$.

Surface-related recombination: At the surfaces of a silicon wafer, the periodic structure of the crystal is disrupted. The partially bonded silicon atoms generate a large number of recombination-active defect levels localized in the silicon band gap. Unlike SRH recombination in the bulk, surface-related recombination is not dominated by a single energy level, but the defect levels are continuously distributed throughout the band gap. If not sufficiently passivated, recombination at the surfaces may dominate the total recombination in a silicon wafer.

Throughout this thesis, two different passivation schemes are applied to reduce the recombination of carriers at the silicon wafer surfaces. Dielectric passivation with an $\mathrm{AlO}_x/\mathrm{SiN}_y$ stack of aluminum oxide (AlO_x) and silicon nitride (SiN_y) [41] and polycrystalline silicon on oxide (POLO) layers [25, 26]. Both combine two different passivation effects. The first passivation effect is based on the reduction of defects occurring at the crystal surface by saturating dangling bonds ("chemical passivation"). This is e.g. achieved by hydrogen from hydrogen-rich SiN$_y$:H layers or by a silicon oxide layer on top of the silicon. The second passivation mechanism is based on the reduction of the concentration of one type of carriers near the surface – which as a consequence reduces recombination requiring one electron and one hole for each recombination event – by inducing a band offset or bending via an electric field ("field-effect passivation"). AlO$_x$ exhibits a high density of fixed negative charges that results in a bending of the energy bands and consequently a depletion of electrons and a corresponding accumulation of holes. Another option to realize field-effect passivation is the use of highly-doped layers that reduce the respective minority carrier type. Poly-Si not only provides a very high level of surface passivation but also a high conductance for either electrons or holes depending on the doping of the poly-Si.

For a wafer with identical surface recombination velocities on front and rear side $S_{\text{front}} = S_{\text{rear}} = S$ (i.e., a symmetrically passivated wafer), the equivalent lifetime τ_{surf} of surface-related recombination can be written as [42]

$$\tau_{\text{surf}} = \frac{W}{2S} + \frac{1}{D}\left(\frac{W}{\pi}\right)^2 , \tag{2.14}$$

with W being the wafer thickness and D the diffusion constant of the excess carriers. The second term of Eq. (2.14) can be neglected for well passivated wafer (i.e., $^{SW}/_{D} < 0.25$) [42], which is always the case throughout this thesis. McIntosh and Black [43] proposed an alternative approach to describe surface-related recombination based

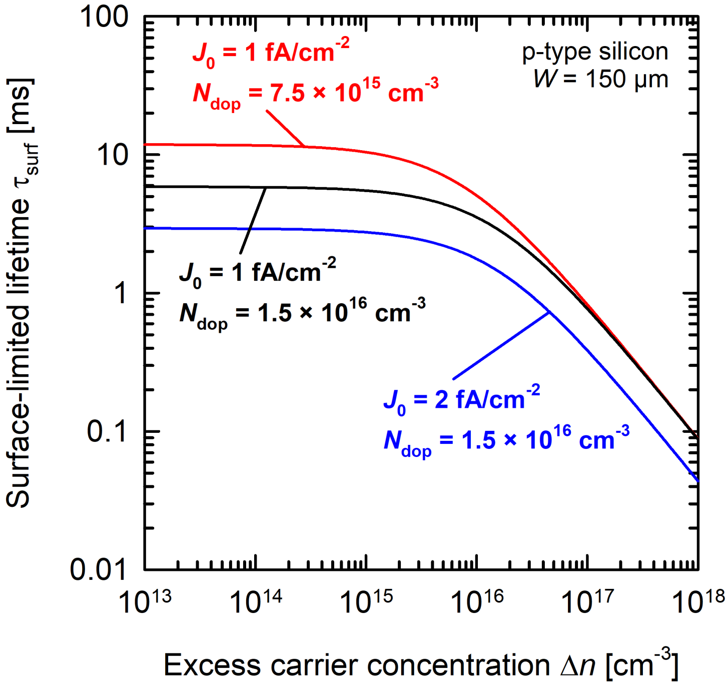

Figure 2.3: Injection-dependent lifetime of a 150 µm thick p-type wafer limited by surface-related recombination for two different saturation current densities J_0 and doping concentration N_{dop} according to Eq. (2.15).

on the recombination in emitter layers [44]. It yields [43]

$$\tau_{\text{surf}} \approx \frac{W}{2S} = \frac{eWn_{\text{i}}^2}{2J_0\left(N_{\text{dop}} + \Delta n\right)}, \tag{2.15}$$

with e being the elementary charge, N_{dop} being the doping concentration, and J_0 being the saturation current density of the emitter region.
Under the assumption that the injection dependence of the surface passivation can be expressed by a single J_0 value – which we assume for a symmetrically passivated sample throughout this thesis –we use the saturation current density J_0 of a "pseudo emitter" on the wafer surfaces as a measure for surface-related recombination and the quality of the surface passivation. Figure 2.3 shows the carrier lifetime limited by recombination at the surfaces according to Eq. (2.15) of a 150 µm thick p-type silicon wafer for two different J_0 values of 1 fA/cm^2 and 2 fA/cm^2 and two different doping concentration N_{dop} of $1.5 \times 10^{16}\,\text{cm}^{-3}$ and $7.5 \times 10^{15}\,\text{cm}^{-3}$.

2.3 The effective carrier lifetime

All the recombination mechanisms described in the Sections 2.1 and 2.2 occur simultaneously within a silicon wafer. Thus, the sum of all recombination rates represents the total recombination. The derived injection-dependent lifetime is called effective

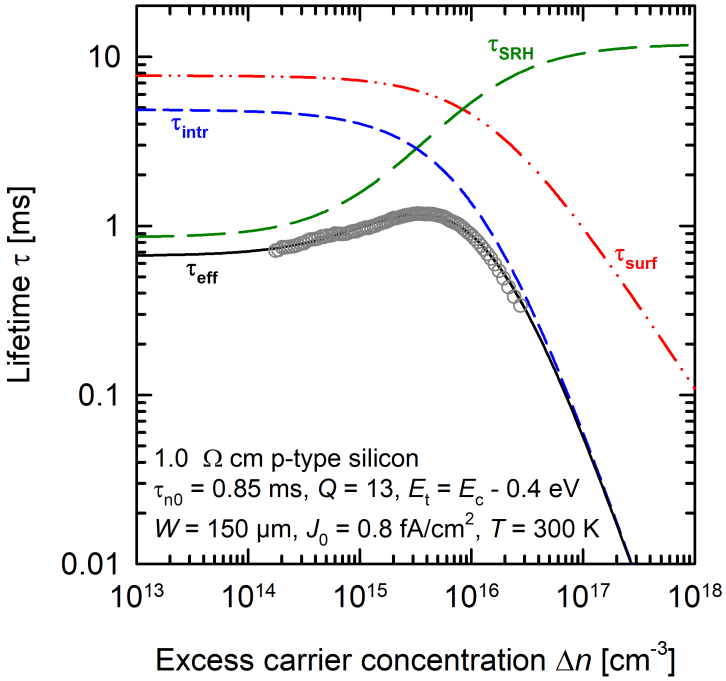

Figure 2.4: Calculated effective lifetime $\tau_{\text{eff}}(\Delta n)$ (solid black line) including its composition of different recombination channels, i.e., intrinsic lifetime τ_{intr} (blue short-dashed line), SRH lifetime τ_{SRH} (green long-dashed line), and surface-recombination-limited lifetime τ_{surf} (red dash-dotted line). The grey circles are a real measurement of the lifetime of a Cz-Si:Ga wafer after LeTID.

carrier lifetime $\tau_{\text{eff}}(\Delta n)$. It is hence given by the expression:

$$\frac{1}{\tau_{\text{eff}}} = \frac{1}{\tau_{\text{intr}}} + \frac{1}{\tau_{\text{SRH}}} + \frac{1}{\tau_{\text{surf}}}. \tag{2.16}$$

Figure 2.4 shows how $\tau_{\text{eff}}(\Delta n)$ is composed of the individual recombination channels. The grey circles are a real measurement of $\tau_{\text{eff}}(\Delta n)$ of a $1.0\,\Omega\,\text{cm}$ gallium-doped Cz-Si (Cz-Si:Ga) wafer ($W = 150\,\mu\text{m}$) after LeTID. As is clearly visible, the impact of the different recombination channels is differently dependent on the excess carrier concentration Δn. Whereas at low carrier injection ($< 3 \times 10^{15}\,\text{cm}^{-3}$) τ_{eff} is limited by SRH recombination in the bulk, at higher injection levels ($> 2 \times 10^{16}\,\text{cm}^{-3}$) τ_{eff} approaches the intrinsic limit of recombination in silicon. Recombination at the well passivated surfaces (i.e., $J_0 < 1\,\text{fA/cm}^2$) plays a minor role for recombination over the entire measured injection range.

2.4 Defect analysis

The lifetime experiments conducted in this thesis mainly focus on the degradation of τ_{eff} due to the activation of recombination-active defects under illumination at different temperatures and illumination intensities. For that, a simplified version of the lifetime analysis presented before in this chapter can be applied. Naturally, the impact of intrinsic recombination (cf. Section 2.1) does not change on the very same sample. Under the assumption that the surface passivation (cf. Section 2.2) remains stable, using Eq. (2.16), the SRH lifetime of the activated defect $\tau_{\text{SRH,def}}$ in

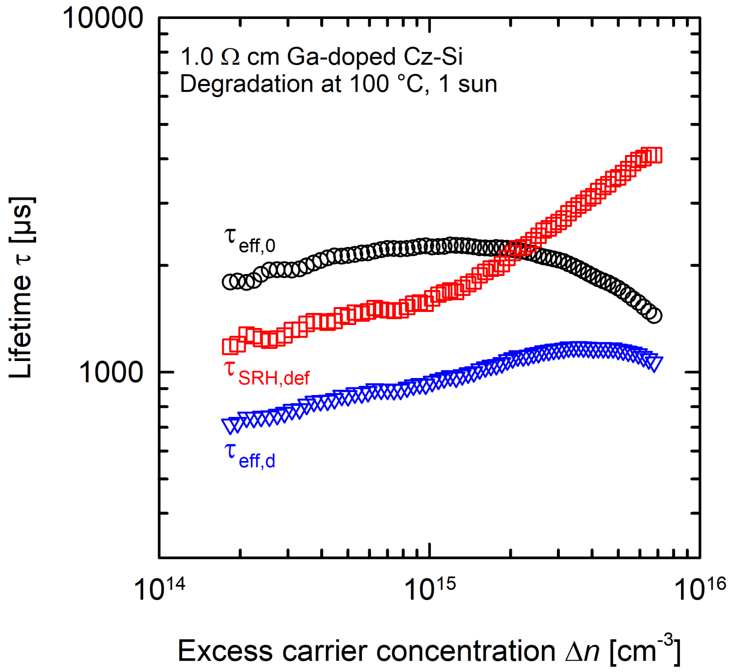

Figure 2.5: Injection-dependent defect analysis of a Cz-Si:Ga lifetime sample. Shown are the effective lifetime before degradation $\tau_{\text{eff},0}$ and the effective lifetime after degradation at 100 °C and 1 sun, $\tau_{\text{eff,d}}$. The SRH lifetime of the activated defect $\tau_{\text{SRH,def}}$ is calculated using Eq. (2.17).

the silicon bulk can be written as

$$\frac{1}{\tau_{\mathrm{eff,d}}} - \frac{1}{\tau_{\mathrm{eff,0}}} = \frac{1}{\tau_{\mathrm{SRH,d}}} - \frac{1}{\tau_{\mathrm{SRH,0}}} = \frac{1}{\tau_{\mathrm{SRH,def}}} \equiv N_{\mathrm{d}}^{*}, \tag{2.17}$$

with $\tau_{\mathrm{eff,d}}$ and $\tau_{\mathrm{SRH,d}}$ being the effective and SRH lifetime in the degraded state and $\tau_{\mathrm{eff,0}}$ and $\tau_{\mathrm{SRH,0}}$ being the corresponding lifetimes before degradation. The inverse of $\tau_{\mathrm{SRH,def}}$ is defined as the effective defect concentration N_{d}^{*}. It is not to be confused with an actual concentration of defects in our samples, but a measure to compare defect concentrations and their impact on the carrier lifetime. The simplified defect analysis is shown exemplarily in Fig. 2.5 for a Cz-Si:Ga lifetime sample illuminated at 100 °C and 1 sun (100 mW/cm^2) leading to a pronounced degradation in lifetime. Like $\tau_{\mathrm{SRH,def}}$, the derived N_{d}^{*} obviously is dependent on Δn. For the calculation of degradation rate constants and the comparison of effective defect concentrations N_{max}^{*} throughout this thesis using the time-dependent version of Eq. (2.17), we will refer to the effective defect concentration $N_{\mathrm{d}}^{*}(t)$ at a fixed excess carrier concentration of $\Delta n = 10^{15}\,\mathrm{cm}^{-3}$.

To verify that the recombination near the surfaces of the lifetime samples remains the same before and after degradation – thereby ensuring the validity of Eq. (2.17) – we use the saturation current density J_0 on both surfaces. To measure J_0, a method to extract it from injection-dependent lifetime measurements developed by Kane and Swanson [45] is used. The inverse measured lifetime after subtraction of the inverse intrinsic lifetime is plotted versus Δn and fitted linearly for $\Delta n > N_{\mathrm{dop}}$. Since

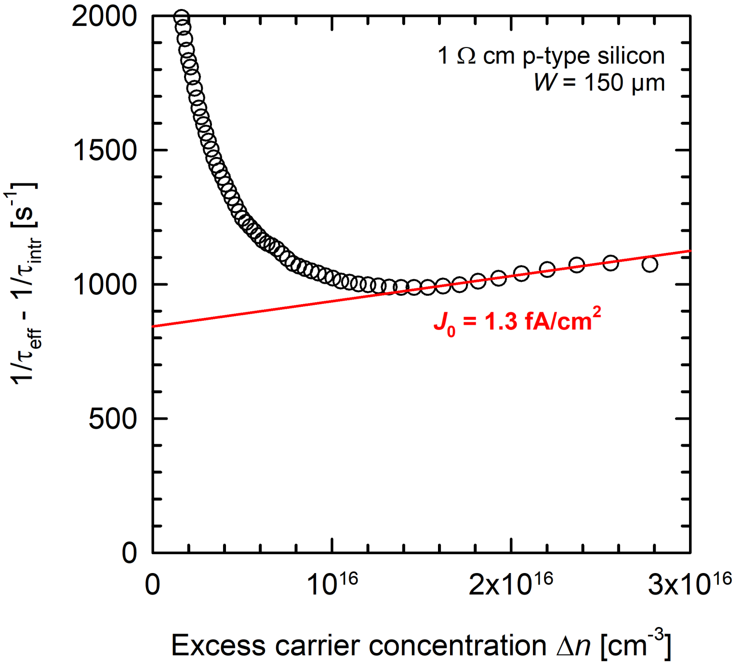

Figure 2.6: Determination of the surface passivation quality of a symmetrically passivated lifetime sample using a method developed by Kane and Swanson [45]. The injection-dependent lifetime is plotted inversely after subtraction of the inverse intrinsic lifetime. The recombination for $\Delta n > N_{\mathrm{dop}}$ is dominated by surface-related recombination and the saturation current density J_0 can be extracted from the gradient according to Eq. (2.15).

the recombination for $\Delta n > N_{\mathrm{dop}}$ is dominated by surface-related recombination (cf. Fig. 2.4), J_0 can be extracted from the gradient according to Eq. (2.15). This analysis is shown exemplarily for a Cz-Si:Ga lifetime sample in Fig. 2.6. Another application of the J_0-based determination of the surface passivation quality used within this thesis is the analysis of surface-related defects due to different passivation schemes.

3 Characterization methods

In this chapter, we will present the characterization techniques used in this thesis. This includes the measurement of (a) the injection-dependent carrier lifetimes using the photoconductance decay (PCD) method, (b) the spatially-resolved measurement of the carrier lifetime using a photoconductance-calibrated photoluminescence (PL) setup, (c) a contactless eddy-current method to measure resistivity changes in silicon wafers, and (d) the current-voltage measurement to determine the electrical solar cell parameters. The operating principle of a solar cell is outlined briefly on the basis of a "poly-Si on oxide backjunction" cell (POLO BJ cell).

3.1 Photoconductance decay (PCD) method

The most important measurement parameter throughout this thesis is the effective carrier lifetime τ_{eff} (also simply called lifetime), which was introduced in Chapter 2. The standard setup to measure $\tau_{\mathrm{eff}}(\Delta n)$ on silicon lifetime samples is the WCT-120 lifetime tester from Sinton Instruments [46]. It applies the photoconductance decay (PCD) method to measure τ_{eff} as a function of the injection-level (i.e., the excess carrier concentration Δn) and averages $\tau_{\mathrm{eff}}(\Delta n)$ over a circular area with a diameter of approximately 2.5 cm. A schematic of the WCT-120 is shown in Fig. 3.1.
The lifetime sample is placed over a coil which is connected to a radio frequency (RF) bridge circuit working at a frequency of 10.7 MHz. The RF circuit induces eddy currents within the lifetime sample. According to Lenz's rule, these eddy currents in turn induce a voltage within the RF circuit, which is directly proportional to the conductance σ (unit: Siemens) of the lifetime sample. Excess carriers (i.e., electron-hole pairs) are generated within the lifetime sample by use of a Xenon flash lamp. While a spatially homogeneous generation of the excess carrier concentration Δn is ensured using two diffuser in front of the flash light, a homogeneous depth profile of Δn is generated via a long-pass filter with a cut-off wavelength of 700 nm.
The conductance σ of the lifetime sample can be separated into the conductance σ_0 in the dark and the photoconductance $\Delta\sigma$ generated by the flash lamp. For a homogeneous Δn distribution, $\Delta\sigma$ is given by

$$\Delta\sigma = eW(\mu_{\mathrm{n}} + \mu_{\mathrm{p}})\Delta n, \tag{3.1}$$

with the elementary charge e, the thickness W of the lifetime sample, and the electron and hole mobilities μ_{n} and μ_{p}. The carrier mobilities are weakly dependent on Δn, however, the sum $\mu_{\mathrm{n}} + \mu_{\mathrm{p}}$ is well known from the literature [48], and Eq. (3.1) can be solved iteratively for each measured $\Delta\sigma$. The photoconductance $\Delta\sigma$ is measured by the RF bridge circuit connected via an DAQ card to a personal computer. The illumination intensity of the flash light is time-dependent and is measured with

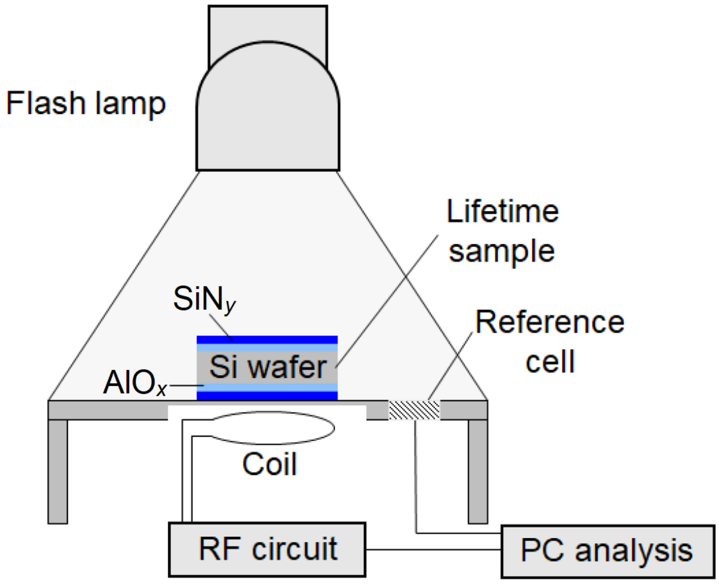

Figure 3.1: Schematic of the WCT-120 lifetime tester, which applies the PCD measuring technique to measure the carrier lifetime. The lifetime sample is placed over a detecting coil connected to an RF bridge circuit, which induces eddy currents within the lifetime sample. Excess carriers are excited within the silicon sample using a flash lamp, whose parameters are characterized by a reference solar cell. The resulting changes of the photoconductance $\Delta\sigma$ are measured via Lenz's rule by the RF bridge circuit connected to a DAQ card. In post processing (PC analysis), $\Delta\sigma$ is translated into an injection-dependent lifetime $\tau_{\mathrm{eff}}(\Delta n)$. The measured lifetime represents an averaged value over a circular area with a diameter of approximately 2.5 cm (approximately the area of the detecting coil). Picture adapted from Helmich [47].

an integrated reference solar cell. The generation rate G can be calculated via

$$G(t) = \frac{I_{\mathrm{ill}}(t) \times J_{\mathrm{sc,1sun}} \times T_{\mathrm{eff}}}{eW}, \tag{3.2}$$

with the time-dependent illumination intensity $I_{\mathrm{ill}}(t)$ (in this thesis always given in suns), the short-circuit current density of the reference cell under one-sun illumination $J_{\mathrm{sc,1sun}}$, and the effective transmission T_{eff}, which is a parameter to account for differences in the photogeneration between the lifetime sample and the reference cell (i.e., thickness and optical properties).

The time dependence of the excess carrier concentration $\Delta n(t)$ is given by the continuity equation [49]

$$\frac{\partial \Delta n(x,t)}{\partial t} = G(x,t) - U(x,t) + \frac{1}{e}\nabla J, \tag{3.3}$$

with the generation rate $G(x,t)$, the recombination rate $U(x,t)$, and the current density J. If the carrier distribution upon illumination is homogeneous, ∇J and the spatial dependence on x vanish. While the time dependence of $G(t)$ is given by the flash light, the time dependence of $U(t)$ depends on $\Delta n(t)$. The ratio of these two quantities, as already defined in Eq. (2.3), is the effective carrier lifetime

$$\tau_{\text{eff}}(\Delta n) \equiv \frac{\Delta n}{U(\Delta n)}. \tag{3.4}$$

Using Eq. (3.4), Eq. (3.3) can be rewritten as the generalized expression for τ_{eff}:

$$\tau_{\text{eff}} = \frac{\Delta n}{G(t) - \frac{\partial \Delta n(t)}{\partial t}}. \tag{3.5}$$

If τ_{eff} is much shorter than the decay time of the flash light, the sample is approximately in steady-state at each point in time and ${}^{\partial \Delta n(t)}/_{\partial t} = 0$ (referred to as quasi-steady-state photoconductance measurement, QSSPC), and Eq. (3.5) simplifies to $\tau_{\text{eff}} = {}^{\Delta n}/_{G(t)}$. If τ_{eff} is significantly longer than the decay time of the flash light, we speak of the photoconductance decay (PCD) mode. In this mode, the data acquisition of $\Delta\sigma$ does not start until the flash light is terminated. Thus, the generation rate $G(t)$ is zero and Eq. (3.5) simplifies to

$$\tau_{\text{eff}} = -\frac{\Delta n}{\frac{\partial \Delta n(t)}{\partial t}}. \tag{3.6}$$

The transient PCD method described by Eq. (3.6) for τ_{eff} values larger than ~800 µs and the generalized data evaluation applying Eq. (3.5) for τ_{eff} lower than ~800 µs are used within this thesis to extract the injection-dependent lifetime. For the latter, two different Xenon flashes of different intensities with decay time constants of ~50 µs and ~2.3 ms can be chosen dependent on the lifetime level and the desired Δn range. The QSSPC method is not used throughout this thesis.

Figure 3.2 shows a PCD measurement exemplarily for a 150 µm thick Ga-doped Cz-Si lifetime sample. In Fig. 3.2(a) the actual measurements of the illumination intensity I_{ill} (black line, left axis) determined from the reference cell and the photoconductance

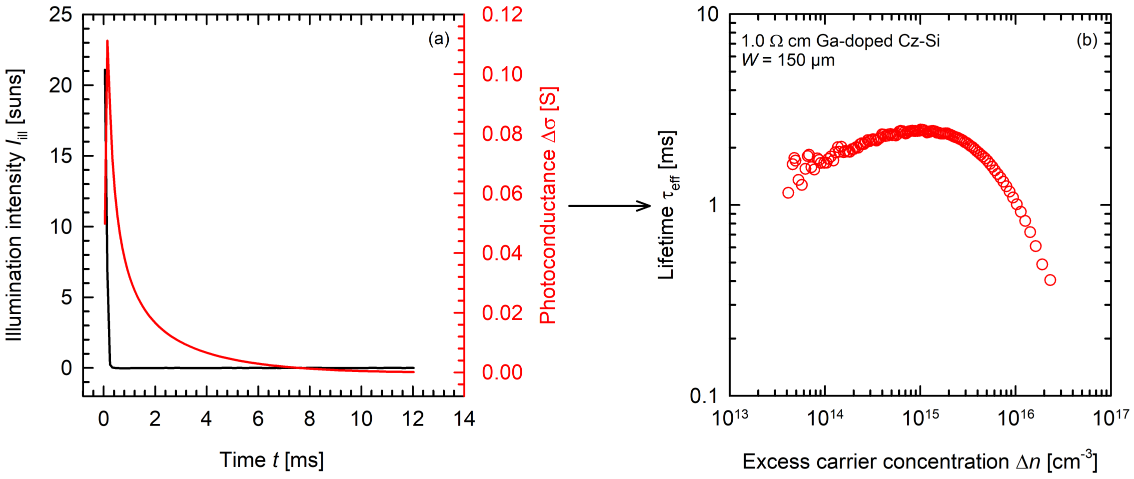

Figure 3.2: PCD lifetime measurement using the WCT-120 from Sinton Instruments. (a) Illumination intensity I_{ill} of the flash light (black line) and decay of the photoconductance $\Delta\sigma$. (b) Injection-dependent effective lifetime τ_{eff} calculated from the photoconductance decay $\Delta\sigma$ in (a) using Eq. (3.6)

$\Delta\sigma$ (red line, right axis) measured inductively via the RF circuit are shown. These two measurement parameters are then translated via automated post-processing into an injection-dependent lifetime $\tau_{\mathrm{eff}}(\Delta n)$ in Fig. 3.2(b).

3.2 Photoluminescence (PL) lifetime imaging

In Section 3.1, we introduced the PCD method to measure the injection-dependent carrier lifetime $\tau_{\mathrm{eff}}(\Delta n)$ inductively and averaged over the circular area above a detector coil with a diameter of approximately 2.5 cm. In this section, we introduce a method to measure $\tau_{\mathrm{eff}}(\Delta n)$ spatially-resolved using a photoconductance-calibrated photoluminescence setup (PL). Details regarding the measurement method have been published by Herlufsen et al. [50, 51].

Figure 3.3(a) shows the measurement setup schematically. The silicon wafer is homogeneously excited by means of a laser diode at a wavelength of 808 nm. Long-pass filters are used to prevent the detection of laser reflections. The resulting PL signal I_{PL} measured with a silicon charge-coupled device (Si CCD) camera is proportional to the product of electron concentration n and hole concentration p. It is for p-type silicon:

$$I_{\mathrm{PL}} = A \times B_{\mathrm{rad}} \times n \times p \approx A \times B_{\mathrm{rad}} \times \Delta n \times (\Delta n + N_{\mathrm{dop}}) , \tag{3.7}$$

assuming $p_0 \approx N_{\mathrm{dop}}$ and $n_0 + \Delta n \approx \Delta n$ as well as carrier neutrality. A accounts for the optical properties of the sample and the measurement setup and B_{rad} is the coefficient of radiative recombination. For a homogeneous excitation over the wafer area, different optics to widen the laser beam and a homogenizer are used. In addition,

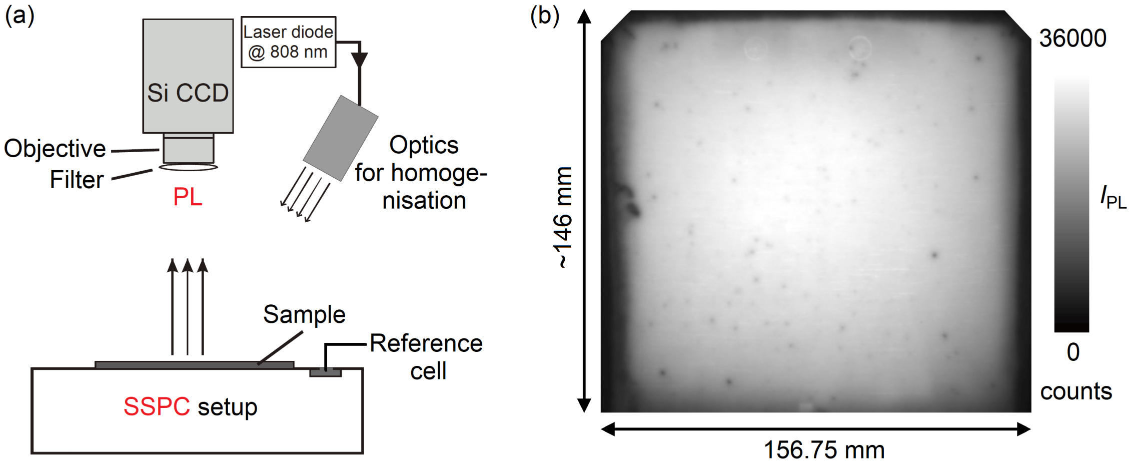

Figure 3.3: (a) Schematic of the photoconductance-calibrated photoluminescence (PL) setup to measure the carrier lifetime spatially-resolved. The steady-state photoconductance (SSPC) setup depicts an identical setup as described for PCD measurements in Section 3.1, but under steady-state conditions with a constant illumination intensity. Picture adapted from Herlufsen et al. [50]. (b) PL image of an M2-size 1 Ω cm Cz-Si:Ga wafer, which has been passivated with an $\mathrm{AlO}_x/\mathrm{SiN}_y$ stack on both surfaces, under laser excitation of a 0.5 suns equivalent. The lower edge of ~10 mm is not visible in the image because it was not in the focus of the camera during the measurement.

the intensity profile of the laser as it is detected by the Si CCD camera is used in post-processing to correct the PL signal. The measurement is conducted under constant illumination, so called steady-state conditions, and results in spatially-resolved images of the PL signal in counts (cts) per second at arbitrary predefined illumination intensities. This is shown exemplarily in Fig. 3.3(b) for a laser illumination intensity of 0.5 suns equivalent.

The excess carrier concentration Δn is determined using the steady-state photoconductance (SSPC) method, which is described in detail in Section 3.1, under constant illumination. The lifetime sample is placed above the detector coil, which averages the signal over a circular area with a diameter of approximately 2.5 cm. Averaging the PL signal over the same area via the Si CCD camera relates the PL signal to the excess carrier concentration Δn within the sample. This calibration is shown exemplarily in Fig. 3.4.

The calibration function follows a second-order polynomial according to Eq. (3.7):

$$I_{\mathrm{PL}} = a \times \Delta n^2 + b \times \Delta n. \tag{3.8}$$

Since the photoconductance is measured under steady-state illumination, Eq. (3.5), relating the lifetime τ_{eff} to Δn, simplifies to

$$\tau_{\mathrm{eff}} = \frac{\Delta n}{G}. \tag{3.9}$$

The generation rate G in the silicon wafer is determined from the photon flux of the illumination Φ of a calibrated reference silicon solar cell integrated into the

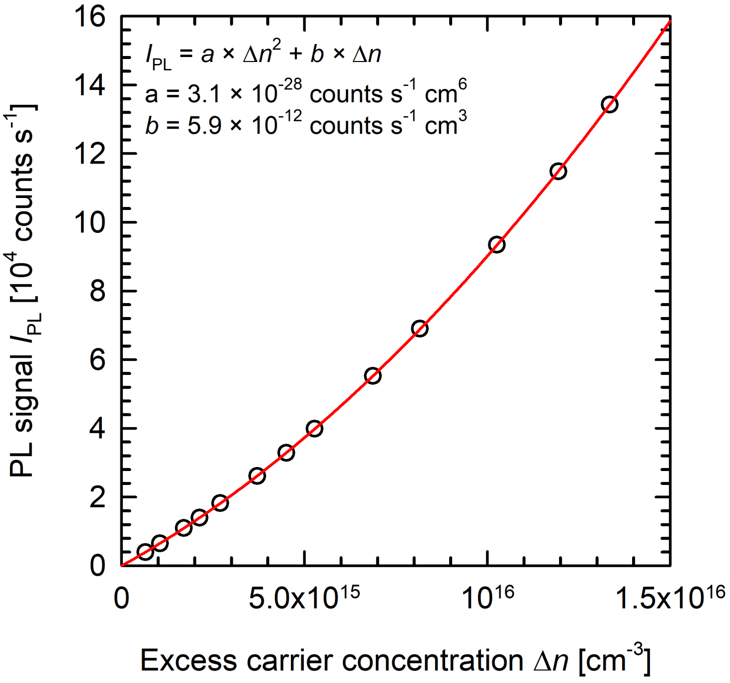

Figure 3.4: Calibration relating the PL signal (measured via Si CCD camera) to the excess carrier concentration Δn (measured via SSPC) during laser excitation at 808 nm. The calibration function I_{PL} (red line) follows a second-order polynomial according to Eq. (3.7).

measurement setup:

$$G = \Phi \left(1 - R_{808}\right) \frac{1}{W}, \tag{3.10}$$

with R_{808} being the reflectivity at the laser wavelength of 808 nm and W being the thickness of the silicon wafer. Equation (3.10) is a valid approximation because the penetration depth of the laser at 808 nm is only ~12.7 µm, which is much less than the wafer thickness of 150 µm.

Combining Eqs. (3.7) and Eq. (3.9) gives the excess carrier concentration Δn and the corresponding lifetime τ_{eff} at any given point of the wafer at the predefined illumination intensities. Through interpolation in post-processing, wafer images at constant Δn as well as injection-dependent lifetimes for any given area of the wafer can be generated as well.

3.3 Eddy-current measurements of the wafer resistivity

The eddy-current method applied in the WCT-120 lifetime tester from Sinton Instruments (cf. Section 3.1) can be used to contactlessly measure the resistivity ρ of a silicon wafer.

For sufficiently small conductances σ (<0.2 S), σ and the measured output voltage $V = V_{\text{sample}} - V_{\text{air}}$ are correlated linearly:

$$\sigma = a \times V. \tag{3.11}$$

V_{sample} and V_{air} being the voltages measured with and without a silicon wafer placed above the detecting coil (cf. Fig. 3.1). These voltages are directly measured using a precision multimeter (Fluke, 8845A). The correlation between V and σ is shown in Fig. 3.5 for a set of calibration wafers. Using this calibration, the resistivity of the lifetime sample ρ (in Ω cm) can be calculated from the output voltage:

$$\rho = \frac{W}{a \times V}, \tag{3.12}$$

with the wafer thickness W. The conductance σ – and hence the resistivity ρ – is temperature dependent. Therefore, ρ is extrapolated to a fixed temperature of 25 °C via

$$\rho_{25\,^\circ\text{C}} = \left(1 - C_\vartheta \left(\vartheta_{\text{meas}} - 25\,[^\circ\text{C}]\right)\right) \times \rho_{\text{meas}}, \tag{3.13}$$

with ρ_{meas} being the resistivity measured at a temperature ϑ_{meas} and C_ϑ being a temperature coefficient dependent on the doping type and the doping concentration of the silicon sample under test. For the p-type silicon used in this thesis, C_ϑ is $7.07 \times 10^{-3}\,^\circ\text{C}^{-1}$ and $7.22 \times 10^{-3}\,^\circ\text{C}^{-1}$ for 1.0 Ω cm and 1.2 Ω cm, respectively [52]. The output voltages to calculate the resistivity according to Eq. (3.12) are measured using a precision multimeter (8845A, Fluke).

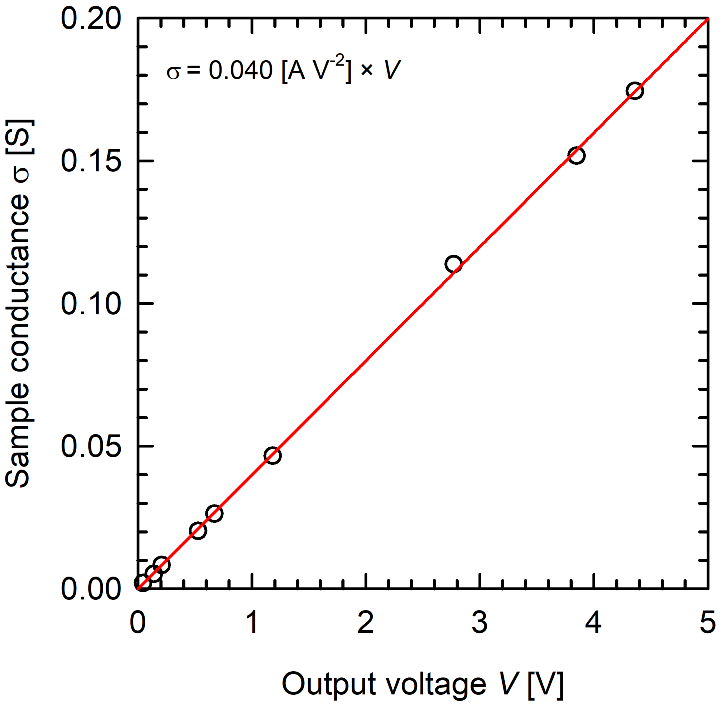

Figure 3.5: Calibration of the RF bridge circuit that is integrated in the WCT-120 lifetime tester from Sinton Instruments. For sufficiently small conductances σ (<0.2 S), σ and the measured output voltage V are correlated linearly.

3.4 Current voltage measurements

In the previous sections of this chapter, two different methods – namely PCD and PL – were introduced to measure the effective carrier lifetime τ_{eff} of lifetime samples, which are basically passivated silicon wafers without any contacts and metalization on the rear and front surface to collect the excess carriers. In this section, we want to describe the current-voltage (IV) measurement used within this thesis to determine the impact of the observed lifetime instabilities on the performance of actual solar cells.

3.4.1 Operating principle of a POLO backjunction solar cell

Figure 3.6 shows a schematic of a ”poly-Si on oxide backjunction” solar cell (POLO BJ cell) with a p-type silicon base [53, 54] as absorber. The front surface of the solar cell is textured and coated with a stack of aluminum oxide AlO_x and silicon nitride SiN_y. SiN_y serves as an antireflection coating to couple as much of the incident light as possible into the solar cell. Furthermore, SiN_y layers serve as hydrogen source for the saturation of dangling bonds at the surfaces (cf. Section 2.2). The incident light of high enough energy $h\nu$, that is not reflected at the metal contacts and the front surface or leaves the solar cell at the rear side, is absorbed by the p-type silicon absorber and generates electron-hole pairs. These electrons and holes have to be collected by electron-selective and hole-selective contacts at the rear and front side of the solar cell.

Depending on the carrier lifetime and hence the carrier diffusion length in the silicon

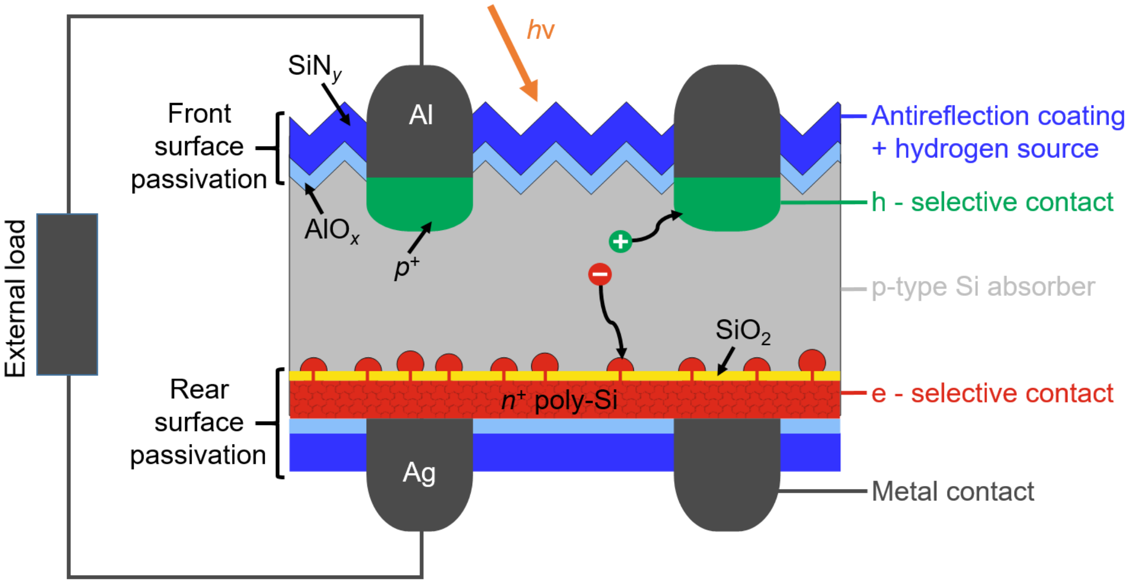

Figure 3.6: Schematic of the cross section of a POLO backjunction solar cell with a p-type silicon base [53, 54].

base, there is a certain probability for recombination before the carriers reach the contacts. Recombination can occur in the bulk, at the non-metallized surfaces, or the metal contacts themselves. To minimize recombination in the bulk, the bulk lifetime has to be as large as possible. This can be achieved by the use of defect-lean silicon materials, by reducing the concentration of recombination-active defects either through cleaning and gettering processes or through adapted processing steps, and by passivation of existing defects so that they are not or less recombination-active. These are topics addressed in this thesis. Recombination at the surfaces can be significantly reduced by different passivation schemes, which are usually a combination of a chemical passivation to saturate dangling bonds and a field effect passivation to reduce the concentration of one type of carrier at the surface (cf. Section 2.2). In the POLO BJ solar cell shown in Fig. 3.6, surface passivation is achieved by an AlO_x/SiN_y stack [41] on the front surface and an SiO_2/poly-Si/AlO_x/SiN_y stack [25, 26] on the rear. To reduce recombination at the metal contacts, two different methods are used in Fig. 3.6. At the front surface, a highly Al-doped region (p^+, h-selective contact) localized underneath the Al contact reduces the minority carrier concentration (i.e., electrons) near the non-passivated silicon-metal interface. At the rear side, a carrier selective contact (n^+ poly-Si, e-selective contact) is used, which accumulates one type of carrier (i.e., electrons), while at the same time blocking the other type (i.e., holes). The POLO stack at the rear combines excellent surface passivation quality [25, 26] with very low contact resistivities [27], hence leading to a very large carrier selectivity [55]. Due to parasitic absorption of the incident light [56–58], poly-Si is not used at the front surface of the cell.

3.4.2 Characteristic solar cell parameters

Solar cell performance is well described by the current-voltage curve under illumination (light IV curve), which means the superposition of the light-generated current density J_L with the current-voltage (IV) curve of the solar cell diode in the dark. In general, the $J(V)$ dependence is given by the expression [59]

$$J = J_\mathrm{L} - J_0 \left(\exp\left(\frac{e\,(V + JR_\mathrm{s})}{n_\mathrm{ideal} k_\mathrm{B} T} \right) - 1 \right) - \frac{V + JR_\mathrm{s}}{R_\mathrm{sh}}, \tag{3.14}$$

with J_0 being the saturation current density, k_B being the Boltzmann constant, and T being the absolute temperature in Kelvin. The equivalent circuit diagram is shown in Fig. 3.7. The so-called ideality factor n_ideal describes non-ideal diode behavior of the solar cell via upward deviations from unity. In fact, n_ideal values smaller than one are also possible in high-injection, if the bulk lifetime is limited by Auger recombination [60]. The series resistance R_s (in $\Omega\mathrm{cm}^2$) consists primarily of the base and emitter resistance of the semiconductor, the resistance of the metallic contacts and interconnections, and the contact resistances of the semiconductor/metal interfaces. The shunt resistance R_sh (in $\Omega\mathrm{cm}^2$) stems from alternate current paths for the light-generated current which is mostly the result of imperfect manufacturing processes, e.g., non-passivated edges or metalization of a damaged emitter. As apparent from Eq. (3.14), a small R_s and a high R_sh are desirable for good solar cell performance.

Figure 3.8 shows an IV curve measured on a POLO BJ solar cell under one-sun equivalent illumination. Characteristic solar cell parameters, which will be introduced in the following, are highlighted. The IV measurements in this thesis were conducted using an LED array light source at 850 nm built into a LOANA system from pv-tools [61].

The most prominent parameter to characterize a solar cell is the energy conversion efficiency η. The efficiency η is defined as the ratio between the electrical output power and the power of the incident light P_in. It is hence given by

$$\eta = \frac{P_\mathrm{MPP}}{P_\mathrm{in}} = \frac{J_\mathrm{sc} \times V_\mathrm{oc} \times FF}{P_\mathrm{in}}, \tag{3.15}$$

with the short-circuit current density J_sc, the open-circuit voltage V_oc, and the so-called fill factor FF. The product of these three parameter is the output power P_MPP

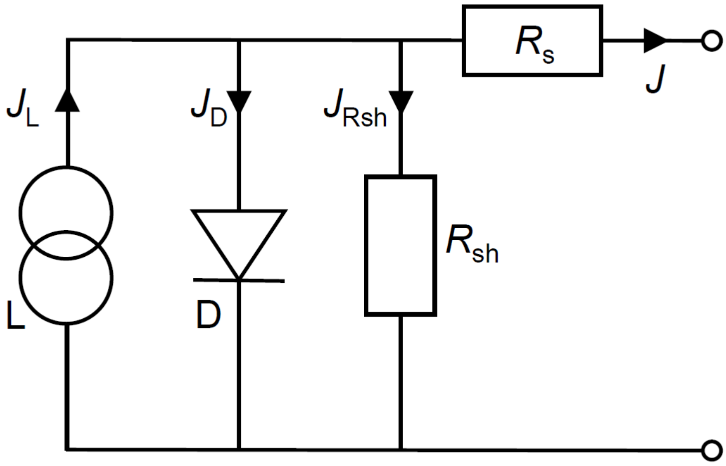

Figure 3.7: Equivalent circuit diagram including a current source L (light-generated current), the diode D, a parallel shunt resistance R_sh, and a series resistance R_s.

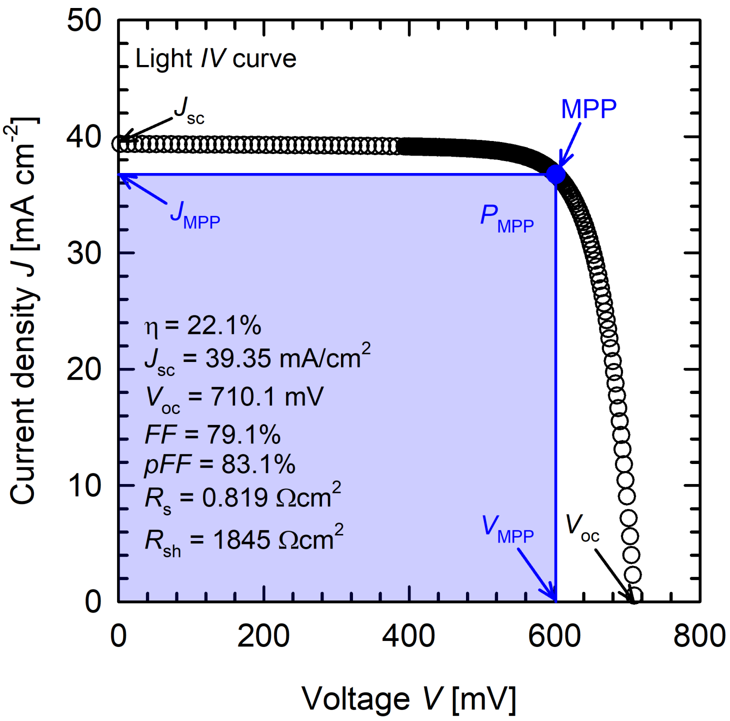

Figure 3.8: Measured current-voltage (IV) curve of a POLO BJ solar cell under one-sun equivalent illumination using an LED array light source at 850 nm. The cell parameters short-circuit current density J_{sc}, open-circuit voltage V_{oc}, and the output power at the maximum power point (MPP) $P_{\mathrm{MPP}} = J_{\mathrm{MPP}} \times V_{\mathrm{MPP}}$ as blue area are highlighted.

at the maximum power point (MPP). At MPP, the electrical power, the product of current density J and voltage V generated by the solar cell, is at its maximum.
The short-circuit current density J_{sc} denotes the maximum current density extracted from the solar cell, i.e., when it is short-circuited. The J_{sc} value depends on the number of photons with high enough energy to generate electron-hole pairs in the silicon base and on the successful collection of these carriers at the contacts. Therefore, J_{sc} depends directly on the light intensity and the spectrum of the incident light. In the LOANA system, J_{sc} is measured under a one-sun equivalent using a short Xenon flash. The light is filtered to match the spectrum as close as possible to an AM1.5G spectrum (class A of IEC 60904-9 according to the manufacturer, pv-tools). The IV curve is then measured using an infrared LED array at a wavelength of 850 nm at an illumination intensity that matches the J_{sc} values obtained from the Xenon flash and the LED measurement. To increase J_{sc}, the optical properties of the solar cell have to be improved through minimizing reflection and absorption losses. The quality of the surface passivation and the carrier lifetime in the base affect J_{sc} as well by an increased probability of carrier collection at the respective metal contact.
The open-circuit voltage V_{oc} denotes the highest possible voltage, i.e., if no current is extracted. Experimentally, the V_{oc} value is obtained from the light IV measurement. According to semiconductor physics, V_{oc} of an ideal solar cell is connected

with the excess carrier concentration Δn at open circuit by the equation [46]:

$$V_{\mathrm{oc}} = \frac{k_{\mathrm{B}}T}{e} \times \ln\left((p_0 + \Delta n)\frac{\Delta n}{n_i^2}\right), \tag{3.16}$$

with p_0 being the equilibrium hole concentration, which equals the acceptor concentration in our p-type silicon base. Note that the temperature T – besides directly affecting V_{oc} – affects also the excess carrier concentration Δn and in particular the intrinsic carrier concentration n_{i} in Eq. (3.16). The most relevant effects are the pronounced temperature dependence of n_{i} and the temperature dependence of the band gap, which decreases with increasing temperature (empirically described by Varshni [62]). In total, V_{oc} is strongly temperature dependent and decreases with increasing temperature for crystalline silicon by 2 mV/K in the temperature range around 300 K [63]. However, it is apparent from Eq. (3.16) that increasing V_{oc} at a fixed temperature T is directly linked to an increasing Δn and therefore decreasing recombination in the solar cell.
The fill factor FF (usually reported in percent) in Eq. (3.15) is defined as

$$FF = \frac{J_{\mathrm{MPP}} \times V_{\mathrm{MPP}}}{J_{\mathrm{sc}} \times V_{\mathrm{oc}}}, \tag{3.17}$$

with J_{MPP} and V_{MPP} being the current density and the voltage at MPP. Graphically, the FF value is a measure of the "squareness" of the IV curve, it is given by the ratio between the rectangle of largest area under the IV curve (at MPP, blue rectangle in Fig. 3.8) and the rectangle spanned by J_{sc} and V_{oc}. In Fig. 3.8, the FF value is 79.1%. Ideally, the maximum possible FF value without including any resistance losses is a function of V_{oc}, given by the empirical expression [64]:

$$FF_0 = \frac{v_{\mathrm{oc}} - \ln\left(v_{\mathrm{oc}} + 0.72\right)}{v_{\mathrm{oc}} + 1}, \tag{3.18}$$

with $v_{\mathrm{oc}} = eV_{\mathrm{oc}}/\left(n_{\mathrm{ideal}}k_{\mathrm{B}}T\right)$ being the open-circuit voltage normalized to the thermal voltage. A real solar cell, however, suffers from parasitic series and shunt resistances reducing the FF value. To estimate the FF potential of a given solar cell, a so-called pseudo fill factor pFF can be determined by measuring both V_{oc} and J_{sc} values separately at different illumination intensities. The pFF value determined from the resulting J_{sc}-V_{oc} curve excludes any impact of the series resistance R_{s} and amounts to 83.1% for the solar cell in Fig. 3.8. The pFF can hence be regarded as a kind of "upper FF limit" of a specific solar cell. Under the assumption of a negligible series resistance R_{s}, but a non-negligible shunt resistance R_{sh} – circumstances provided by the pFF value –, the FF value is given by the empirical expression [64]:

$$FF_{\mathrm{sh}} = FF_0\left(1 - \frac{v_{\mathrm{oc}} + 0.7}{v_{\mathrm{oc}}} \times \frac{V_{\mathrm{oc}}FF_0}{J_{\mathrm{sc}}R_{\mathrm{sh}}}\right). \tag{3.19}$$

Using Eqs. (3.18) and (3.19), the pFF value of 83.1% (cf. Fig. 3.8) results in an ideality factor of $n_{\mathrm{ideal}} = 1.1$. An increasing n_{ideal} corresponds to a decreasing FF value, which – regarding this thesis – is caused by a strongly injection-dependent bulk lifetime due to a deep-level defect center [65].

4 Light- and elevated-temperature-induced degradation in boron-doped Czochralski-silicon

4.1 Introduction

The so-called 'Light- and elevated-temperature-induced degradation' (LeTID) effect [10–13] of the carrier lifetime in block-cast multicrystalline silicon (mc-Si) has become a steadily growing area of research over the past decade. The fast-firing step at the end of the solar cell production process was identified to trigger the degradation effect [13, 14] and the firing peak temperature was shown to have a major impact on the extent of the lifetime degradation [66]. More recently, there have been publications indicating that a similar defect could exist in Czochralski-grown silicon (Cz-Si) as well [15, 16, 67]. Other researchers, however, did not find any indications of the mc-Si-typical LeTID effect in Cz-Si material [68]. In addition, some publications reported LeTID in other types of monocrystalline silicon materials, such as float-zone silicon (FZ-Si) and n-type Cz-Si [17, 19, 69]. In this chapter, we examine the carrier lifetime degradation under illumination of boron-doped (B-doped) Cz-Si material at increased temperatures to investigate, if the mc-Si-specific LeTID defect also occurs in B-doped Cz-Si material. We apply various process conditions to the Cz-Si wafers known to effectively trigger LeTID in mc-Si wafers.

In a second step, we propose a simple method to separate the two main degradation phenomena – namely the activation of the boron-oxygen (BO) defect and the LeTID-type effect – observable on fired B-doped Cz-Si. Through BO activation/deactivation cycles by applying alternating illumination and dark annealing (DA) steps, both degradation effects can be characterized separately.

We point out similarities and differences of the LeTID effect observed in mc-Si and Cz-Si.

4.2 Experimental details

We use standard B-doped Cz-Si wafers with a base resistivity of $1.3\,\Omega\,\mathrm{cm}$. The saw damage of the wafers is removed in a KOH solution before cleaning them in a standard RCA sequence. The sample processing includes a phosphorus diffusion at 829 °C, resulting in n^+-diffused regions with a sheet resistance of either around $47\,\Omega/\mathrm{sq}$ or $100\,\Omega/\mathrm{sq}$ on both wafer surfaces. The phosphosilicate glass and the n^+-regions are removed afterwards by an HF dip and a short etch step in a KOH solution. The wafer surfaces are passivated with an $\mathrm{AlO}_x/\mathrm{SiN}_y$-stack on both sides [41]. 10 nm of aluminum oxide (AlO_x) are deposited using plasma-assisted atomic layer deposition (Oxford Instruments, FlexAl). 100 nm of silicon nitride (SiN_y) with a refraction index n of 2.05 (Meyer Burger, SiNA) or 120 nm with $n = 2.4$ (Oxford Instruments, Oxford Plasmalab 80 Plus) are deposited by plasma-enhanced chemical vapor deposition. Furthermore, on some wafers the AlO_x layers are omitted.

The wafers receive a fast-firing treatment using an industrial conveyor belt furnace (centrotherm international, DO–FF–8.600–300). Three different measured peak firing temperatures FT (550 °C, 750 °C, and 800 °C) with an uncertainty of ±10 °C at a belt speed of 6.8 m/min are applied. Only the higher temperatures of 750 °C and 800 °C are known to trigger the LeTID effect in mc-Si wafers, which is attributed to the in-diffusion of hydrogen from the silicon nitride and/or the dissolution of metal precipitates within the bulk [66]. The sample temperature during fast-firing is measured using a temperature tracker (Datapaq DQ1860A) and a type-K thermocouple (Omega, KMQXL-IM050G-300) within the furnace. The set-peak temperatures were different for Cz-Si and mc-Si wafers to obtain the same actual peak temperatures FT due to the different surfaces textures of the two different material types. The set-peak temperatures were 650 °C, 850 °C, and 900 °C respectively, for the Cz-Si wafers and 900 °C for reference mc-Si wafers. We will always refer to the measured FT throughout this chapter. For our experiments, the wafers are cut into 5 cm × 5 cm samples after firing.

After processing, the Cz-Si samples are annealed for 10 min at 200 °C in the dark to fully deactivate the BO defect. In order to investigate the impact of dark annealing on our reference mc-Si wafers [70], we compared the formation of the LeTID defect with and without previous dark annealing at 200 °C for 10 min. We observed no difference of the dark-annealed and the non-annealed mc-Si samples. Hence, the initial dark annealing will not be discussed further in the following.

The Cz-Si samples were exposed to different conditions. The standard test conditions are 80 °C and 1 sun ($100\,\mathrm{mW/cm^2}$) illumination with a halogen lamp, i.e., typical LeTID defect activation conditions as known from experiments on mc-Si samples [12, 13]. We measure the illumination intensity with a calibrated reference silicon solar cell. The lateral variation of the illumination intensity is less than ±0.05 suns, while the temperature during illumination is constant within a range of ±2 °C. Cz-Si samples illuminated at room temperature ((30 ± 2) °C, (0.10 ± 0.02) suns) serve as a reference to characterize the BO defect activation.

The lifetime is measured in between illumination at (30 ± 2) °C by the photoconductance decay (PCD) method using a WCT-120 lifetime tester from Sinton Instruments, the operating principle of which is explained in detail in Section 3.1. If not stated otherwise, the lifetime is stated at a fixed excess carrier concentration of $\Delta n = 10^{15}\,\mathrm{cm^{-3}}$. In addition, we examine the injection dependence of the effective lifetime to distinguish between bulk- and surface-related effects and to extract the defect-specific hole-to-electron capture time constant ratio.

4.3 Lifetime evolution at elevated temperatures

Figure 4.1(a) shows the lifetime evolution for two Cz-Si samples fired at an FT of 750 °C (black circles) and 550 °C (blue inverse triangles) and for an mc-Si sample fired at $FT = 750$ °C as a reference (red squares).

For the mc-Si sample (red squares), the typical LeTID behavior is clearly visible.

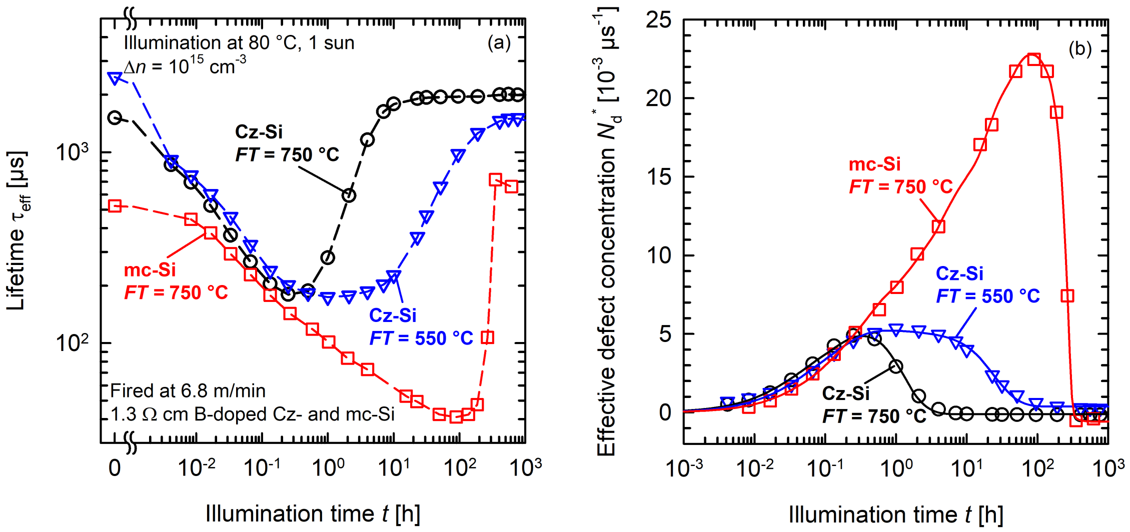

Figure 4.1: (a) Effective lifetime $\tau_{\mathrm{eff}}(t)$ and (b) the corresponding effective defect concentration $N_{\mathrm{d}}^{*}(t)$ illuminated at 1 sun at 80 °C. Results are shown for two Cz-Si samples fired at an FT of 750 °C (black circles) and 550 °C (blue inverse triangles) and for an mc-Si sample of the same doping concentration as a reference ($FT = 750\,°\mathrm{C}$, red squares). Whereas the dashed lines in (a) serve as guide to the eye, the lines in (b) are exponential fits of the data using Eq. (4.2) or Eq. (4.3), respectively.

The fully degraded state is reached after approximately 100 h at 80 °C and 1 sun illumination intensity. The lifetime regeneration starts afterwards and lasts for another ∼200 h. The Cz-Si sample fired at the same peak temperature, however, shows a different behavior (black circles). The degraded state is reached in less than an hour at 80 °C and 1 sun, which is attributed to the activation of the well-known BO defect [9]. The BO defect is fully deactivated after another ∼10 h comparable to [71]. The lifetime then remains stable under prolonged illumination. The Cz-Si sample fired at a peak temperature of only 550 °C, which is not expected to show any LeTID, also shows the typical BO degradation/regeneration cycle (blue inverse triangles in Fig. 4.1(a)). In Fig. 4.1(b), the corresponding effective defect concentration $N_{\mathrm{d}}^{*}(t)$ (cf. Section 2.4) is shown. The effective defect concentration is defined as

$$N_{\mathrm{d}}^{*}(t) = \frac{1}{\tau_{\mathrm{d}}(t)} - \frac{1}{\tau_{0}}, \tag{4.1}$$

with the lifetimes of the degraded and initial (dark-annealed) states $\tau_{\mathrm{d}}(t)$ and τ_0, respectively. The colors and symbols used in Fig. 4.1(b) match the ones in Fig. 4.1(a). Whereas the dashed lines in Fig. 4.1(a) serve as guide to the eye, the lines in Fig. 4.1(b) are exponential fits separating $N_{\mathrm{d}}^{*}(t)$ into a defect concentration of degradation $N_{\mathrm{deg}}^{*}(t)$ and regeneration $N_{\mathrm{reg}}^{*}(t)$:

$$\begin{aligned} N_{\mathrm{d}}^{*}(t) &= N_{\mathrm{deg}}^{*}(t) + N_{\mathrm{reg}}^{*}(t) \\ &= N_{\mathrm{max,deg}}^{*}\left(1 - \exp\left(-s(\Delta n) R_{\mathrm{deg}} \times t\right)\right) \\ &\quad - N_{\mathrm{max,reg}}^{*}\left(1 - \exp\left(-s(\Delta n) R_{\mathrm{reg}} \times t\right)\right), \end{aligned} \tag{4.2}$$

with the maximum defect concentration $N_{\mathrm{max,deg}}^{*}$ and the rate constant R_{deg} of the lifetime degradation, as well as $N_{\mathrm{max,reg}}^{*}$ and R_{reg} of the lifetime regeneration. Please note that the mc-Si degradation in Fig. 4.1(b) (red squares) requires a double-exponential fit:

$$\begin{aligned} N^*_{\mathrm{deg}}(t) = {} & N^*_{\mathrm{max,deg,1}}\left(1 - \exp\left(-s(\Delta n)R_{\mathrm{deg,1}} \times t\right)\right) \\ & + N^*_{\mathrm{max,deg,2}}\left(1 - \exp\left(-s(\Delta n)R_{\mathrm{deg,2}} \times t\right)\right), \end{aligned} \tag{4.3}$$

with a fast (1) and slow (2) component, respectively. Although the BO degradation has been shown to consist of a fast and a slow component as well [9] if examined at low temperatures (e.g., 30 °C), the fast component is not visible at higher temperatures (i.e., 80 °C) and can be ignored for the Cz-Si samples shown in Fig. 4.1. The scale factor $s(\Delta n)$ subsumes the Δn-dependence of R_{deg} and R_{reg} for a more accurate comparison of the rate constants of Cz-Si and mc-Si samples. It will be explained in more detail later in this section.

The maximum effective defect concentration $N^*_{\mathrm{max,deg,1}} + N^*_{\mathrm{max,deg,2}}$ for the LeTID defect in the mc-Si sample is more than 4 times larger than $N^*_{\mathrm{max,deg}}$ for the Cz-Si samples. The maximum effective defect concentration of the two Cz-Si samples fired at different peak temperatures FT, however, is almost identical as is the degradation rate constant R_{deg} of $(20.6 \pm 0.8)\,\mathrm{h}^{-1}$ (after firing at $FT = 750\,°\mathrm{C}$, black circles) and $(17.6 \pm 1.0)\,\mathrm{h}^{-1}$ ($FT = 550\,°\mathrm{C}$, blue inverse triangles). Both is to be expected for the BO defect activation, since the samples are processed from the same material. The degradation rate constants of LeTID in the mc-Si sample (Fig. 4.1, red squares) are $R_{\mathrm{deg,1}} = (10 \pm 2)\,\mathrm{h}^{-1}$ for the fast and $R_{\mathrm{deg,2}} = (0.7 \pm 0.2)\,\mathrm{h}^{-1}$ for the slow component. The slow component (2) therefore differs by a factor of up to 30 from R_{deg} of the BO-related degradation at the same temperature.

Note that the rate constants of the deactivation process (R_{reg}, regeneration of the lifetime) of the Cz-Si samples in Fig. 4.1 depend on FT, which is well-known from the literature [72, 73] and which is fully consistent with the faster regeneration at higher peak temperature observed in Fig. 4.1. We obtain R_{reg} under illumination at 80 °C and 1 sun of $(1.0 \pm 0.2)\,\mathrm{h}^{-1}$ (after firing at $FT = 750\,°\mathrm{C}$) and $(0.06 \pm 0.02)\,\mathrm{h}^{-1}$ (after firing at $FT = 550\,°\mathrm{C}$). The regeneration rate constant of LeTID after firing at $FT = 750\,°\mathrm{C}$ is $(0.02 \pm 0.01)\,\mathrm{h}^{-1}$. The scale factor $s(\Delta n)$, which we assumed in our discussion of the rate constants, will be explained in the following.

It has been shown that the kinetics of LeTID in mc-Si depend on the illumination intensity [74] or more precisely the excess carrier concentration Δn [75]. A constant illumination intensity during degradation – as it is applied in our experiments – results in a decreasing Δn and hence an a priori decreasing apparent degradation rate constant $s(\Delta n)R_{\mathrm{deg}}$. This leads to a somewhat stretched degradation of the mc-Si sample in Fig. 4.1. To state unchanging degradation rate constants R_{deg}, which can be identified as the apparent rate constants at $t = 0$ before degradation, we introduce a scale factor that subsumes the Δn dependence [76]. The same reasoning applies analogously to the apparent regeneration rate constant $s(\Delta n)R_{\mathrm{reg}}$. Though primarily a method to measure carrier lifetimes, the PCD method also yields a so-called implied open circuit voltage $V_{\mathrm{oc,implied}}$ at 1 sun for the measured lifetime data. Using Eq. (3.16), this $V_{\mathrm{oc,implied}}$ value can be translated into an excess carrier concentration Δn at 1 sun. The scale factor $s(\Delta n)$ is simply the Δn value at the time

t normalized to the initial Δn value at $t = 0$ before LeTID:

$$s = \frac{\Delta n(t)}{\Delta n(t=0)}, \qquad 0 \leq s \leq 1. \tag{4.4}$$

Figure 4.2 shows the improvements of fitting the effective defect concentration N_d^* of LeTID in mc-Si by applying $s(\Delta n)$. In Fig. 4.2(a), the excess carrier concentration Δn under one-sun illumination at 30 °C is shown (red squares, left axis) together with the scale factor (black line, right axis) derived from Δn. Figure 4.2(b) shows the same N_d^* (red squares) of LeTID in mc-Si already shown in Fig. 4.1(b). Whereas the dashed blue line shows a triple exponential fit as described in Eqs. (4.2) and (4.3) without use of the scale factor (i.e., $s = 1$), the solid black line applies $s(\Delta n)$. As clearly visible, the fit improves significantly, which, however, has also significant impact on the determined rate constants. Subsuming the Δn dependence of the apparent rate constants in $s(\Delta n)$, the degradation rate constants increase by a factor of 3 ($R_\mathrm{deg,1}$, fast component) and 60 ($R_\mathrm{deg,2}$, slow component). The regeneration rate constant R_reg increases by a factor of 2.

Unlike LeTID, R_deg of the BO degradation has been shown to be proportional to the square of the total hole concentration $p^2 = (p_0 + \Delta n)^2$ [77–80], whereas R_reg of the BO regeneration seem to be linearly dependent on Δn [81, 82]. This has been taken into account for the BO-specific scale factor $s(\Delta n) = s(p_0, \Delta n)$. Using $s(p_0, \Delta n)$, the degradation rate constant R_deg increases by a factor of up to 1.8 and the regeneration rate constant R_reg increases by a factor of up to 1.5. This significantly reduced impact of $s(p_0, \Delta n)$ on the BO-related degradation and regeneration in Cz-Si compared to the $s(\Delta n)$ impact on LeTID in mc-Si is due to the significantly reduced degradation extent resulting in less Δn variations.

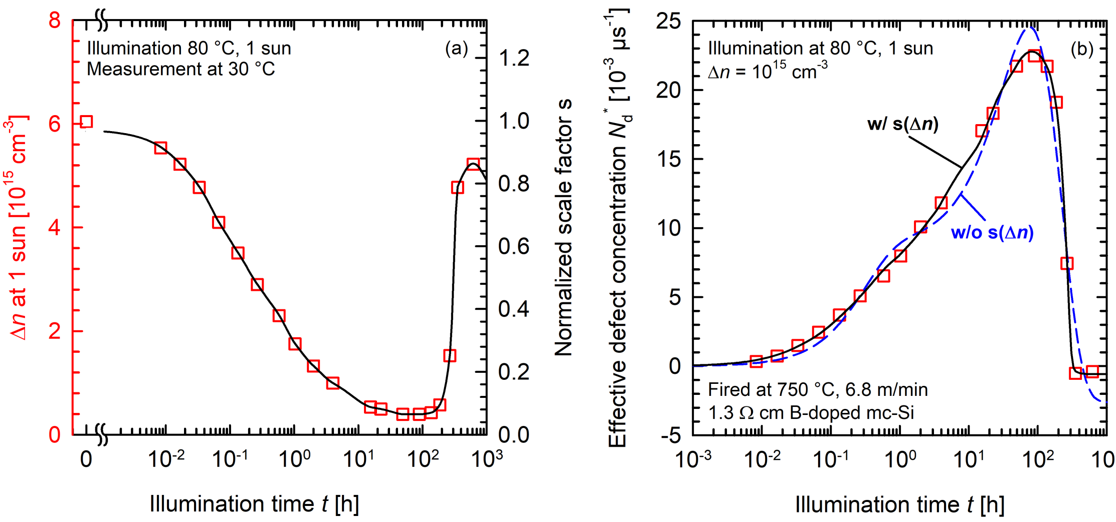

Figure 4.2: Improvement of fitting the effective defect concentration N_d^* of LeTID in mc-Si applying a scale factor $s(\Delta n)$ which subsumes the Δn dependence of the rate constants R_deg and R_reg. (a) Excess carrier concentration Δn under one-sun illumination at 30 °C in the mc-Si sample shown in Fig. 4.1 (red squares, left axis) together with the scale factor $s(\Delta n)$ normalized to $\Delta n(t = 0)$ (black line, right axis). (b) Corresponding defect concentration N_d^* (red squares) fitted using Eqs. (4.2) and (4.3) with (solid black line) and without (dashed blue line) applying the scale factor $s(\Delta n)$.

It is important to note that we determine Δn at 1 sun at the measurement temperature of the PCD method of ~30 °C instead of at the 80 °C applied in Fig. 4.1. The actual Δn value at the chosen illumination conditions would hence be expected to differ. However, since our aim is to approximate the normalized change of Δn due to changes in the carrier lifetime and not the absolute Δn under one-sun illumination at 80 °C, we expect the determined $s(\Delta n)$ to serve our goal reasonable well.
To characterize the activated defects further, we determine the hole-to-electron capture time constant ratio Q via the linearized Shockley-Read-Hall (SRH) lifetime [40, 83]. The SRH lifetime and the Q value are introduced in Section 2.2. Under the assumption of a deep-level defect, the SRH lifetime is given by [40]:

$$\tau_{\mathrm{SRH}} = \tau_{\mathrm{n0}} \left(1 + Q\frac{n}{p}\right), \tag{4.5}$$

with the ratio of electron and hole concentrations n/p and the capture time constant ratio $Q = \tau_{\mathrm{p0}}/\tau_{\mathrm{n0}}$. The obvious advantage of the SRH defect analysis in its linearized form is that a single defect manifests itself as a straight line. The Q value is determined at full degradation under the assumption of a single-level deep defect close to the middle of the band gap. The SRH lifetime (which is the inverse of N_{d}^{*}) is normalized using the capture time constant for electrons τ_{n0} to display the Q value as the gradient of the linear fit.

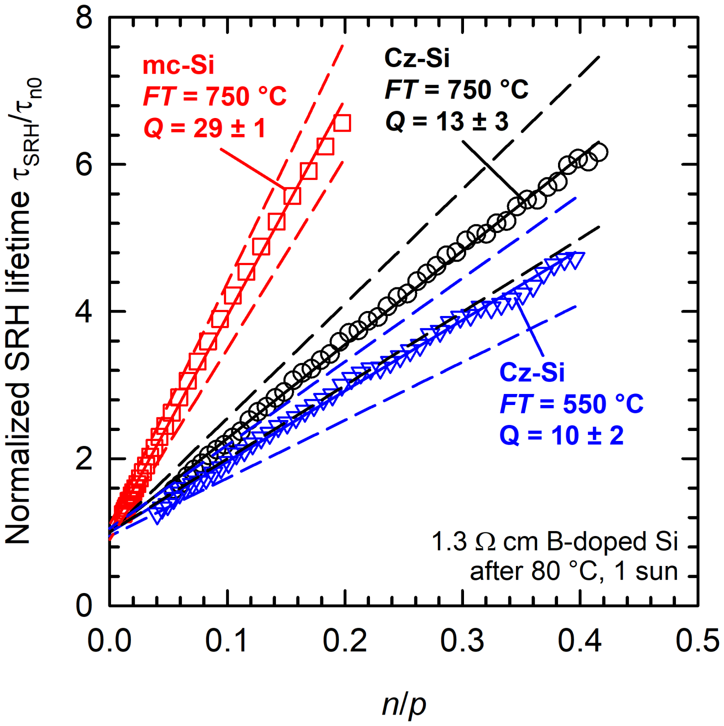

Figure 4.3: Normalized SRH lifetime $\tau_{\mathrm{SRH}}/\tau_{\mathrm{n0}}$ of the light-induced defect for two Cz-Si samples fired at different peak temperatures FT: 750 °C (black circles) and 550 °C (blue inverse triangles) as a function of n/p. The solid lines are linear fits of Eq. (4.5) to the measured data and the dashed lines indicate the measurement uncertainty. The Q values extracted for the Cz-Si samples are characteristic for the BO defect. For comparison, the SRH lifetime for the LeTID defect of an mc-Si sample fired at 750 °C (red squares) is shown, resulting in a significantly higher Q value.

The normalized SRH lifetime is plotted in Fig. 4.3 versus n/p for the Cz-Si samples, which were fired at an FT of 750 °C and 550 °C, respectively, and for the reference mc-Si sample fired at 750 °C. Since a second shallow defect is present in the mc-Si material, the analysis is only possible up to $n/p = 0.2$. The capture time constant ratio Q for the LeTID-specific defect of the mc-Si sample is determined as $Q = 29 \pm 1$, which is in excellent agreement with the literature [84, 85]. The Q value for the defect activated in the Cz-Si samples is $Q = 13 \pm 3$ for the higher and $Q = 10 \pm 2$ for the lower FT. Both values are in good agreement with the literature data of the BO defect, which is characterized by a Q value of $\sim$10 [86, 87]. The error margin is calculated with an assumed absolute error of the lifetime measurement of 10% (see dashed lines in Fig. 4.3).

Obviously, the lifetime of the examined Cz-Si samples is limited by the BO defect activation. To support this conclusion, Fig. 4.4 shows the injection-dependent lifetimes in the fully degraded state for both samples (black circles and blue inverse triangles). In addition, the fully degraded lifetime for a sample fired at 750 °C (green triangles) and illuminated under typical BO defect activation conditions of 30 °C and 0.1 suns for 160 h is shown (green triangles). The injection-dependent lifetimes of all three samples are practically identical. There are slight variations only at high injection levels, which is likely due to a variation in surface passivation and not related to the activation of a bulk defect.

Although only the results of one Cz-Si material are presented here, the same experiments were also conducted for two other Cz-Si materials of comparable base resistivities and processed in parallel, giving comparable results.

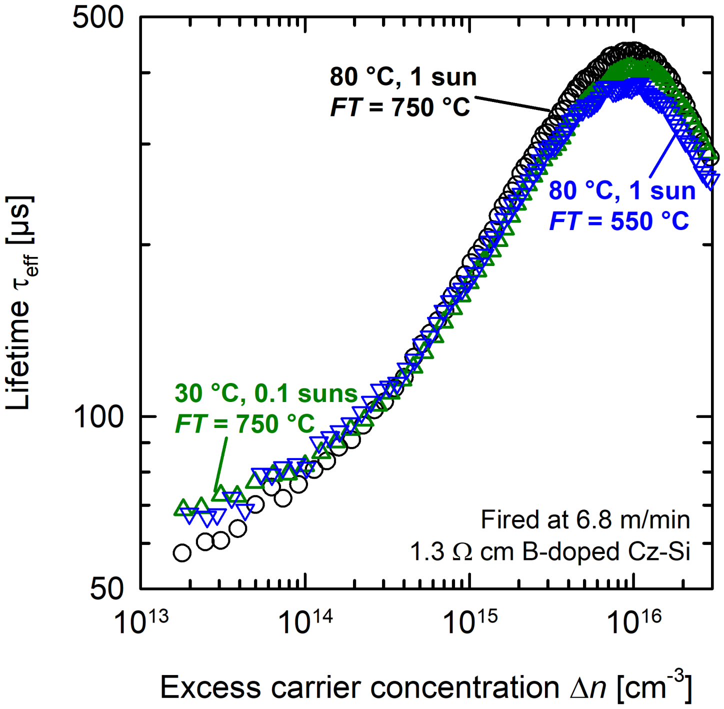

Figure 4.4: Injection dependent lifetimes in the fully degraded state for three different samples fired at an FT of 750 °C and 550 °C and illuminated either at 80 °C and 1 sun or at at 30 °C and at 0.1 suns.

4.4 Impact of the silicon nitride layer composition

It has been observed that the maximum concentration of the LeTID defect in mc-Si changes with varying refractive index n (related to the composition), and hence silicon content, of the hydrogen-rich SiN_y passivation layers, which was attributed to the increased amount of in-diffused hydrogen into the silicon bulk. The maximum in-diffused hydrogen concentration was observed for silicon-rich SiN_y layers with a refractive index of $n = 2.4$ [88]. Hydrogen is hence considered to be one of the major contributors to the LeTID effect in different silicon materials [19, 69, 88, 89].
In the previous section, we have shown that the lifetime of B-doped Cz-Si is dominated by the BO defect activation, if AlO_x/SiN_y stacks applying SiN_y layers with the industrially relevant refractive index of $n = 2.05$ are applied for passivation. In order to examine, whether an increased amount of in-diffused hydrogen increases the impact of a LeTID-like effect in the same material, the dielectric layers used for surface passivation of the Cz-Si samples were varied. On the one hand, the refractive index n (as measured by single-wavelength ellipsometry at $\lambda = 633\,\text{nm}$) of the SiN_y is changed from the typical value of $n = 2.05$ to very silicon-rich SiN_y with $n = 2.4$. On the other hand, the underlying AlO_x layer known to act as a diffusion barrier for hydrogen [90] was omitted in some samples. The results are displayed in Fig. 4.5.
The data recorded on the Cz-Si sample already discussed in Section 4.3 (80 °C, 1 sun, AlO_x/SiN_y ($n = 2.05$) stack, $FT = 750\,°\text{C}$) serve as a reference (black circles). The deactivation of the BO defect is completed after 45 h in the case of the single layer

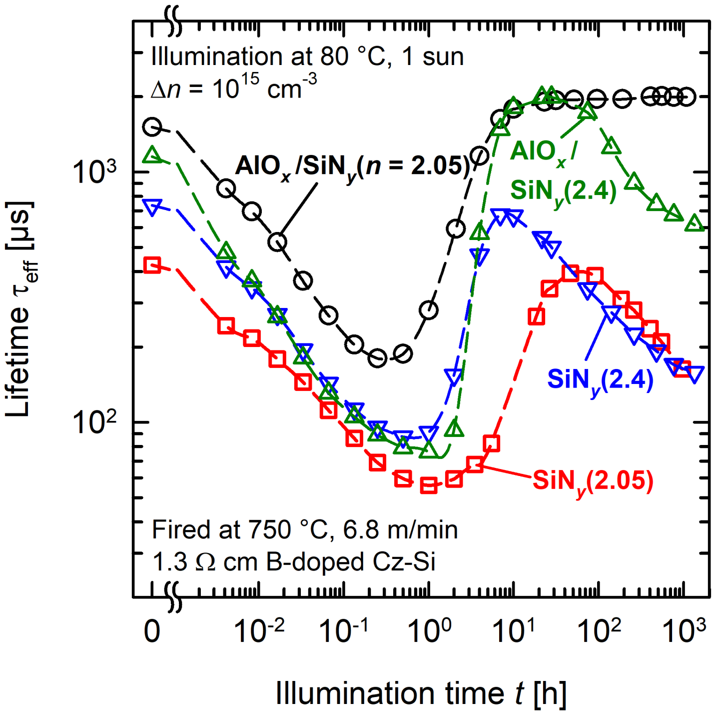

Figure 4.5: Effective lifetime τ_{eff} versus the cumulative exposure time to 1 sun and 80 °C. Results are shown for four Cz-Si samples coated with different depicted dielectric layers and fired at the measured peak temperature of 750 °C. The values in brackets denote the refractive index n (and hence the compositions) of the SiN_y layers applied.

SiN_y with a refractive index of $n = 2.05$ (red squares), but already much faster after 10 to 20 h for the silicon-rich single layer SiN_y with a refractive index of $n = 2.4$ (blue inverse triangles) and the AlO_x/SiN_y ($n = 2.4$) stack (green triangles). Interestingly, for these samples (in contrast to the reference sample shown as black circles in Fig. 4.5), we observe that after reaching the initial lifetime (or even a slightly higher lifetime value), the lifetime starts to degrade on the long term. This second degradation is still in progress for the samples after more than 1500 h at 80 °C and 1 sun.

An analysis of the capture time constant ratio Q of the first formed defect center (fully activated within 1 h at 80 °C and 1 sun) results in $Q = 16 \pm 5$ for the silicon-rich SiN_y ($n = 2.4$) and in $Q = 17 \pm 2$ for the AlO_x/SiN_y ($n = 2.4$) stack. These Q values are slightly outside the margin of the Q values reported in the literature for the BO defect [86, 87], which could be an indication for the contribution by another defect with increased Q, though the BO activation is dominant. For the $n = 2.05$ SiN_y single layer, however, the Q value is 12 ± 3, which is fully consistent with the BO defect.

In Fig. 4.6, the regenerated lifetimes after the full deactivation of the BO defect (closed green triangles and closed red squares, after 20 and 45 h, respectively) and the lifetime of the second degradation effect (open green triangles and open red squares, after 1400 and 1000 h, respectively) are shown for the AlO_x/SiN_y ($n = 2.4$)

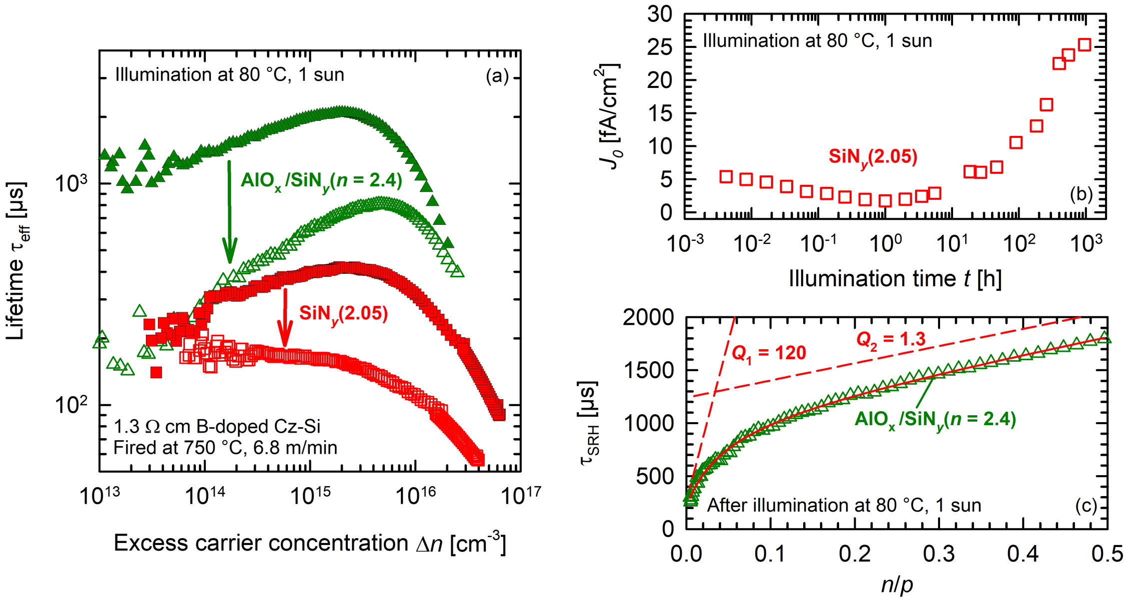

Figure 4.6: (a) Injection-dependent lifetimes of two samples coated with AlO_x/SiN_y ($n = 2.4$) and SiN_y ($n = 2.05$), respectively. The regenerated lifetimes (closed green triangles and closed red squares) and the lifetime curves of the second degradation (open green triangles and open red squares) visible in Fig. 4.5 are shown. In the case of SiN_y (2.05), the injection dependent lifetime measurements are carried out using two xenon flashes of different intensities of the PCD setup to broaden the accessible Δn range. (b) Saturation current density J_0 of the SiN_y (2.05) sample plotted over the cumulative time the sample was exposed to 80 °C and 1 sun. J_0 was extracted at around $\Delta n = 2 \times 10^{16}\,\mathrm{cm}^{-3}$ following the Kane and Swanson [45] approach. (c) SRH lifetime τ_{SRH} of the second defect of the AlO_x/SiN_y (2.4) sample after 1400 h of illumination as a function of n/p.

stack and the single layer SiN_y ($n = 2.05$) Cz-Si samples. Please note that the physical origins of the two observed degradation processes seem to be fundamentally different. Whereas the first relatively fast degradation visible in Fig. 4.5 is clearly a bulk-related effect with the activation of the BO complex being the dominant mechanism, a degradation of the surface passivation quality is largely responsible for the second degradation effect on the single layer silicon nitride samples, as evidenced by the injection dependence with a pronounced degradation at high injection densities (red squares in Fig. 4.6(a)). To characterize this degradation of the surface passivation quality, we use the saturation current density J_0 of a pseudo emitter on the wafer surfaces. A method to extract J_0 from injection-dependent lifetime measurements has been developed by Kane and Swanson [45] and has been introduced in Section 2.4. As shown in Fig. 4.6(b), the saturation current density J_0 extracted around $\Delta n = 2 \times 10^{16}\,\mathrm{cm}^{-3}$ increases by a factor of 5 during the 1000 h of illumination. The degradation in the surface passivation is also observed for the silicon-rich SiN_y ($n = 2.4$) sample. However, the activation of a bulk defect screened by the degradation of the surface passivation quality cannot be ruled out.

Importantly, the $\mathrm{AlO}_x/\mathrm{SiN}_y$ ($n = 2.4$) stack (green triangles in Fig. 4.6(a)) shows a very different behavior. The degradation is not visible in the high-injection regime, but at low injection levels and is therefore most likely caused by the activation of an additional bulk defect. However, the measured injection dependence is much weaker and therefore completely different from the one expected for the mc-Si-specific LeTID defect as well as of the BO defect. An analysis of the capture time constant ratio Q plotted in Fig. 4.6(c) reveals two defect states. Under the assumption of deep-level defects, the Q values can be determined to be $Q_1 = 120 \pm 60$ and $Q_2 = 1.3 \pm 0.5$. Please note that the square deviation was minimized to determine these Q values. Especially for Q_1, the determined value depends strongly on the selected injection range, which is the major reason for the large uncertainty. However, the Q value of the mc-Si-specific LeTID defect is $\sim$30, which is well outside the range of Q_1 and Q_2.

In order to examine the formation of the new type of Cz-defect on a shorter timescale, Fig. 4.7(a) shows the lifetime evolution of a Cz-Si sample coated with an $\mathrm{AlO}_x/\mathrm{SiN}_y$ ($n = 2.4$) stack at 1 sun and 185 °C. The Cz-Si sample is processed identically to the one discussed in Figs. 4.5 and 4.6. In contrast to the mono-exponential long-term degradation observed in Fig. 4.5 (green triangles), the degradation visible in Fig. 4.7(a) appears to be double-exponential. In Fig. 4.7(b), the injection-dependent lifetime is depicted for the initial state of the long-term degradation (after 8 min at 185 °C and 1 sun, black circles), the intermediate state after 93 h (blue inverse triangles) and the fully degraded state after 781 h (red squares). The SRH defect analysis of the intermediate state after illumination for 93 h (not shown here) reveals Q values in the same range as in Fig. 4.6(c), that is $Q_1 = 80 \pm 40$ and $Q_2 = 1.5 \pm 0.5$. After complete degradation, we extract the same Q values, shown in Fig. 4.7(c), of $Q_1 = 80 \pm 40$ and $Q_2 = 1.4 \pm 0.5$. Both recombination centers are possibly two different states of the same chemical defect of unknown composition.

We observe this second pronounced degradation only under use of a rather untypical SiN_y layer with a refractive index of $n = 2.4$ on a very long timescale of thousands of hours at the elevated temperature of 80 °C and higher. In the next Section 4.5, we will therefore focus on the firing-triggered LeTID-like defect that is activated on

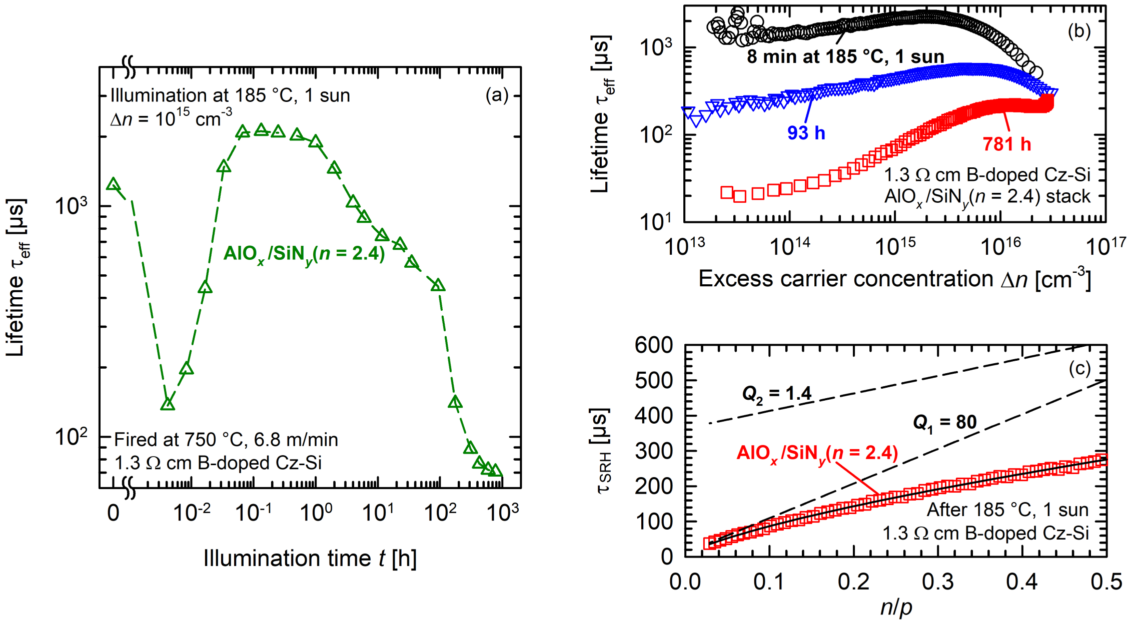

Figure 4.7: (a) Effective lifetime τ_{eff} versus the cumulative exposure time to 1 sun and 185 °C of a sample coated with an $\text{AlO}_x/\text{SiN}_y$ ($n = 2.4$) stack. The dashed line serves as guide to the eyes. (b) Injection-dependent lifetime of the sample after 8 min (black circles), 93 h (blue inverse triangles) and 781 h (red squares) at 1 sun and 185 °C. (c) SRH lifetime τ_{SRH} of the second defect of the $\text{AlO}_x/\text{SiN}_y$ ($n = 2.4$) Cz-Si sample after 781 h at 1 sun and 185 °C as a function of n/p.

the same timescale as the BO defect. We will separate them to study their different properties.

4.5 Separation of LeTID and BO-related degradation

A short time anneal of 10 min at 200 °C in the dark (Dark Anneal, DA) is known to temporarily deactivate the BO complex [6]. In this section we want to examine the impact of DA steps on the formation of LeTID in B-doped Cz-Si and investigate the possibility to use DA to separate LeTID and BO defect activation.
Figure 4.8 shows the lifetime evolution of Cz-Si samples, which received the following treatments after processing: Halogen lamp illumination (1 sun) at 80 °C to activate the BO defect, followed by a DA step at 200 °C for 10 min to deactivate the BO complex [6]. This experiment is repeated several times. The lifetime is shown after illumination and subsequent annealing for each iteration. Figure 4.8(a) shows the lifetime evolution of a sample, which received no firing step but was merely annealed at 425 °C for 15 min. There is no significant change in the lifetime visible after each cycle. The behavior of a fired Cz-Si sample in Fig. 4.8(b) is quite different. Besides the BO defect (fast oscillation between upper and lower state), there is a distinct second slower degradation and a subsequent regeneration in the lifetime, which is visible in the enveloping curves (blue inverse triangles). By reference measurements with varying experimental parameters (i.e., DA and illumination times), we ensured that neither a beginning regeneration of the lifetime due to BO deactivation under illumination nor an incomplete deactivation of the BO effect under DA has any impact on the additional degradation/regeneration effect. This LeTID-type degra-

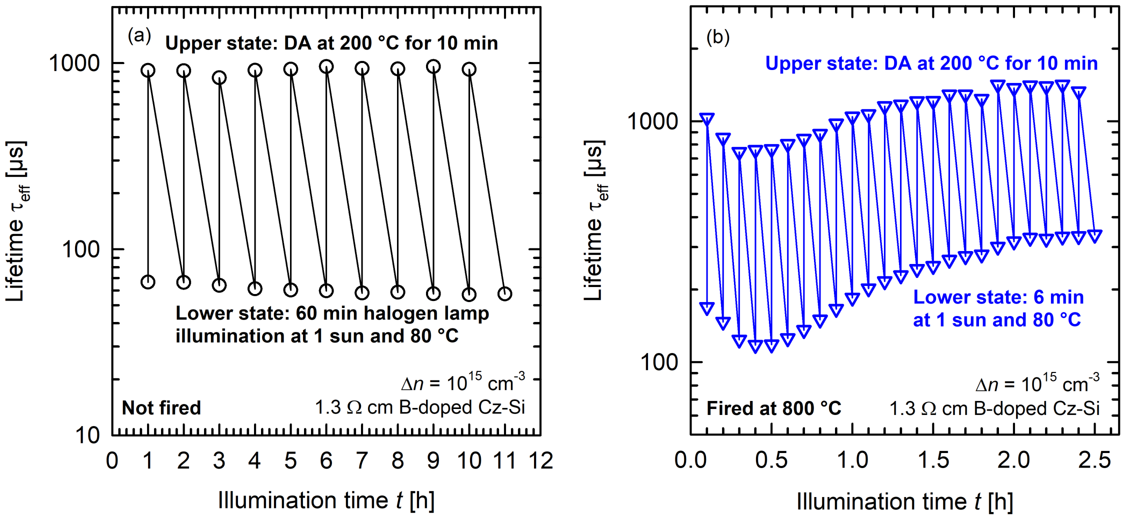

Figure 4.8: Repeated BO activation/deactivation cycles of B-doped Cz-Si lifetime samples. The BO complex is activated by illumination at 1 sun and 80 °C and, after full BO activation, is then deactivated by a dark anneal (DA) at 200 °C for 10 min. The effective lifetime τ_{eff} extracted at $\Delta n = 10^{15}\,\text{cm}^{-3}$ is plotted versus the cumulative illumination time t. (a) The lifetime sample was merely annealed at 425 °C for 15 min after $\text{AlO}_x/\text{SiN}_y$ passivation (i.e., no fast-firing step was applied). (b) The wafer from which the sample was cut was fired at an FT of 800 °C after $\text{AlO}_x/\text{SiN}_y$ passivation. The firing step triggers a slow non-BO-related lifetime degradation and regeneration, as shown by the enveloping curves.

dation effect is only observed after high-temperature firing. The time constant – the inverse of the degradation rate constant used before in this chapter – of LeTID in Cz-Si is in the range between 0.3 and 0.5 h at 80 °C and 1 sun. The LeTID degradation time constant of our mc-Si reference wafer amounts to 1.5 h at 80 °C and 1 sun (cf. Fig. 4.1, assuming a scale factor $s(\Delta n)$). The time constants hence differ by a factor of ~4. Please note that assuming $s(\Delta n)$ for Cz-Si samples would have no impact on the time constant due to the relatively small LeTID extent.

Note furthermore that the difference in the illumination time between the non-fired sample in Fig. 4.8(a) and the fired sample in Fig. 4.8(b) is due to the onset of the lifetime regeneration in the fired sample. If, however, the same experimental conditions are applied to a non-fired sample (i.e., halogen lamp illumination for only 6 min at 80 °C within each cycle), there is no change of the lifetime in the activated or deactivated state of the BO complex visible for the first hour of cumulative illumination time (i.e., during 10 cycles). We have chosen the representation in Fig. 4.8(a) (i.e., 60 min illumination intervals) because it shows the stability of the BO defect activation/deactivation over a longer period.

Fig. 4.9 shows the impact of the DA or the illumination periods. Whereas the blue inverse triangles in Fig. 4.9(a) show the same data as Fig. 4.8(b), a DA step of only 5 min, instead of the usual 10 min, is applied in between the illumination for the sample represented by the red squares. The illumination period of 6 min at 80 °C remains identical for both samples. The repeated dark annealing in-between seems to have no impact, since halving of the DA time (red squares) does not change the time constant of the long-term degradation/regeneration. Only the deactivated lifetime after each DA step is lower after DA for only 5 min (Fig. 4.9(a), red squares) instead

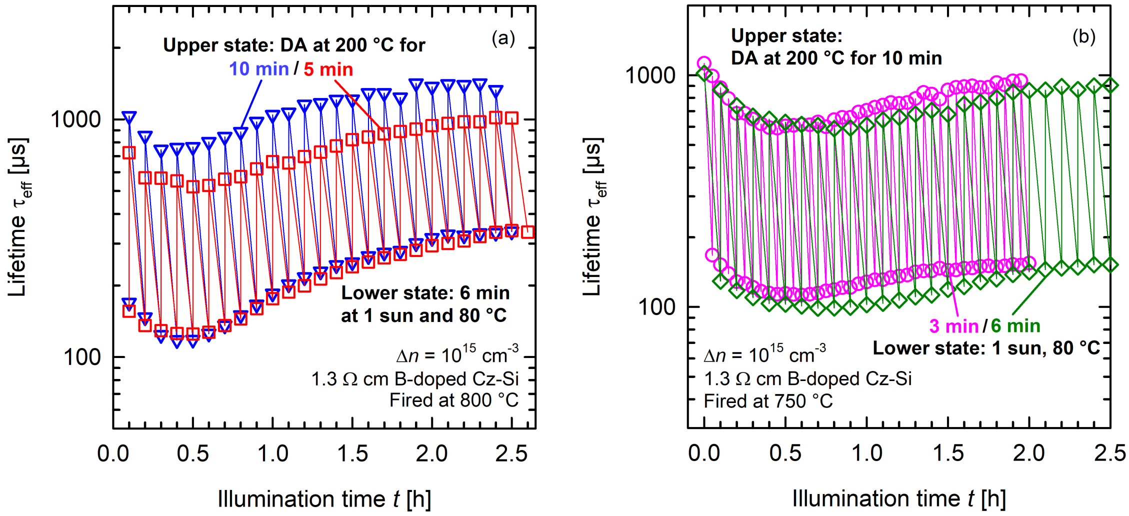

Figure 4.9: Repeated BO activation/deactivation cycles of fired B-doped Cz-Si lifetime samples. The BO complex is activated by illumination at 1 sun and 80 °C and deactivated by a dark anneal (DA) at 200 °C. The effective lifetime τ_{eff} extracted at $\Delta n = 10^{15}\,\text{cm}^{-3}$ is plotted versus the cumulative illumination time t. (a) Whereas the blue inverse triangles represent the same data already presented in Fig. 4.8(b) (i.e., DA at 200 °C for 10 min), the red squares show τ_{eff} of a sister sample which receives the same DA step for only 5 min alternating with the illumination. The period of the DA seems to have no impact on the LeTID effect. (b) Variation of the illumination time at 80 °C. Whereas the sample represented by the green diamonds is illuminated for 6 min at 80 °C alternating with DA, the sister sample (pink circles) is illuminated at intervals of only 3 min. It cycles therefore twice as often alternately through DA and illumination within the same cumulative illumination time t. There is no impact of the illumination interval visible on the time constant of the LeTID activation.

of 10 min (Fig. 4.9(a), blue inverse triangles), which is, in this case, consistent with an incomplete BO deactivation.

In Fig. 4.9(b), the illumination time t is varied, whereas the DA time in-between remains identical for both samples. Unfortunately, this experiment had to be conducted on samples which were fired at a slightly lower measured peak temperature of 750 °C instead of 800 °C. Since we did not vary the peak firing temperature systematically, we refrain from drawing conclusions from differences between the Figs. 4.9(a) and 4.9(b) regarding time constants and extent of the lifetime degradation. For the sample illuminated for 6 min within each cycle (green diamonds) the time constant of the LeTID degradation is (0.4 ± 0.2) h, for the sample illuminated for only 3 min (pink circles) it is (0.3 ± 0.1) h at 80 °C and 1 sun (determined for the deactivated lifetimes). We conclude that no impact of the illumination interval can be observed. Importantly, the LeTID effect in Cz-Si does not only occur at elevated temperatures (e.g., at 80 °C), but also at lower temperatures (i.e., at $\sim$30 °C). Figure 4.10(a) shows the firing-triggered LeTID-type effect observed at 30 °C and 0.1 suns light intensity. Compared to the illumination at higher intensity and temperature in Fig. 4.8(b), the time constant is significantly larger, as is to be expected of any thermally activated degradation process. Interestingly, the degradation effect is much more pronounced at 30 °C and 0.1 suns than at higher temperature and intensity, which could either indicate that two independent, parallel processes are responsible for the activation and deactivation of the defect, or that the LeTID effect

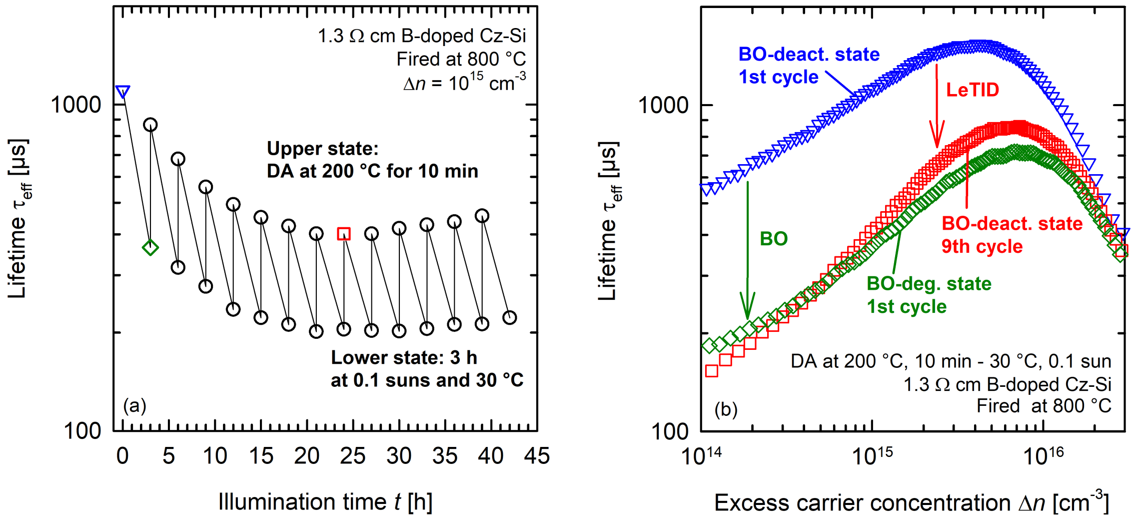

Figure 4.10: (a) Repeated BO deactivation/activation cycles of a Cz-Si sample at 30 °C and 0.1 suns for a fired Cz-Si sample. The LeTID effect is clearly visible as enveloping curves in addition to the BO deactivation/activation oscillations. (b) Injection-dependent lifetimes for the BO and the LeTID effect, activated at 30 °C and 0.1 suns. The blue inverse triangles represent the deactivated state of both degradation effects. Whereas the BO defect is activated for 3 h (green diamonds), the LeTID defect needs 24 h under the same condition to be fully activated (red squares). The positions within our experiment of the three injection-dependent lifetimes in (b) are highlighted in (a) with matching colors and symbols.

is dependent on the injected carrier concentration Δn. In contrast, there are reports that the LeTID effect in mc-Si materials is temporarily deactivated by illumination at 25 °C [20, 91].

To characterize the electronic properties of LeTID in B-doped Cz-Si and to differentiate it from the BO defect, we examine the sample treated at room temperature (Fig. 4.10(a)) in more detail. The LeTID effect is much more pronounced at 30 °C and 0.1 suns than at our standard illumination conditions of 80 °C and 1 sun. Therefore, differences are more evident and the characterization of electronic properties can be performed with less uncertainty.

The injection-dependent lifetime of the three highlighted states in Fig. 4.10(a) is shown in Fig. 4.10(b). The blue inverse triangles depict the initial state after sample processing and the very first DA step at 200 °C for 10 min. Therefore, it represents the deactivated state of both the BO and the LeTID defect. The degraded (activated) state of the BO defect (Fig. 4.10(b), green diamonds) after 3 h illumination time at 30 °C and 0.1 suns is taken from the very first activation/deactivation cycle. Note that 3 h of room temperature illumination were not sufficient to fully activate the BO complex. For the characterization of the electronic properties, however, this does not matter. The degraded state of the LeTID effect (Fig. 4.10(b), red squares) is taken from the 9th BO activation/deactivation cycle, directly after the DA step. The BO defect is therefore in its deactivated state, the lifetime degradation in comparison to the lifetime curve represented by the blue inverse triangles can hence be completely attributed to the LeTID defect. As clearly visible in Fig. 4.10(b), the BO- and the LeTID-related lifetimes differ in their injection dependencies. The LeTID-limited lifetime shows a more pronounced injection dependence compared to the BO-related lifetime. To compare this quantitatively, we determine the hole-to-electron capture time constant ratio Q via the linearized SRH lifetime [40, 83] as introduced in Eq. (4.5) and explained in more detail in Section 2.2. The Q value of the BO defect is determined to $Q_{\mathrm{BO}} = 10 \pm 2$, which is in agreement with the literature [86, 87]. The Q value of the LeTID effect is determined to $Q_{\mathrm{LeTID}} = 23^{+9}_{-5}$. The uncertainty margin is calculated with an assumed absolute uncertainty of the lifetime measurement of 5%. The large uncertainty range of Q_{LeTID} is due to the relatively small differences between the measured lifetimes in the deactivated and the activated defect state. Note that Q_{LeTID} is in the range we would also expect from the LeTID effect in mc-Si [84, 85].

4.6 Impact of BO regeneration

Both the BO-related degradation [71–73] as well as LeTID [12, 13] are known to regenerate under prolonged illumination at elevated temperatures. To continue our investigation of the impact of short-time DA steps on LeTID, we apply repeated regeneration/DA cycles on both B-doped Cz-Si and mc-Si samples. Fung et al. [92] reported that the fully degraded lifetime after LeTID in mc-Si increases when exposed to repeated regeneration/DA cycles. The authors attributed this increase of the LeTID-limited lifetime to a speculative hydrogen reservoir state [92].

In Fig. 4.11, measured lifetimes in different defect states are shown for (a) a fired Cz-Si and (b) a fired mc-Si sample. In contrast to Section 4.5, the illumination (at the applied temperatures) is continued after degradation until the respective main degradation effects – that is BO-related degradation for Cz-Si and LeTID for mc-Si – are fully regenerated before applying a DA step and repeating the experiment. Since there are three well-defined points for each regeneration/DA cycle, the data is presented in three plots within Figs. 4.11(a) and 4.11(b). These are (1) the measured effective lifetimes τ_{eff} in the fully degraded state (open blue inverse triangles), (2) the regenerated state (red squares) and (3) the measured effective lifetime after subsequent DA at 200 °C for 10 min (black circles). As before, the data is plotted versus the cumulative illumination time.

It is immediately apparent that τ_{eff} of the fully degraded state of the Cz-Si sample increases significantly from initially 140 µs (first degradation) to 300 µs after the second degradation cycle (Fig. 4.11(a), blue inverse triangles, ∼20 h). This is related to the regenerated state of the LeTID effect as shown in Fig. 4.8(b) (after ∼2.5 h, lower state). As pointed out in Section 4.5, the LeTID effect in Cz-Si is not influenced by repeated DAs, which is why such a significant lifetime change of the fully degraded state only occurs once in Fig. 4.11(a). Afterwards, the effective lifetime in the degraded state is almost stable and shows only a minor decrease with increasing number of cycles or, equivalently, increasing cumulative illumination time. Since an increase in the surface recombination current density J_0, a measure for the surface passivation quality of our samples [45], can be observed simultaneously (Fig. 4.11(c)), we determine the bulk lifetime to examine, if this small decrease of the effective lifetime is related to an increasing recombination at the surfaces. To

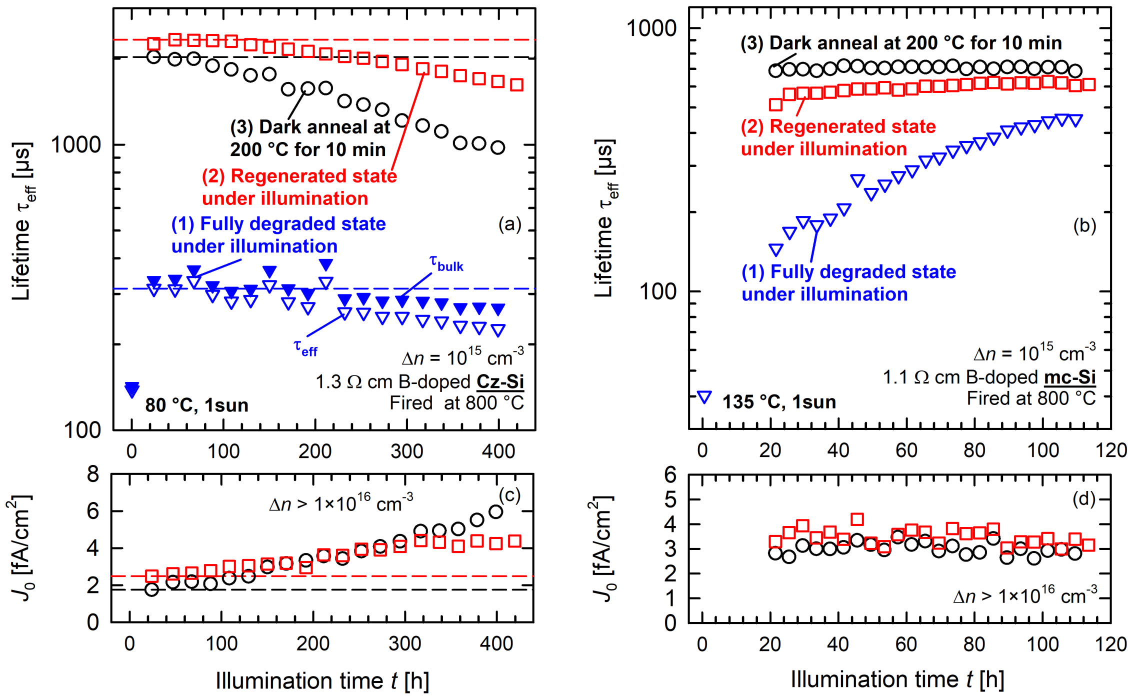

Figure 4.11: (a) Measured effective lifetimes τ_{eff} of a fired B-doped Cz-Si sample in different BO states: (1) after full BO activation at 80 °C and 1 sun (open blue inverse triangles), (2) after full regeneration at 80 °C and 1 sun (red squares), and (3) after subsequent dark annealing (DA) at 200 °C for 10 min (black circles). In addition, the bulk lifetime τ_{bulk} in the fully degraded state is shown (filled blue inverse triangles), according to Eq. (4.6) and the J_0 data shown in (c). The data is plotted versus the cumulative illumination time t. (b) Measured effective lifetime τ_{eff} of a fired B-doped mc-Si sample in three different states: (1) after full LeTID activation at 135 °C and 1 sun, (2) after regeneration at 135 °C and 1 sun, and (3) after subsequent DA at 200 °C for 10 min. In (c) and (d), the respective recombination current densities J_0 [45] are shown for the samples above. Colors and symbols match the experimental states in (a) and (b).

determine the bulk lifetime, we use the equation:

$$\tau_{\text{bulk}} = \left(\frac{1}{\tau_{\text{eff}}} - \frac{2J_0(N_{\text{dop}} + \Delta n)}{en_{\text{i}}^2 W}\right)^{-1}, \tag{4.6}$$

with the base doping N_{dop}, the elementary charge e, the intrinsic carrier concentration n_{i}, and the sample thickness W. Please refer to Chapter 2 for more details on Eq. (4.6). Note furthermore that Eq. (4.6) is valid only if the surface passivation can be described by a single J_0 value, which we assume here. The bulk lifetime τ_{bulk} of the fully degraded state for the Cz-Si sample is shown in Fig. 4.11(a) (filled blue inverse triangles). The corresponding J_0 values used to determine τ_{bulk} are shown in Fig. 4.11(c) (black circles). As can be seen from Fig. 4.11(a), the major part of the lifetime decrease for the Cz-Si sample is due to the surface-related degradation and only a negligible part to the bulk. The surface-related lifetime degradation is most likely caused by the repeated DA steps, since there is no such behavior observable on Cz-Si reference samples simply illuminated at 80 °C and 1 sun for at least 1000 h (cf. Fig. 4.1), black circles).

Fig. 4.11(b) shows the same kind of experiment for an mc-Si sample. As before, the main regeneration/DA effect – which is clearly LeTID in this case – can be observed repeatedly when applying the DA step after complete regeneration under illumination. Again, a significant increase of the fully degraded lifetime from 40 µs to 150 µs is visible after the first iteration (Fig. 4.11(b), blue inverse triangles, ∼20 h). This correlates, however, with a significant reduction in the period required for a complete regeneration of the LeTID effect. Whereas the first regeneration/DA cycle takes 20 h, all following cycles take ∼4 h to completely regenerate the LeTID effect after the DA was applied. Moreover, the lifetime increase in the fully degraded state continues until the 24th iteration, which was the end of our experiment. This increase of the LeTID-limited lifetime in mc-Si with increasing number of cycles has already been reported before by Fung et al. [92], the authors attributed it to a speculative hydrogen reservoir state. Note that there is no significant change of the surface passivation quality visible (Fig. 4.11(d)). Thus, the increasing LeTID-related lifetime is clearly bulk-related.

As opposed to this, the Cz-Si sample in Fig. 4.11(a) shows no hydrogen-reservoir-like behavior. Apart from the very first increase between the first and second cycle the fully degraded bulk lifetime is constant or even slightly decreasing with increasing number of cycles (state (1) in Fig. 4.11(a)).

Note that the temperature for the mc-Si sample was chosen higher (135 °C) during the regeneration/DA experiment than for the Cz-Si samples (80 °C) due to significantly faster regeneration/DA rates at higher temperatures, reducing the period of our investigations.

4.7 Conclusions

In this chapter, we have performed a series of carrier lifetime experiments at different temperatures to examine LeTID in boron-doped Cz-Si. Most of our samples were coated symmetrically with an AlO_x/SiN_y stack on the front an rear surface, where the SiN_y layer had a refractive index of $n = 2.05$. These samples were then fired in a conventional conveyor belt furnace. This fast-firing is known to trigger the LeTID effect in mc-Si due to the in-diffusion of hydrogen from the hydrogen-rich SiN_y layers on the wafer surfaces into the silicon bulk. Hydrogen is believed to be one essential component causing LeTID in mc-Si. Although we provided optimal conditions for the activation of the LeTID defect, as shown on reference samples processed on mc-Si wafers, our illumination experiments showed no indication of the activation of the mc-Si-specific LeTID defect in boron-doped Cz-Si. The lifetime at all times under illumination was limited by the activation of the BO defect. We proved this conclusively by comparing the lifetime degradation and regeneration behavior with the activation of the mc-Si-specific LeTID on in parallel processed mc-Si samples. The degradation rate constants R_{deg} differ by up to a factor of 30, even after introducing a scale factor $s(\Delta n)$ that subsumes the Δn-dependence of degradation. The capture time constant ratios Q differ by a factor ∼3. Nevertheless, in Cz-Si wafers coated with very silicon-rich SiN_y layers ($n = 2.4$), which are known to introduce a maximum amount of hydrogen into the silicon bulk, we in fact determined Q values outside the margin reported for the BO defect in the literature, but on the same timescale as observed for the BO defect activation. Although the BO defect activation obviously remains dominant for these samples as well, a certain influence of a defect with a higher Q value seems likely. Furthermore, we observed the formation of another type of bulk defect on the long term. This defect showed very different recombination parameters compared to the mc-specific-LeTID defect, and can hence be considered as a different kind of (probably hydrogen-related) defect. For the application of typical SiN_y layers, no LeTID effect beyond the BO defect activation was observed to limit the lifetime in boron-doped Cz-Si under illumination.

However, through BO activation/deactivation cycles by alternating an illumination and a dark annealing (DA) step, we were able to separate the BO defect activation from a firing-triggered LeTID-type defect in samples coated with stacks of AlO_x and typical SiN_y ($n = 2.05$) layers. Comparing lifetime measurements on non-fired and fired samples, we were able to show that, besides the well-known BO LID, a second degradation effect is occurring in the bulk of fired Cz-Si samples. This LeTID effect occurs not only at elevated temperatures (80 °C, 1 sun), but is even more pronounced at low temperatures (i.e., 30 °C) and low illumination intensities (i.e., 0.1 suns). Note that the LeTID effect on mc-Si seems to be temporarily deactivated by illumination at low temperatures near room temperature. The extracted hole-to-electron capture time constant ratio Q of the LeTID defect in Cz-Si is 23^{+9}_{-5} and therefore higher than the Q value of the BO defect, which equals 10 ± 2 and was determined on the same samples. Compared to the LeTID defect which occurs in fired mc-Si materials, there are some important differences to the LeTID defect in Cz-Si. First, the time constants of the defect activation differ by a factor of $\sim$4, suggesting a different detailed defect physics behind both degradation effects. More importantly, however, in a second series of experiments, we showed that the LeTID effect in mc-Si, unlike the LeTID effect in Cz-Si, is strongly influenced by the DA steps, as has also been reported by Fung et al. [92], who attributed this effect to a speculative hydrogen-reservoir state, which is not observed on our Cz-Si samples.

Nevertheless, since the LeTID on both B-doped mc-Si and Cz-Si is clearly triggered by firing, it is most likely that both degradation effects are hydrogen-related, however, the detailed defect physics seem to be different.

5 Light- and elevated-temperature-induced degradation in gallium-doped Czochralski-silicon

5.1 Introduction

Light-induced lifetime degradation effects are frequently observed in crystalline silicon materials for solar cell production. One of the most prominent ones is caused by the electron-induced activation of a boron-oxygen (BO) defect, typically occurring in boron-doped Czochralski-grown silicon (Cz-Si) [6–8, 93]. Another degradation effect is the so-called 'light- and elevated-temperature-induced degradation' (LeTID), first observed on block-cast multicrystalline silicon (mc-Si) [10, 11, 94]. In contrast to the BO-related degradation effect, the occurrence of the LeTID effect requires a previous fast-firing step at a high peak temperature [14, 66, 95]. There have been reports of LeTID-type effects in boron-doped Cz-Si [15, 16, 67], in float-zone silicon (FZ-Si) [17, 19] and in n-type Cz-Si [69]. More recently, lifetime instabilities on fired gallium-doped Cz-Si wafers and solar cells have been reported too [96–98]. Ga-doped Cz-Si materials – the most recently introduced Cz-Si material into the large scale cell production – has been dominating the p-type mono-Si market for only a couple of years. According to data of the International Technology Roadmap for PV, boron as dopant for p-type material disappears in 2023 [22]. This is due to the absence of BO degradation and a significantly reduced degradation extent.

The extent of lifetime degradation differs with the material and the dominant defect activated within the bulk of the material. Figure 5.1 shows the degradation and regeneration effects observed at 80 °C and 1 sun on the three main p-type materials used in the solar industry within the last decade, which are B-doped Cz-Si (Cz-Si:B, black circles), B-doped mc-Si (mc-Si:B, blue inverse triangles), and Ga-doped Cz-Si (Cz-Si:Ga, red triangles). In addition, the lifetime evolution of B-doped float-zone silicon (FZ-Si:B, pink squares) is shown as a reference, because it is the most defect-lean silicon material.

The LID observed on the Cz-Si:B sample within 0.25 h can be ascribed to the activation of BO defects. The degradation is followed by a regeneration of the lifetime within 10 h under the same conditions. Although we were able to show the impact of a LeTID-type defect on a similar timescale as the BO defect formation, the BO defect is clearly dominant (cf. Chapter 4). The blue inverse triangles show the typical LeTID effect on mc-Si:B, but a high-temperature firing step is necessary for LeTID to occur [13, 14, 95]. Contrary to these pronounced degradation phenomena, the degradation extent of similarly processed Cz-Si:Ga (red triangles) and FZ-Si:B (pink squares) samples is significantly lower at high lifetime levels under illumination at 80 °C and 1 sun.

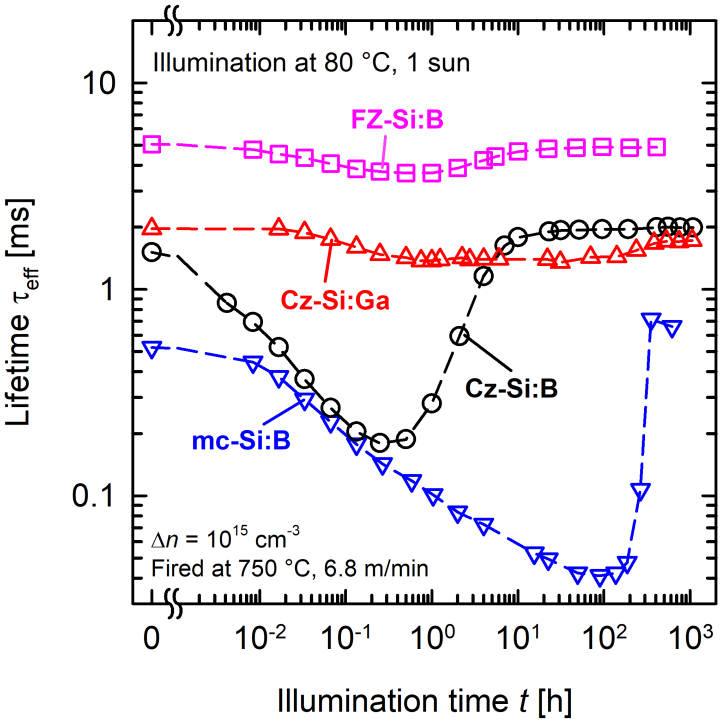

Figure 5.1: Effective lifetime $\tau_{\mathrm{eff}}(t)$ of different p-type silicon materials under illumination at 80 °C and 1 sun for up to 1000 h. Shown are degradation and regeneration behavior of B-doped Cz-Si (black circles), B-doped mc-Si (blue inverse triangles), Ga-doped Cz-Si (red triangles), and B-doped FZ-Si (pink squares). Whereas a pronounced degradation occurs in mc-Si:B and Cz-S:B due to the LeTID effect and the BO pair formation, respectively, the degradation extent in both Cz-Si:Ga and FZ-Si:B is significantly lower under illumination at 80 °C and 1 sun.

In this chapter, we examine the degradation in Cz-Si:Ga in detail through a series of carrier lifetime experiments. As a reference, we study FZ-Si:B, as the most defect-lean silicon material available today. Both materials are for different reasons (no B-doping in case of Cz-Si:Ga, very low oxygen contamination in FZ-Si:B) not prone to BO degradation and are therefore excellent test objects for detailed degradation experiments of firing-triggered degradation phenomena.

5.2 Experimental details

Symmetrical lifetime samples were processed on 1 Ω cm Cz-Si:Ga and 1.2 Ω cm FZ-Si:B wafers. The saw damage of the wafers was removed in a KOH solution before cleaning them in a standard RCA sequence. Subsequently, a double-sided phosphorus diffusion is performed in a quartz-tube furnace at a process temperature of 829 °C. The resulting phosphosilicate glass and the n^+-layers on both wafer surfaces are removed by an HF dip and a short etch step in a KOH solution. After another RCA cleaning, both wafer surfaces are symmetrically coated with AlO_x/SiN_y stacks. First, 10 nm of aluminum oxide (AlO_x) are deposited by plasma-assisted atomic layer deposition (Oxford Instruments, FlexAL). Subsequently, (100 ± 5) nm of silicon nitride (SiN_y) with a refractive index of $n = (2.05 \pm 0.02)$ are deposited on top by plasma-enhanced chemical vapor deposition (PECVD, Meyer Burger, SiNA).

The silicon nitride films of (120 ± 3) nm for a variation of the refractive index n on both Cz-Si:Ga and FZ-Si:B are deposited using another PECVD tool (Oxford Instruments, Oxford Plasmalab 80 Plus). The thicknesses as well as the refractive indices n of (2.07 ± 0.02), (2.24 ± 0.02), and (2.37 ± 0.03) are determined using spectrally resolved ellipsometry measured at various angles of incidence (M2000UI, J.A. Woollam). The refractive indices are reported at a constant wavelength of 633 nm. As a reference, some wafers are annealed at 425 °C for 15 min to activate the surface passivation without a fast-firing step. The remaining wafers receive a firing treatment in an industrial conveyor-belt furnace (centrotherm international, DO-FF-8.600-300) at belt speeds v_{band} between 2.8 and 7.2 m/min and set-peak firing temperatures ranging from 750 °C to 900 °C, resulting in measured peak firing temperatures FT between 630 °C and 800 °C. Standard firing conditions, whose variations of FT and v_{band} we examine on Cz-Si:Ga in Section 5.4, are $FT = 750\,°\mathrm{C}$ and $v_{\text{band}} = 6.8\,\mathrm{m/min}$. We will always refer to the actual FT measured on the wafer surfaces using a temperature tracker (Datapaq DQ1860A) and a type-K thermocouple (Omega, KMQXL-IM050G-300). The reported FT values have an uncertainty of ±10 °C. After firing, the wafers are cut into 5 cm × 5 cm samples using a laser process. The final thickness of all samples is (150 ± 10) µm.

After finishing the processing, the samples receive the following treatment: Halogen lamp illumination on a hot plate at elevated temperatures between 70 °C and 160 °C at an illumination intensity of typically 1 sun (100 mW/m^2) until the degraded state is reached (i.e., the defect is fully activated). We examine the impact of the illumination intensity on the degradation effect in Section 5.7 for intensities ranging from 0.1 to 1 sun. We measure the illumination intensity with a calibrated reference silicon solar cell. The lateral variation of the illumination intensity is less than ±0.05 suns, while the temperature during illumination is constant within a range of ±2 °C. In order to deactivate the defect, the lifetime samples are illuminated at 0.5 suns for up to 30 min at a reduced sample temperature of (44 ± 4) °C. Our preliminary investigations had shown that defect deactivation occurs under these conditions. Note that this temperature of (44 ± 4) °C is a consequence of the halogen lamp illumination itself and measured on reference samples with a digital thermometer (RS Components, RS 206-3750) and a type-K temperature probe (Testo AG, TE type-K). For selected samples, the degradation experiments are repeated several times, either at the same or each time at a different temperature during degradation.

We measure the effective lifetime (τ_{eff}) of the samples at (30 ± 2) °C by the photoconductance decay (PCD) method using a WCT-120 lifetime tester from Sinton Instruments (transient mode), the operating principle of which is explained in detail in Section 3.1. If not stated otherwise, the lifetimes are reported at an excess carrier concentration of $\Delta n = 10^{15}\,\mathrm{cm}^{-3}$.

5.3 Temperature-dependent degradation

Figure 5.2 shows the degradation effects observed in the Cz-Si:Ga samples at temperatures ϑ ranging from 90 °C (black circles) to 140 °C (pink hexagons). Figure 5.2(a) shows the measured effective lifetime τ_{eff} as a function of illumination time t at 1 sun illumination intensity. The corresponding evolution of the effective defect concentration $N_{\text{d}}^{*}(t)$ is plotted in Fig. 5.2(b). Please refer to Section 2.4 for more

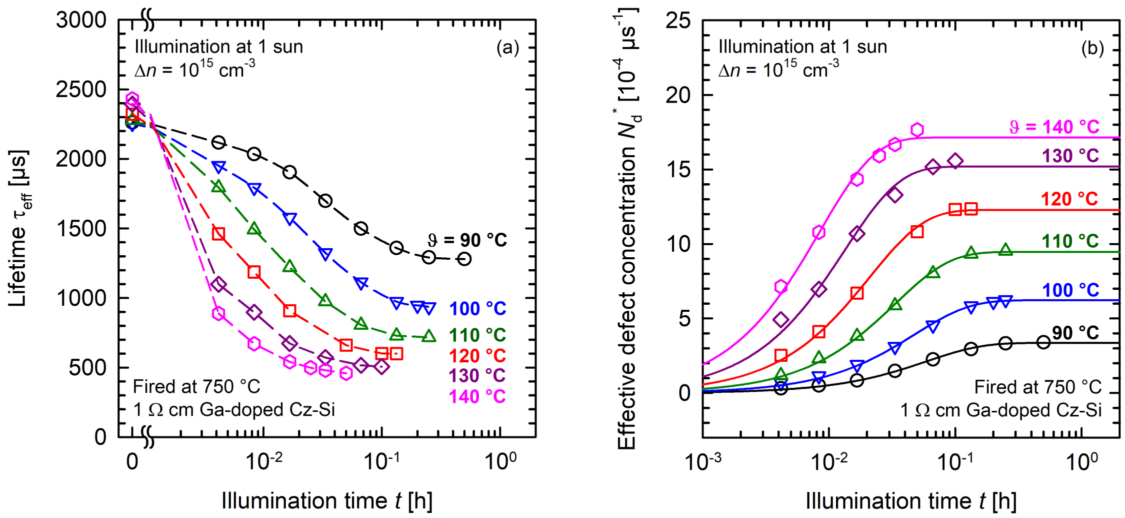

Figure 5.2: Lifetime degradation of Cz-Si:Ga illuminated at 1 sun at temperatures ϑ ranging from 90 °C to 140 °C. (a) Effective lifetime τ_{eff} at $\Delta n = 10^{15}\,\mathrm{cm}^{-3}$, as a function of illumination time t. The dashed lines serve as guide to the eye. (b) Corresponding effective defect concentration $N_{\mathrm{d}}^{*}(t)$ (colors and symbols match the graphs in (a)). The lines are exponential rise-to-maximum fits of the measurement data calculated by using Eq. (5.2).

details on the effective defect concentration. $N_{\mathrm{d}}^{*}(t)$ is determined using the definition

$$N_{\mathrm{d}}^{*}(t) = \frac{1}{\tau_{\mathrm{d}}(t)} - \frac{1}{\tau_{0}}, \tag{5.1}$$

with $\tau_{\mathrm{d}}(t)$ being the lifetime after illumination for the time t and τ_0 being the lifetime before starting the illumination. The colors and symbols used in Fig. 5.2(b) match the ones in Fig. 5.2(a). Whereas the dashed lines in Fig. 5.2(a) serve as guide to the eye, the lines in Fig. 5.2(b) are exponential rise-to-maximum fits of $N_{\mathrm{d}}^{*}(t)$:

$$N_{\mathrm{d}}^{*}(t) = N_{\mathrm{max}}^{*}\left(1 - \exp\left(-R_{\mathrm{deg}} \times t\right)\right), \tag{5.2}$$

with the maximum defect concentration N_{max}^{*} and the degradation rate constant R_{deg} as fit parameters. Note that adding a scale factor s(Δn) as introduced in Section 4.3 has only a minor impact on the apparent R_{deg}, i.e., less than 7%$_{\mathrm{rel}}$ due to significantly less lifetime degradation compared to Cz-Si:B and mc-Si:B, or more precisely negligible changes of Δn in our samples under one-sun illumination. Hence we will neglected it for degradation in Cz-Si:Ga and FZ-Si:B in this chapter.

As clearly visible in Fig. 5.2, the extent of the lifetime degradation in Cz-Si:Ga shows a pronounced dependence on the applied temperature ϑ during illumination. Whereas the degradation at 90 °C and 1 sun leads to a fully degraded state with $\tau_{\mathrm{eff,d}} = 1300\,\mu\mathrm{s}$ at $\Delta n = 10^{15}\,\mathrm{cm}^{-3}$ (initially $\tau_0 = 2300\,\mu\mathrm{s}$), $\tau_{\mathrm{eff,d}}$ is reduced to 500 µs, if the degradation is performed at 140 °C and 1 sun. As can be seen in Fig. 5.2(b), increasing ϑ from 90 °C to 140 °C increases N_{max}^{*} by a factor of 5.

The equilibrium state establishing itself between the activated and the deactivated state of the defect is dependent on ϑ and the activation and deactivation are reversible processes. This is illustrated in Fig. 5.3. A degraded lifetime sample is illuminated at a low temperature (44 °C, 0.5 suns), which completely deactivates the

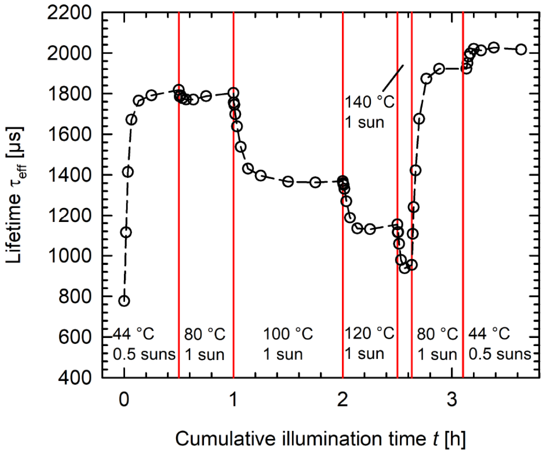

Figure 5.3: Lifetime degradation of Cz-Si:Ga versus the cumulative illumination time t. The gradual change of the applied temperature leads to different degraded states, showing the dependence of the equilibrium state between activated and deactivated defect centers on the temperature.

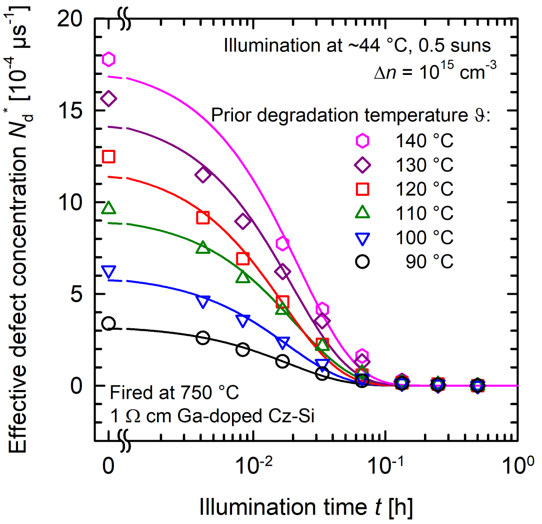

Figure 5.4: Temporary deactivation of the Cz-Si:Ga degradation effect by illumination near room temperature (i.e., 0.5 suns, ∼44 °C). Shown is the effective defect concentration $N_{\mathrm{d}}^*(t)$ (colors and symbols match the graphs in Fig. 5.2), the lines are exponential decay fits following Eq. (5.3).

defect. Afterwards, the temperature ϑ is increased step-by-step at a constant illumination intensity of 1 sun. This leads to a decreasing lifetime in step-shaped plateaus, corresponding to a successive increase in defect concentration. The subsequent reduction of ϑ to 80 °C and then 44 °C shows that the degradation is reversible. At the end of the series of experiments, almost the same lifetime of 2000 µs is attained as at the beginning. We attribute the fact that the lifetime at the end of the experiment of 2000 µs is higher than after the initial 44 °C step (1800 µs) to a partial permanent deactivation of the defect during the series of experiments (cf. Section 5.8).

As already mentioned, illumination at 0.5 suns and ∼44 °C for up to 30 min completely reverses the observed temperature-dependent LeTID effect. This is shown in Fig. 5.4 for the effective defect concentration $N_{\mathrm{d}}^*(t)$. Note that a similar behavior at low temperatures has been reported for LeTID in mc-Si solar cells [20, 91] and also in fired FZ-Si wafers [19]. We calculate $N_{\mathrm{d}}^*(t)$ for the temporary defect deactivation using Eq. (5.1) and assuming the same τ_0 as for the defect activation before. A simple exponential decay function is fitted to the data shown in Fig. 5.4:

$$N_{\mathrm{d}}^*(t) = N_{\mathrm{max}}^* \times \exp\left(-R_{\mathrm{de}} \times t\right). \tag{5.3}$$

The extracted deactivation rate constant R_{de} from the data shown in Fig. 5.4 amounts to $(52 \pm 10)\,\mathrm{h}^{-1}$ regardless of the degradation temperature ϑ applied. The temporary deactivation on Cz-Si:Ga is hence a very fast process and we no longer measure any significant change of the carrier lifetime after 30 min.

Due to the fact that the defect activation and deactivation processes are fully reversible, all measured data shown in Fig. 5.2 have been obtained from the same lifetime sample by repeating the experiment at different temperatures ϑ, starting at the lowest ϑ of 90 °C and increasing it for each repetition. After each complete degradation, the defect deactivation process shown in Fig. 5.4 has been used. In order to verify the observed behavior, the dependence of N^*_{max} on the temperature has been confirmed on various samples. Furthermore, the complete and reversible deactivation has been confirmed by repeated activation/deactivation cycles on the same samples under constant degradation conditions.

Interestingly, we observe a qualitatively similar degradation behavior on our FZ-Si:B wafers as observed on our Cz-Si:Ga samples. Figure 5.5 shows the degradation observed on the FZ-Si:B samples at temperatures ϑ ranging from 70 °C (black circles) to 120 °C (pink hexagons) at 1 sun illumination intensity. Figure 5.5(a) shows the effective lifetime τ_{eff} as a function of illumination time t. The corresponding evolution of the effective defect concentration $N^*_{\mathrm{d}}(t)$ is plotted in Fig. 5.5(b). Whereas degradation at 70 °C and 1 sun leads to a fully degraded state with $\tau_{\mathrm{eff,d}} = 4000\,\mu\mathrm{s}$ at $\Delta n = 10^{15}\,\mathrm{cm}^{-3}$ (initially $\tau_0 = 4300\,\mu\mathrm{s}$), $\tau_{\mathrm{eff,d}}$ is reduced to 3200 µs, if the degradation is performed at 100 °C and 1 sun. In contrast to the results on Cz-Si:Ga in Fig. 5.2, the maximum defect concentration N^*_{max} for FZ-Si:B in Fig. 5.5(b) reaches a maximum at $\vartheta = 100$ °C and decreases for larger ϑ. This can be attributed to the onset of the defect deactivation under prolonged illumination, resulting in parallel degradation and regeneration of the effective lifetime (see also Section 5.8). Since activation and deactivation of the defect are parallel processes, this effect leads to reduced N^*_{max} values for ϑ larger than 100 °C in the case of FZ-Si:B. We would expect the same effect for Cz-Si:Ga as well, but occurring at higher temperatures (cf. Section 5.4).

Importantly, the defect deactivation (regeneration of τ_{eff}) under prolonged illumination at elevated temperatures should not to be confused with the deactivation by illumination at low temperatures (e.g., 0.5 suns at ∼44 °C, see Figs. 5.4 and 5.6).

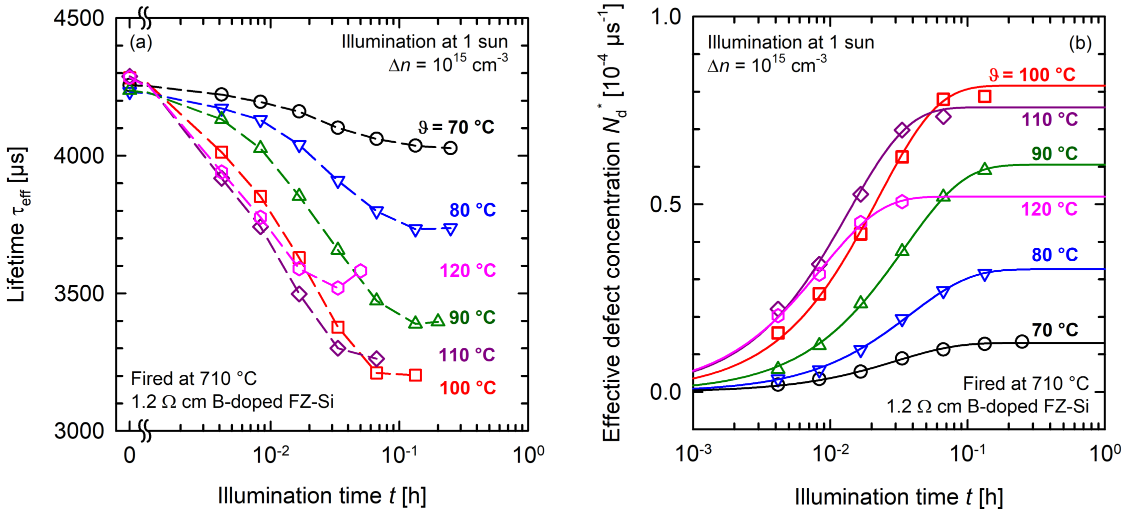

Figure 5.5: Lifetime degradation of FZ-Si:B illuminated at 1 sun at temperatures ranging from 70 °C to 120 °C. (a) Effective lifetime τ_{eff} at $\Delta n = 10^{15}\,\mathrm{cm}^{-3}$, as a function of illumination time t. The dashed lines serve as guide to the eye. (b) Corresponding effective defect concentration $N^*_{\mathrm{d}}(t)$ (colors and symbols match the graphs in (a)). The lines are exponential rise-to-maximum fits of the measurement data calculated by using Eq. (5.2).

The deactivation close to room temperature is merely a temporary (non-permanent) effect, whereas under prolonged illumination at elevated temperatures a permanent deactivation is achievable (see Section 5.8).

The temporary defect deactivation at low temperatures on FZ-Si:B is shown in Fig. 5.6. The deactivation rate constant R_{de} calculated using Eq. (5.3) amounts to $(74 \pm 9)\,\mathrm{h}^{-1}$, which is even faster than on Cz-Si:Ga ($R_{\mathrm{de}} = (52 \pm 10)\,\mathrm{h}^{-1}$).

The maximum defect concentration N^*_{max} follows a linear correlation, if plotted versus the illumination temperature ϑ at a constant illumination intensity. This is shown in Fig. 5.7 for an illumination intensity of 1 sun. Whereas in the case of Cz-Si:Ga the complete data set (ϑ between 90 °C and 140 °C) can be fitted using a linear function (Fig. 5.7, black circles), only the limited temperature range from 70 °C to 100 °C follows a linear correlation for FZ-Si:B (Fig. 5.7, red squares). This can be attributed to the afore mentioned onset of the permanent deactivation at higher temperatures ϑ. The lines in Fig. 5.7 show fits of the linear function

$$N^*_{\mathrm{max}} = a \times \vartheta + b \tag{5.4}$$

to the measured data. It is obvious from Fig. 5.7 that the slopes a differ by a factor of ~10 ($a_{\mathrm{Cz:Ga}} = (28 \pm 1) \times 10^{-6}/(^\circ\mathrm{C}\,\mu\mathrm{s})$ and $a_{\mathrm{FZ:B}} = (2.3 \pm 0.1) \times 10^{-6}/(^\circ\mathrm{C}\,\mu\mathrm{s})$) for the two materials. The temperature where no degradation should be observable at all (i.e., the intercept with the temperature axis) is determined to be $\vartheta = 78\,^\circ\mathrm{C}$ for Cz-Si:Ga and $\vartheta = 65\,^\circ\mathrm{C}$ for FZ-Si:B. Experiments at 80 °C for Cz-Si:Ga (see Fig. 5.1) revealed that a degradation is still observable, however, the maximum defect concentration is minimal ($N^*_{\mathrm{max}} < 2 \times 10^{-4}\,\mu\mathrm{s}^{-1}$).

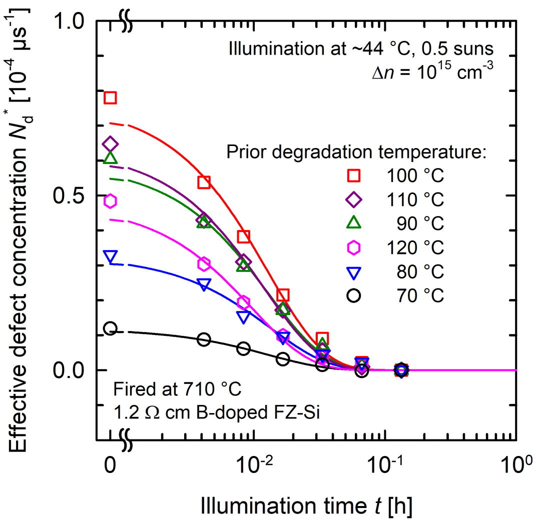

Figure 5.6: Temporary deactivation of the FZ-Si:B degradation effect by illumination near room temperature (i.e., 0.5 suns, ~44 °C). Shown is the effective defect concentration $N^*_{\mathrm{d}}(t)$ (colors and symbols match the graphs in Fig. 5.5), the lines are exponential decay fits following Eq. (5.3).

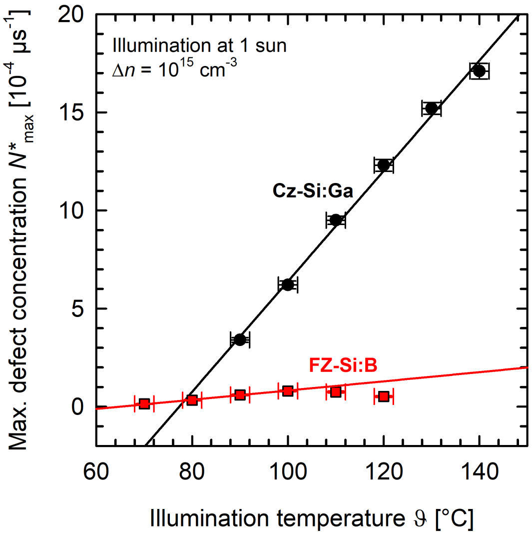

Figure 5.7: Maximum defect concentration N^*_{max} as a function of the illumination temperature ϑ for Cz-Si:Ga (black circles) and FZ-Si:B (red squares). The lines are linear fits for either the complete set of data (Cz-Si:Ga) or for the data measured in the temperature range of 70 °C to 100 °C (FZ-Si:B).

Please note that N^*_{max} in FZ-Si:B is significantly smaller than on the Cz-Si:Ga wafers (by a factor ~6 at $\vartheta = 90\,°\mathrm{C}$, as the comparison between black circles and red squares in Fig. 5.7 reveals). Whereas the actual peak temperatures in the firing furnace showed a difference of ~40 °C for the two different materials under examination (due to different optical properties, the FZ-Si:B wafers are shiny-etched), it is more likely that the significantly reduced amount of impurities in FZ-Si:B is responsible for the observed differences. However, a certain influence of the firing peak temperature cannot be excluded.

Reference measurements on non-fired samples revealed no significant degradation. In Fig. 5.8, the initial and degraded injection-dependent lifetime data of both a fired and a non-fired Cz-Si:Ga lifetime sample illuminated at $\vartheta = 100\,°\mathrm{C}$ and 1 sun are depicted. Although non-fired Cz-Si:Ga shows indeed a very slow degradation, resulting in a reduction of the lifetime from 1600 µs to 1400 µs at $\Delta n = 10^{15}\,\mathrm{cm}^{-3}$ within 4 hours (Fig. 5.8, red squares), the degradation is much less severe than for fired Cz-Si:Ga wafers under the same conditions within 15 min (Fig. 5.8, black circles). Also, no lifetime recovery at illumination near room temperature (i.e., ~44 °C and 0.5 suns) is observed afterwards for non-fired Cz-Si:Ga for 20 h. This makes it very unlikely that the observed slight degradation effect has the same physical origin as the one reported on fired Cz-Si:Ga wafers. Furthermore, the lifetime of non-fired FZ-Si:B remains completely stable at 3200 µs under the same conditions. Note that dark-anneal experiments with fired samples at the same temperature of 100 °C showed no degradation either within 1 h.

We conclude that charge carrier injection is necessary to activate the temperature-dependent degradation effect, which is triggered by the fast-firing step. The impact of the fast-firing parameters will be examined in more detail in Section 5.4.

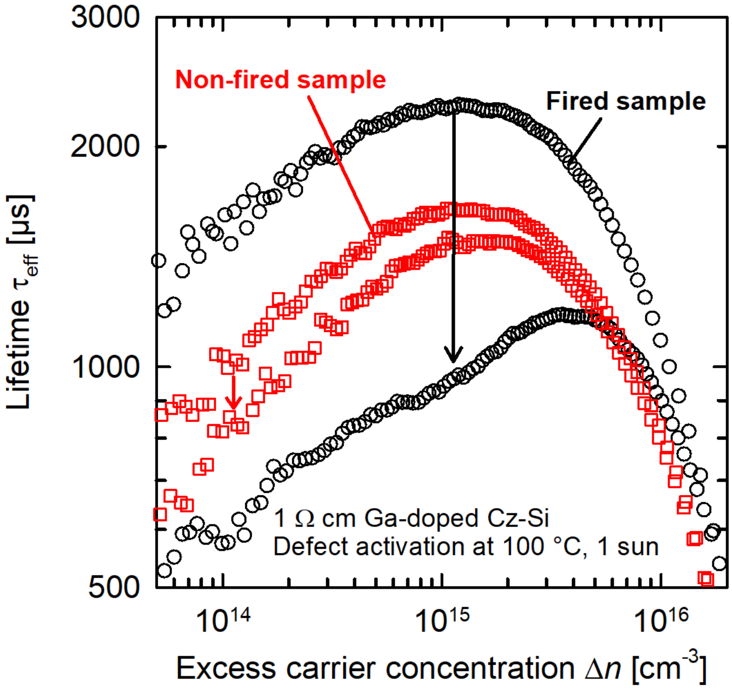

Figure 5.8: Injection-dependent lifetimes for deactivated (upper curve) and activated (lower curve) defect in Cz-Si:Ga at 100 °C and 1 sun light intensity. Shown are a fired (black circles) and a non-fired (red squares) sample.

5.4 Impact of fast-firing conditions on LeTID

In the previous section, we showed that the LeTID effect in Cz-Si:Ga is strongly temperature-dependent. The defect can be temporarily deactivated by illumination at low temperatures and a fast-firing step is necessary to trigger the degradation. In this section we examine the impact of the fast-firing step in more detail.

Several parameters have been shown to have a major impact on the extent of LeTID effects observed in different B-doped silicon materials, such as B-doped mc-Si and monocrystalline FZ-Si. The refractive index n of hydrogen-rich silicon nitride (SiN_y) layers (related to the SiN_y composition) and the peak firing temperature (FT) were shown to be related to the amount of hydrogen in-diffusion into the silicon bulk, which is believed to be one major cause of LeTID [19, 88, 99, 100]. In addition, the cooling ramp of the applied firing step after FT was demonstrated to have a significant impact on the extent of LeTID in B-doped silicon materials [101, 102]. A typical firing profile measured on the wafer surface is shown exemplarily in Fig. 5.9. In this section, we perform a series of degradation experiments to examine the impact of the peak firing temperature FT and the band velocity v_{band} (related to the cooling ramp after FT) of the conveyor belt furnace on the extent of lifetime degradation in Cz-Si:Ga. In addition, we vary the properties of the hydrogen-rich silicon nitride (SiN_y:H) deposited on top of an aluminum oxide (AlO_x) passivation layer both on Cz-Si:Ga and FZ-Si:B wafers at fixed FT and v_{band}. In order to vary the hydrogen content diffusing into the silicon wafer during firing, we increase the silicon

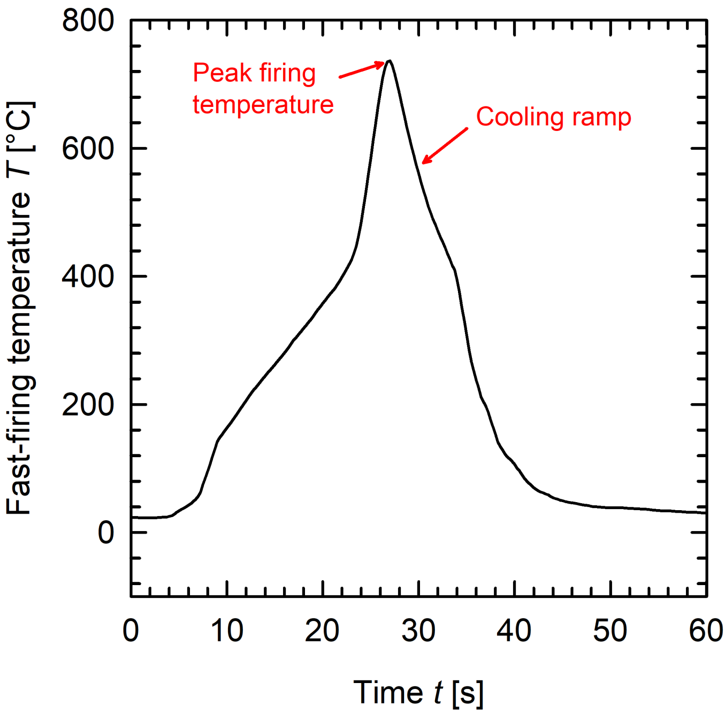

Figure 5.9: Typical firing profile measured on the wafer surface of a 1 Ω cm Cz-Si:Ga wafer (W = 150 µm) at a set-peak firing temperature of 850 °C and a band velocity v_{band} of 6.8 m/min. While the peak firing temperature FT denotes the highest measured temperature T during fast-firing, the cooling ramp is mostly defined by the decrease in T after FT.

Table 5.1: Summary of parameter variations.

Parameter	FT	v_{band}	SiN_y (n)
Peak temperature [°C]	630-800	740	750
Band velocity [m/min]	6.8	2.8-7.2	6.8
Refractive index n	2.05	2.05	2.07/2.24/2.37

content and thereby decrease the atomic density of the SiN_y films by increasing the silane gas flow during the PECVD process, which increases the refractive index n of the SiN_y layers. It has been shown that the atomic density of the silicon nitride film has a pronounced impact on the in-diffusion of hydrogen into the silicon bulk of multicrystalline silicon [88].

The firing conditions applied for the three variations are summarized in Table 5.1. In order to quantify the impact of the key parameters FT, v_{band}, and n of the SiN_y layers, the maximum defect concentration N^*_{max} as introduced in Eq. (5.2) is examined as a function of the temperature ϑ during illumination at 1 sun.

Figure 5.10 shows the impact of the peak firing temperature FT and the band velocity v_{band} of the fast-firing step on the LeTID effect described in Section 5.3. In Fig. 5.10(a), the maximum defect concentration N^*_{max} calculated using Eq. (5.2) is plotted versus the temperature during illumination ϑ for the three FT values of 680, 740, and 800 °C. N^*_{max} depends linearly on ϑ between 100 °C and 140 °C. The lines are simple linear fits to the measurement data within the respective applicable temperature range following Eq. (5.4).

Please note that we observe no LeTID after firing at the lowest applied FT value of 630 °C, which we take into account with a grey zero line in Fig. 5.10(a). As a reference, we added also the linear correlation (cyan dashed line) for N^*_{max} which was

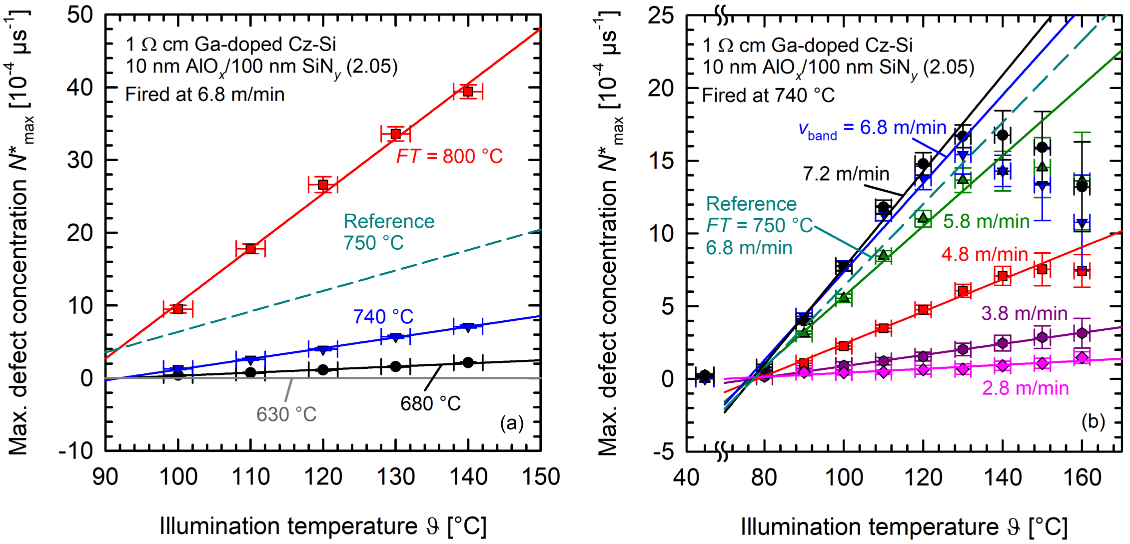

Figure 5.10: Maximum effective LeTID defect concentration N^*_{max} as a function of the temperature ϑ during illumination for variations of (a) the peak firing temperature FT and (b) the band velocity v_{band} of the fast-firing step. The lines are linear fits to the data within the respective applicable temperature ranges.

discussed in detail in Section 5.3 and determined on a different batch of samples. That batch had been fired at an FT value of 750 °C.

Figure 5.10(b) shows $N^*_{\text{max}}(\vartheta)$ for six different band velocities v_{band} ranging between 2.8 and 7.2 m/min at a fixed FT value of 740 °C. Again, the reference of Section 5.3 on the same Cz-Si:Ga material after firing at 750 °C and 6.8 m/min is plotted as a cyan dashed line. There are in part significant deviations from the linear correlation between N^*_{max} and ϑ for higher ϑ and v_{band} values. Whereas for the higher v_{band} values above ∼5 m/min the temperature dependence of LeTID follows a linear correlation only at temperatures ϑ below ∼130 °C, for the lower v_{band} values below ∼4 m/min N^*_{max} increases linearly with ϑ over the entire examined temperature ranges between 80 °C and 160 °C. We attribute the deviations from the linear correlation to the onset of defect deactivation under prolonged illumination, which we will discuss in more detail in Section 5.8.

Whereas for ϑ between 80 °C and 160 °C the illumination intensity was set at 1 sun, the same was reduced to 0.5 suns to reach $\vartheta = 44\,°\text{C}$ in Fig. 5.10(b), which is the equilibrium temperature at this intensity. Please note that reducing the illumination intensity to 0.5 suns has no impact on the observed N^*_{max} values, as will be shown in Section 5.7. Note furthermore that the temperature axis in Fig. 5.10(b) has a break for better clarity and omits the temperatures from 47 to 70 °C. The degradation from initially ∼2300 µs to ∼2200 µs observed at 44 °C and 0.5 suns within ∼10 h deviates strongly from the linear correlation for $N^*_{\text{max}}(\vartheta)$ observed above 80 °C. Furthermore, degradation at 44 °C shows no correlation with v_{band}. From this observation we conjecture that a different mechanism might be present at 44 °C, which is not related to the LeTID defect.

For this study and Cz-Si:Ga samples with maximum lifetimes at or below ∼2500 µs, 77 °C is the lower limit for the observation of LeTID, as determined by the intercept of the linear fits with the temperature axis in Fig. 5.10(b).

The reference cyan dashed line fits relatively well into the data shown in Fig. 5.10, although some deviations regarding the absolute value of N^*_{max} in Fig. 5.10(a), are to be noted. Furthermore, the blue inverse triangles in the Figs. 5.10(a) and 5.10(b) represent an a priori identical fast-firing step, but also show non-negligible differences regarding the absolute values of N^*_{max}. However, although from the same material, the samples stem from different processed batches, which makes it difficult to draw definite conclusions.

It can be concluded for Fig. 5.10 that the extent of LeTID in Cz-Si:Ga depends critically on both FT and v_{band}, which we attribute to the content of available hydrogen within the silicon bulk. Increasing FT increases the in-diffusion of hydrogen into the silicon bulk from the SiN_y:H layers on the wafer surfaces [66, 90]. Helmich et al. showed in Ref. [90] that AlO_x layers serve as a diffusion barrier for hydrogen. However, the AlO_x layer is essential to provide excellent surface passivation for our wafers, resulting in measured effective lifetimes of up to 2500 µs after firing. For an AlO_x thickness of 10 nm, however, hydrogen is still detectable in both FZ-Si:B and Cz-Si:B after firing at an FT of 765 °C [103]. Since we do not vary the AlO_x thickness during our lifetime experiments, we do not expect an impact of the barrier function on our experiments.

The dependence of N^*_{max} on v_{band} is likely due to the different cooling ramps after the peak firing temperature FT. Figure 5.11 shows the N^*_{max} dependence on the

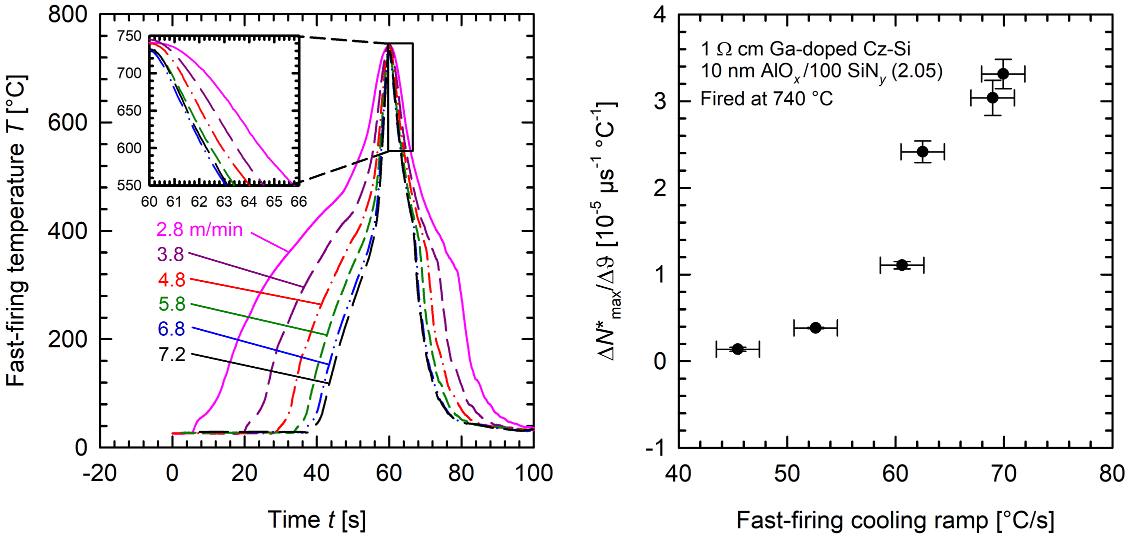

Figure 5.11: Dependence of the maximum effective LeTID defect concentration N^*_max on the cooling ramp of the fast-firing step. (a) Firing profile measured on the wafer surfaces of $1\,\Omega\,\text{cm}$ Cz-Si:Ga wafers ($W = 150\,\mu\text{m}$) at different band velocities v_band between $2.8\,\text{m/min}$ and $7.2\,\text{m/min}$ and a measured peak firing temperature FT of $\sim$740 °C. The inset shows a magnification of the cooling ramps after FT. (b) Gradient of the linear fits shown in Fig. 5.10(b) $\Delta N^*_\text{max}/\Delta\vartheta$ versus the cooling ramp of the fast-firing step shown in (a).

cooling ramp for the data depicted in Fig. 5.10(b). In Figure 5.11(a), the firing profiles measured on the examined wafers are depicted. The inset shows the cooling ramp after FT. The cooling ramp used in Fig. 5.11(b) is given by the gradient of the fast-firing temperature $\Delta T/\Delta t$ between 700 °C and 600 °C (cf. Fig. 5.11(a)). Both diffusivity and solubility of hydrogen are known to decrease with decreasing temperature [104, 105], significantly increasing the impact of the higher temperatures $>$600 °C on the diffusion length of hydrogen in silicon [106, 107]. Figure 5.11(b) shows the gradient of the linear fits depicted in Fig. 5.10(b) $\Delta N^*_\text{max}/\Delta\vartheta$ versus the cooling ramp. The gradient $\Delta N^*_\text{max}/\Delta\vartheta$ has an apparent s-shape and increases significantly for cooling ramps between 50 °C/s and 70 °C/s. The hypothesis is that a slower cooling ramp results in more hydrogen diffusion to hydrogen sinks, from which it is no longer available for defect formation under illumination. At faster cooling ramps, however, both diffusivity and solubility in silicon decrease very fast after FT, quenching the hydrogen within the bulk [101, 102]. We chose the gradient $\Delta N^*_\text{max}/\Delta\vartheta$ to represent the LeTID extent in Fig. 5.11(b). Note, however, that using the N^*_max values at a fixed temperature ϑ during illumination would result in a similar s-shape with increasing cooling ramps. Our results are in agreement with the literature regarding the impact of the cooling ramp on LeTID in mc-Si [101, 102] and FZ-Si [108].

Figure 5.12 shows the impact of the composition (related to the refractive index n) of the SiN$_y$:H layer on the extent of LeTID. Whereas Fig. 5.12(a) shows N^*_max as a function of the temperature ϑ during illumination for three different refractive indices n of the hydrogen-rich SiN$_y$:H on Cz-Si:Ga, Fig. 5.12(b) shows the impact of the SiN$_y$:H composition for FZ-Si:B at lower temperatures than for Cz-Si:Ga. We decided to use lower temperatures – and as a consequence also a reduced illumina-

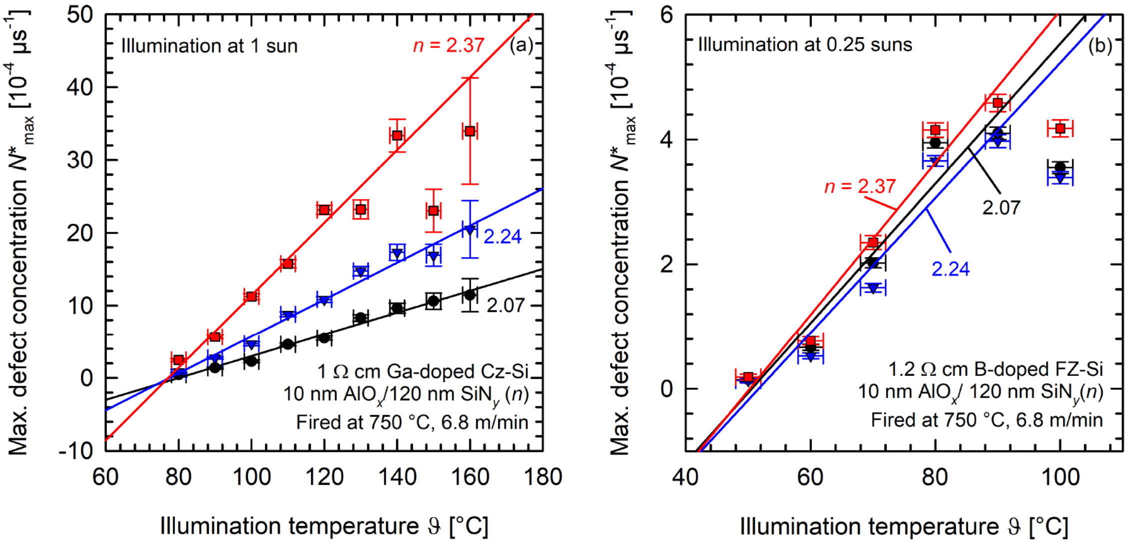

Figure 5.12: Maximum effective LeTID defect concentration N^*_{max} as a function of the temperature ϑ during illumination for variations of the refractive index n of hydrogen-rich SiN$_y$:H layers deposited on both wafer surfaces for (a) Cz-Si:Ga and (b) FZ-Si:B after firing at a peak temperature of 750 °C. The lines are linear fits to the measured data within the respective applicable temperature ranges.

tion intensity of 0.25 suns – because of the significantly lower maximum of $N^*_{\mathrm{max}}(\vartheta)$ for FZ-Si:B, which peaks already at 90 °C (see Fig. 5.12(b)). Halogen lamp illumination at 1 sun itself would cause a temperature of 70 °C on the wafer surface, whereas illumination at 0.25 suns leads to only 35 °C.

Both the absolute N^*_{max} for each applied ϑ and the slope of the linear fits of $N^*_{\mathrm{max}}(\vartheta)$ increase for Cz-Si:Ga (Fig. 5.12(a)) with increasing n. These results are in agreement with the assumption that hydrogen is an essential part of the LeTID defect. The hydrogen content in the silicon bulk has been shown to increase over the examined range of the refractive index after fast-firing treatment [88]. However, we do not observe the same kind of increasing behavior with increasing n for FZ-Si:B in Fig. 5.12(b). This difference to the otherwise similar degradation behavior in Cz-Si:Ga indicates a second participant in the defect reaction besides hydrogen, which limits N^*_{max} in FZ-Si:B. Float-zone silicon has in general a significantly reduced amount of impurities compared to Cz-Si. This includes non-metallic impurities such as oxygen as well as metallic impurities such as 3d transition metals. We will discuss the dependence of the hydrogen content on the composition of the SiN$_y$:H layer in Section 5.5.

In order to determine the uncertainty for the maximum defect concentrations N^*_{max} in Figs. 5.10 and 5.12, we generate and fit 10,000 ensembles of random deviations from the lifetime data measured on single samples using a normal distribution. We assume a standard deviation (1σ) of 2% for the original lifetime measurements as exemplarily shown in Fig. 5.2(a). Thereby, each lifetime measurement already represents an averaged value over five measurements using the WCT-120 built-in averaging. This assumption is in agreement with the general uncertainty of the lifetime measurement using PCD measurements as reported by McIntosh and Sinton [109]. Furthermore, a standard deviation for each illumination interval of 2 s is used to determine $\Delta N^*_{\mathrm{max}}$. We assume ±2 °C for the temperature in Figs. 5.10 and 5.12.

5.5 Impact of compositional variations of SiN$_y$:H on the hydrogen content within the silicon bulk

In the previous section, we have shown that the extent of LeTID in Cz-Si:Ga depends critically on the peak firing temperature FT and the band velocity v_{band} of the fast-firing step. Furthermore, the composition of hydrogen-rich SiN$_y$:H layers has a significant impact on the extent of LeTID as well. All three influencing factors are in agreement with an increasing amount of hydrogen available for defect reactions within the silicon bulk. In this section, we will look at the connection between hydrogen in the silicon bulk and the composition of SiN$_y$:H layers on both Cz-Si:Ga and, as a reference, on FZ-Si:B.

Hydrogen from hydrogen-rich SiN$_y$:H layers diffuses during the fast-firing step into the silicon bulk, where it can interact with defects and sometimes passivates deep-level impurities [103, 110, 111]. However, hydrogen is also believed to play an important role in the LeTID defect reaction mechanism observed in mc-Si:B, FZ-Si:B, and possibly even on P-doped n-type silicon [19, 88, 99–101, 112]. After firing, the hydrogen within the silicon bulk mainly consists of hydrogen dimers H_2 [113], which dissociate during annealing (e.g., at 160 °C) and can then passivate dopant atoms (in B-doped Si) [114]. To measure the resulting resistivity changes of silicon samples, Walter et al. [115] proposed a method using the eddy-current technique employed within the WCT-120 lifetime tester from Sinton Instruments. Although the chuck of the setup is temperature controlled, the sample temperature for each measurement has to be recorded and the resistivity is extrapolated to a fixed temperature of 25 °C. The saturation value of the resistivity change is a measure of the hydrogen content within the silicon bulk. For boron-doped silicon a detailed defect model exists [113], which allows to determine the total hydrogen concentration from the base resistivity of the wafer and its change upon annealing. According to the model, in case of boron-only doping, this change is caused by the formation of hydrogen-boron pairs (HB pairs) [115]. Several studies have shown this consistently on FZ-Si:B [88, 90, 115, 116] and Cz-Si:B [103]. Experiments conducted on Cz-Si:Ga showed qualitatively comparable, but quantitatively smaller changes in resistivity during annealing compared to FZ-Si:B [117, 118].

In this section, we present measurements of the resistivity changes upon annealing at temperatures $\geq$160 °C on both FZ-Si:B and Cz-Si:Ga samples coated with SiN$_y$:H layers of different compositions, i.e., with refractive indices n of 2.07, 2.24, and 2.37. The samples were processed in parallel to the lifetime samples with the variation of n presented in Section 5.4, but without an AlO$_x$ passivation layer underneath the SiN$_y$:H layers.

Figure 5.13 shows the changes in the specific resistivities $\Delta\rho$ versus the annealing time t of FZ-Si:B samples for three refractive indices n of the SiN$_y$ layers of 2.07, 2.24, and 2.37 after fast-firing at 750 °C and 6.8 m/min. A non-fired sample with $n = 2.37$ is shown as a reference (green diamonds). Whereas the non-fired sample shows no increase of $\Delta\rho$ for 2000 h of annealing, the resistivities of the fired samples saturate within 100 to 200 h at 160 °C due to the formation of HB pairs. Furthermore, the extent of $\Delta\rho$ increases with increasing n, which directly correlates to the hydrogen content available for HB formation within the silicon bulk. Afterwards, under prolonged annealing at the slightly higher temperatures of 180 °C (for 100 h)

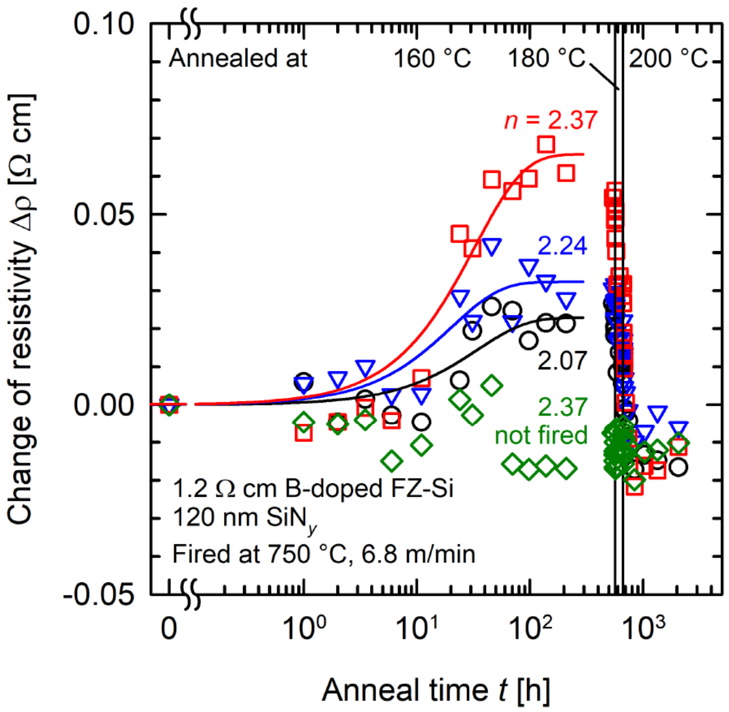

Figure 5.13: Measured changes of the specific resistivity Δρ of FZ-Si:B samples fired under the same conditions (750 °C, 6.8 m/min) as a function of time during dark annealing at 160 °C (for 565 h), 180 °C (for the next 100 h after annealing at 160 °C), and 200 °C (for the last 1400 h). SiN$_y$:H films of three different refractive indices n (2.07, 2.24, 2.37) were deposited prior to firing. One non-fired sample is not showing any relevant change in Δρ.

and 200 °C (for 1400 h), Δρ decreases drastically, which is attributed to a dissociation of the HB pairs [113, 114, 119].

Figure 5.14 shows the measured Δρ change for Cz-Si:Ga under prolonged annealing at 200 °C (Fig. 5.14(a)) and subsequently at 250 °C (Fig. 5.14(b)). Please note that a higher temperature was required for the Cz-Si:Ga compared to the FZ-Si:B material in order to observe a sufficiently large change in Δρ (dark annealing experiments at 160 °C and 180 °C did not lead to sufficiently large changes within the Δρ measurement uncertainty). Nonetheless, small changes at annealing temperature of 160 °C and 180 °C were observed, which is reflected in the non-zero starting values in Fig. 5.14(a). At 200 °C dark annealing temperature, however, a significant increase of Δρ occurs, as can be seen in Fig. 5.14(a). The lines in Fig. 5.14(a) are exponential rise-to-maximum fits of the available data, where the saturation value, however, cannot be precisely extracted, because due to time restrictions we had to stop our annealing experiment after 3000 h. Importantly, the non-fired reference (green diamonds, Fig. 5.14(a)) shows no increase in Δρ.

Please note that the formation of HGa pairs in the fired samples is only one possible explanation for the increase in resistivity. In the literature, there are also reports of a hydrogen-enhanced thermal donor formation in oxygen-rich Cz-Si [120–123] which could also explain why the non-fired sample shows no increase in Δρ. In particular, Stein et al. [122] reported an activation energy of (1.5 ± 0.2) eV, determined in a temperature interval between 350 °C and 400 °C, and a thermal donor formation rate of up to $2 \times 10^{16}\,\mathrm{cm}^{-3}\,\mathrm{h}^{-1}$. An extrapolation of this formation rate to 200 °C

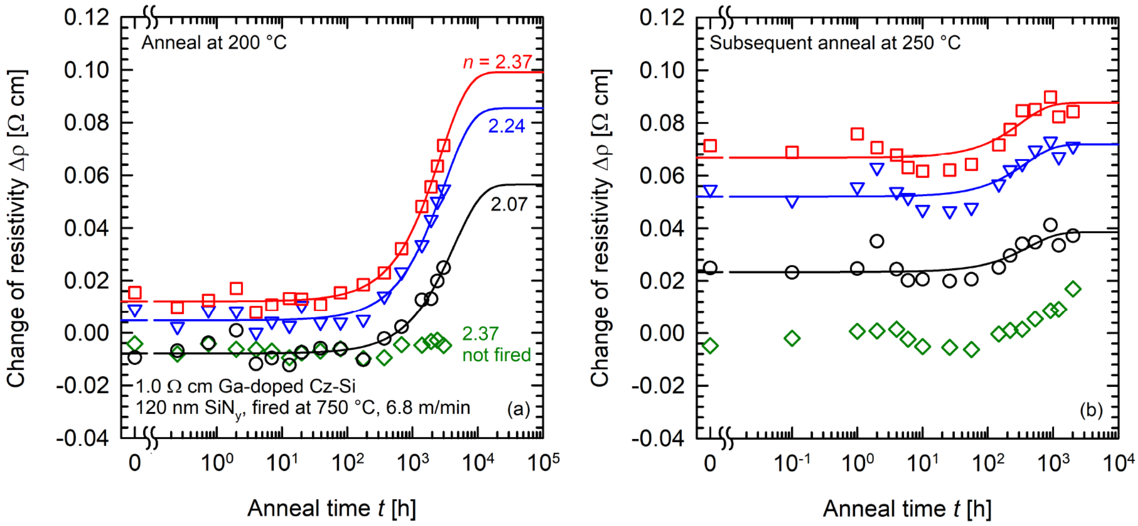

Figure 5.14: Resistivity change $\Delta\rho$ versus the anneal time t at (a) 200 °C and subsequently at (b) 250 °C for variations of the refractive index n of the SiN$_y$:H layers for Cz-Si:Ga samples, which were fired at 750 °C. The solid lines are exponential rise-to-maximum fits. Note that the measurements in (a) start at non-zero values because before annealing the samples at 200 °C, annealing at 160 °C (565 h) and 180 °C (100 h) did not lead to sufficiently large changes in $\Delta\rho$.

yields a rate of $4 \times 10^{11}\,\mathrm{cm}^{-3}\,\mathrm{h}^{-1}$, which is of the same order of magnitude as the formation rates of the fits in Fig. 5.14(a). However, it is questionable if the applied extrapolation of the literature data is allowed over such a large temperature range. Furthermore, the uncertainty of such an extrapolation is at least one order of magnitude. The formation of thermal donors in the literature was typically examined at temperatures around 400 °C, which is why it is difficult to compare it directly with our experiments. Nevertheless, we can conclude that the observed resistivity changes are caused by the fast-firing step and it is likely that they are caused by hydrogen diffusion into the silicon bulk.

Due to an obvious time limitation of the experiment, 200 °C are not suitable to assess the saturation value of the observed $\Delta\rho$ increase. Therefore, the temperature was increased subsequently to 250 °C for 2000 h, as shown in Fig. 5.14(b). The solid lines are again exponential rise-to-maximum fits. At 250 °C, however, the additional increase of $\Delta\rho$ observed for the fired samples is mirrored by the non-fired sample (green diamonds, Fig. 5.14(b)), which makes the involvement of hydrogen unlikely. Thermal donors could be the cause of this continued increase, although the temperature is rather low for the formation of the same [124, 125].

Nevertheless, the increase in $\Delta\rho$ in Fig. 5.14(a) suggests an increasing hydrogen content with increasing refractive index n of the SiN$_y$:H layers, in agreement with our experiments on FZ-Si:B (Fig. 5.13). However, the $\Delta\rho$ increase for Cz-Si:Ga shown in Fig. 5.14(a) is two orders of magnitude slower compared to the $\Delta\rho$ increase observed on FZ-Si:B (Fig. 5.13). To our knowledge, resistivity changes upon dark-annealing were not reported before over such a long period of time.

Please note that we compare not only a change of the doping element (boron versus gallium) but also the silicon material (FZ-Si versus Cz-Si). Helmich et al. [103] did a comparative study on FZ-Si:B and Cz-Si:B and observed no significant dependence of the HB pair formation rate on the kind of silicon material. Furthermore, Acker et al. [117] did a comparative study on FZ-Si:B and Cz-Si:Ga as well and observed an even faster increase in resistivity for Cz-Si:Ga (10 h at 160 °C) than for FZ-Si:B (100 h at 160 °C). This relatively fast increase of the resistivity in Cz-Si:Ga was also reported by Simon et al. [118] at the slightly different conditions of 180 °C (~1 h). Note that within the same timescale, we only observed fluctuations in the resistivity change (not shown here). These fluctuations, however, did result in the non-zero starting values in Fig. 5.14(a). Both mentioned studies [117, 118] did not continue their respective experiments for thousands of hours to observe differences on very large timescales.

In conclusion, the observed increase in $\Delta\rho$ during dark annealing (see Fig. 5.14(a)) in combination with the increasing extent of LeTID observed on fired Cz-Si:Ga samples with increasing refractive index n of the SiN_y films present during firing (see Fig. 5.12(a)) clearly suggest an involvement of hydrogen in the observed LeTID defect mechanism in Cz-Si:Ga.

5.6 Activation energies of LeTID mechanisms

An experimentally extracted activation energy E_A of a defect reaction typically reflects an apparent activation energy. Measurements at different temperatures usually represent a superposition of different defect reactions at different temperatures. In particular, as mentioned in Section 5.3, activation and deactivation of the responsible defect are parallel processes, which influence not only the extent of degradation at higher temperatures but have an impact on the apparent degradation rate constant R_deg as well. In order to determine the apparent activation energy E_A of the LeTID effect in Cz-Si:Ga, we measure the degradation rate constant R_deg as a function of absolute temperature T and fit the Arrhenius law

$$R_\mathrm{deg} = k_0 \times \exp\left(-\frac{E_\mathrm{A}}{k_\mathrm{B}T}\right) \tag{5.5}$$

to the measured data, k_B being the Boltzmann constant and k_0 a presumably temperature-independent pre-factor.

Figure 5.15 shows the Arrhenius plot for the comparative measurements of LeTID in Cz-Si:Ga and FZ-Si:B as discussed in detail in Section 5.3. We plot R_deg versus the inverse absolute temperature $1/T$. The temperatures ϑ in °C are depicted at the top for easy reference. Note that R_deg saturates for FZ-Si:B below 90 °C, hence we excluded the low temperature data from the fit. The deviations from the Arrhenius law of the Cz-Si:Ga samples are minimal, which is why we use the complete data set in the temperature range from 90 °C to 140 °C. We will discuss this behavior later within this section.

We obtain activation energies of $E_\mathrm{A,Cz:Ga} = (0.58 \pm 0.04)\,\mathrm{eV}$ and $E_\mathrm{A,FZ:B} = (0.57 \pm 0.02)\,\mathrm{eV}$. These values are identical within the respective measurement uncertainty ranges. However, the temperature-independent pre-factor k_0 differs by a factor of almost 2: $k_\mathrm{0,Cz:Ga} = (1.37 \pm 0.07) \times 10^9\,\mathrm{h}^{-1}$ for Cz-Si:Ga and $k_\mathrm{0,FZ:B} = (2.09 \pm 0.07) \times 10^9\,\mathrm{h}^{-1}$ for FZ-Si:B. The difference in k_0 and therefore the much faster degradation observed in FZ-Si:B compared to Cz-Si:Ga can probably be ex-

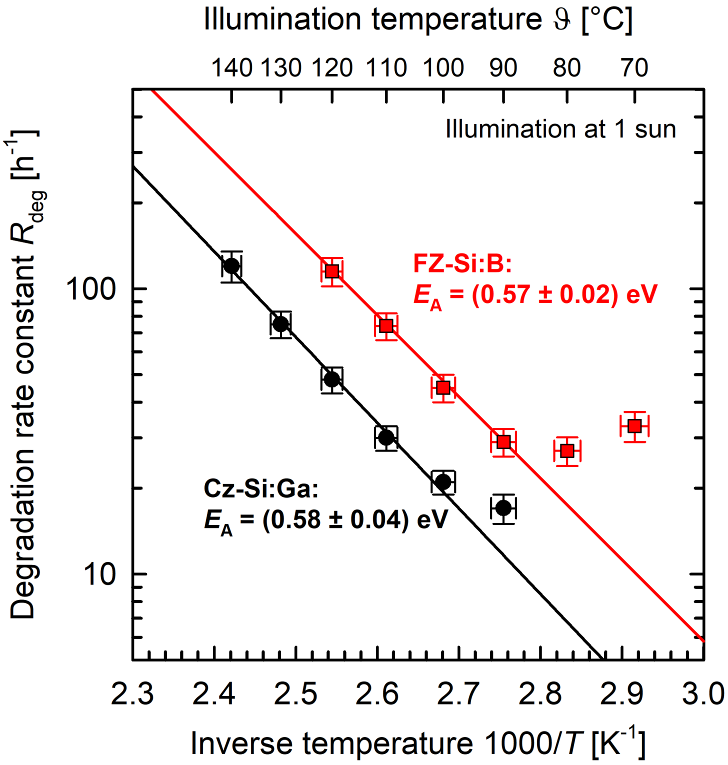

Figure 5.15: Arrhenius plot of the degradation rate constants R_{deg} over the inverse temperature $1/T$ for Cz-Si:Ga (black circles) and FZ-Si:B (red squares). The lines are Arrhenius fits following Eq. (5.5) of the complete set of temperatures ϑ ranging from 90 °C to 140 °C for Cz-Si:Ga and a limited set of ϑ ranging from 90 °C to 120 °C for FZ-Si:B.

plained by the higher carrier lifetime in FZ-Si in general due to a significantly reduced amount of impurities present. The higher lifetime results in a higher excess carrier concentration Δn under the same illumination conditions (i.e., 1 sun) and hence a higher formation rate of the responsible defect. The dependence on the illumination intensity I_{ill} will be discussed in Section 5.7.

Figure 5.16 shows the activation energy E_{A} for the variation of the refractive index n, as discussed in Section 5.4. Figure 5.16(a) shows the Arrhenius plots exemplarily for Cz-Si:Ga. For temperatures ϑ during illumination below ~100 °C, a saturation of the degradation rate constant R_{deg} is observed, the low temperature data is hence excluded from the fit. In Fig. 5.15, this saturation was only apparent for FZ-Si:B, but we observe it in both materials Cz-Si:Ga and FZ-Si:B. There hence seems to be a physical mechanism behind it, which we have not identified so far. We measure the lifetime after few and fixed time intervals between illumination periods, leading to a high sensitivity to individually measured values especially for the low temperatures, where the magnitude of degradation is relatively small. This is also reflected in the measurement uncertainty of R_{deg}, which is particularly large at 80 °C in Fig. 5.16(a).

Figure 5.16(b) shows the extracted apparent activation energies E_{A} for both Cz-Si:Ga (closed pink diamonds) and FZ-Si:B (closed green triangles) samples versus the refractive index n of the SiN$_y$ layers. The activation energies of samples from a different batch determined in Fig. 5.15 are added for reference as open symbols.

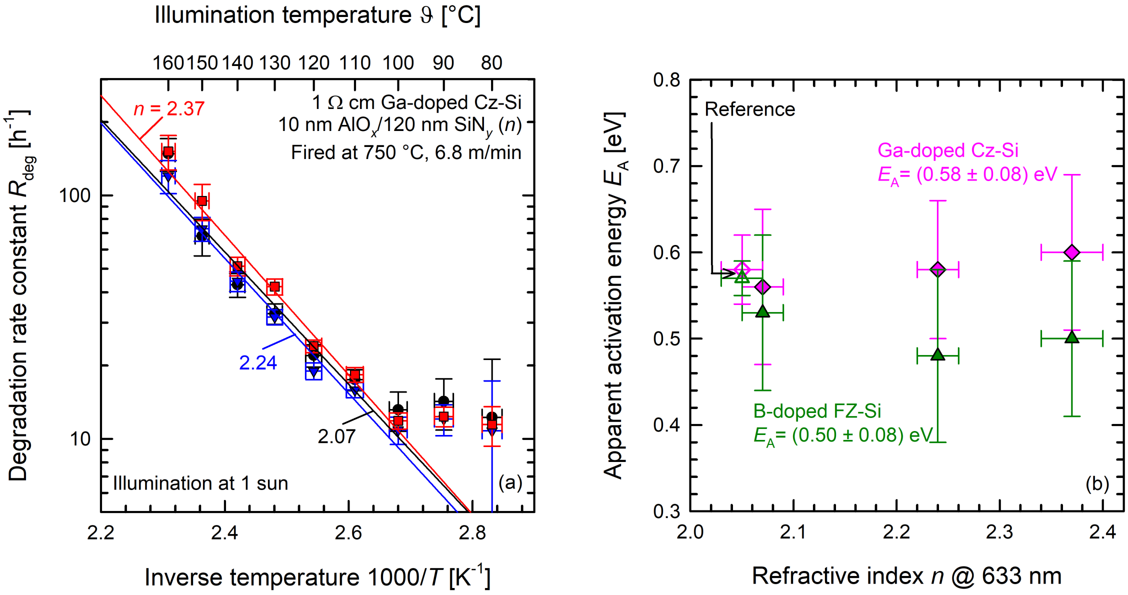

Figure 5.16: Apparent activation energies E_A for a variation of the refractive index n of SiN$_y$ layers. (a) Arrhenius plot of the degradation rate constants over the inverse temperature $1/T$ for Cz-Si:Ga. (b) Apparent activation energy E_A versus refractive index n for both Cz-Si:Ga (pink diamonds) and FZ-Si:B (green triangles).

The average value of E_A over varying n is (0.58 ± 0.08) eV for the Cz-Si:Ga and (0.50 ± 0.08) eV for FZ-Si:B wafers. Hence, E_A is constant within the relatively large E_A measurement uncertainty.

Figure 5.17 shows the extracted apparent activation energy E_A versus the peak firing temperature FT (Fig. 5.17(a)) and the band velocity v_band (Fig. 5.17(b)) of the fast-firing step. There might be a weak increase of E_A with increasing FT and v_band. This apparent increase is, however, well within the uncertainty range of the data points. The determined uncertainties are, especially for the high FT and v_band values, close to 0.1 eV. All determined E_A values shown in Figs. 5.16(b) and 5.17 lie hence within the range of (0.55 ± 0.10) eV. Our results suggest that a single defect mechanism is responsible for the LeTID effect examined in both materials, Cz-Si:Ga and FZ-Si:B.

Our experimentally determined E_A values are at the lower end of reported activation energies for LeTID effects on different silicon materials in the literature. On multicrystalline silicon, Bredemeier et al. [74] reported $E_\mathrm{A} = (0.94 \pm 0.06)$ eV, whereas Vargas et al. [126] reported $E_\mathrm{A} = (1.08 \pm 0.05)$ eV. Graf et al. [67] reported $E_\mathrm{A} = (0.80 \pm 0.12)$ eV for FZ-Si:B. Jafari et al. [127] and Lin et al. [128] reported values of $E_\mathrm{A} = (0.74 \pm 0.10)$ eV and $E_\mathrm{A} = (0.90 \pm 0.05)$ eV, respectively, on Cz-Si:Ga materials. It has to be noted that both studies on Cz-Si:Ga do not report a pronounced temperature dependence of the LeTID extent. The reason for these apparent contradictions is not clarified so far, but might be related to differences in the sample preparation or in the purity levels of the Cz-Si:Ga materials investigated in the different studies.

The uncertainties of R_deg exemplarily shown in Fig. 5.16(a) were determined in the same way as described for the maximum defect concentration N^*_max in Section 5.4 with an ensemble of random variations of the original lifetime measurements us-

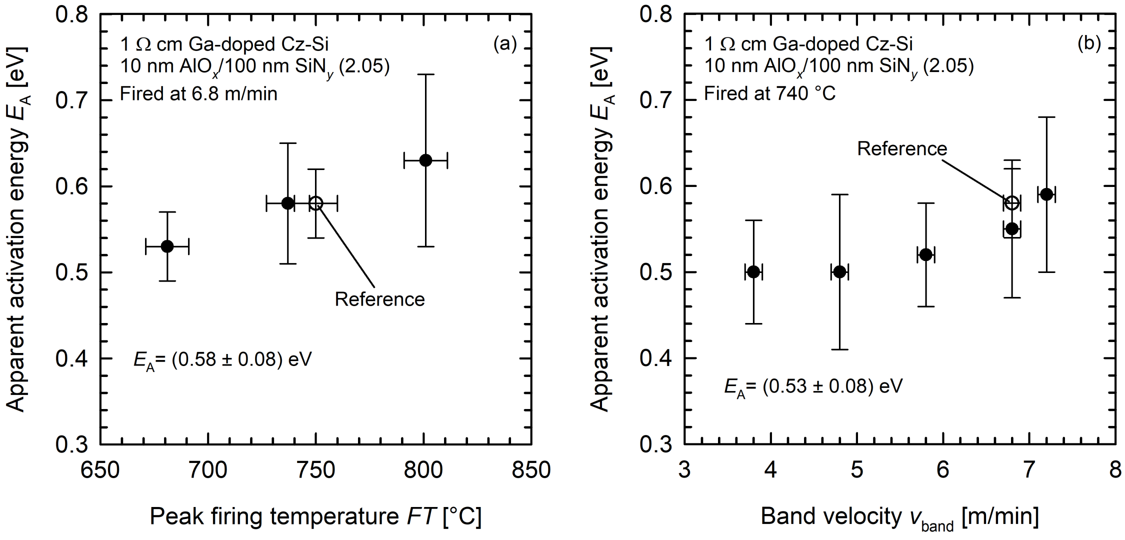

Figure 5.17: Apparent activation energies E_A versus parameter variation within the lifetime sample processing of Cz-Si:Ga. (a) Apparent activation energy E_A versus peak firing temperature FT and (b) E_A versus band velocity v_{band} of the fast-firing step.

ing a normal distribution. We calculate the uncertainty ranges for the apparent activation energy E_A following the publication by Reed [129] taking into account the uncertainty for both R_{deg} and the temperature T (i.e., 2 K). Using this "linear least-square fits with errors in both coordinates" by Reed to determine uncertainties for the exponential Arrhenius law already includes an important assumption. Since the data has to be linearized to apply the procedure published in Ref. [129], the data is weighted in a least-square-fit routine with the logarithm base e giving the lower temperatures ϑ a higher weight than the higher temperatures. In general, this assumption is valid because with increasing temperature the LeTID effect is accelerating, leading to less data points in the lifetime degradation with increasing temperature (cf. Fig. 5.2) and therefore a larger uncertainty. Furthermore, as already mentioned in Section 5.3, the deactivation under prolonged illumination is a parallel process, which is of major importance especially at higher temperatures.

We combine the logarithmic weighting of our R_{deg} data to use a linear least-square fit with two additional least-square fits of the exponential Arrhenius law in Eq. (5.5). First, under simple exclusion of the highest temperature data at 160 °C (where deactivation already takes place) and, second, under weighting the data with their standard deviations. Following this procedure, we determine the mean values and uncertainties for E_A in Figs 5.16(b) and 5.17. This is the reason why we name our E_A value apparent activation energy.

5.7 Illumination intensity dependence of LeTID

In this section, we examine the impact of the illumination intensity I_{ill} on the degradation dynamics at a fixed degradation temperature of 100 °C, while I_{ill} is varied between 0.1 and 1 sun. Figure 5.18 shows both the maximum defect concentrations N^*_{max} (Fig. 5.18(a)) and the degradation rate constants R_{deg} (Fig. 5.18(b)).

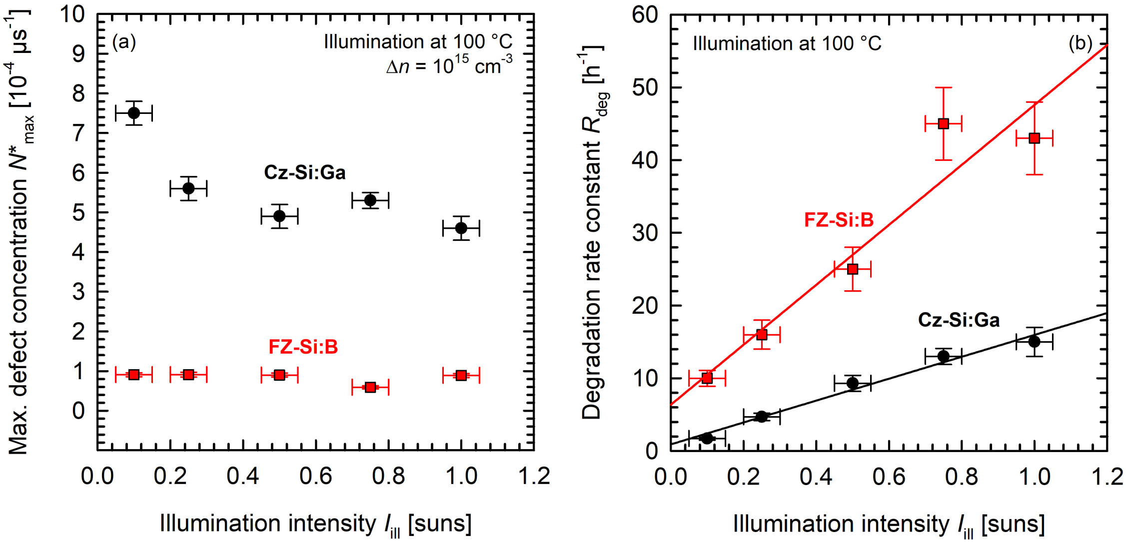

Figure 5.18: (a) Maximum defect concentration N^*_{max} and (b) degradation rate constant R_{deg} plotted versus the illumination intensity I_{ill} for Cz-Si:Ga (black circles) and FZ-Si:B (red squares). The temperature applied during the degradation is 100 °C for both sample types. The data in (b) are fitted using a linear regression.

As clearly visible in Fig. 5.18(a), for illumination intensities I_{ill} above 0.25 suns, N^*_{max} does not depend on the intensity I_{ill}. The increased N^*_{max} at $I_{\mathrm{ill}} = 0.1$ suns in the case of the Cz-Si:Ga sample was not observed on the FZ-Si:B material. This, however, could be related to the higher effective lifetime in FZ-Si:B in general, which leads to a higher excess carrier concentration Δn than in Cz-Si:Ga under the same illumination conditions. A shift of the increasing N^*_{max} in FZ-Si:B to lower intensities than $I_{\mathrm{ill}} = 0.1$ suns is therefore possible. Another explanation could be an impact of the permanent deactivation of the defect at elevated temperatures for higher illumination intensities. A delayed onset at lower illumination intensities could explain the higher maximum defect concentration N^*_{max} value, since both the activation and deactivation of the defect are most likely independent and parallel processes. However, a general dependence of the maximum defect concentration on the illumination intensity is not observed.

As can be seen in Fig. 5.18(b), the degradation rate constant R_{deg} increases linearly with the illumination intensity I_{ill} between 0.1 and 1 suns. The solid lines in Fig. 5.18(b) show linear fits using the equation:

$$R_{\mathrm{deg}} = a \times I_{\mathrm{ill}} + b. \tag{5.6}$$

The slopes a are determined to be $a_{\mathrm{Cz:Ga}} = (15 \pm 2)\,\mathrm{h}^{-1}\,\mathrm{suns}^{-1}$ and $a_{\mathrm{FZ:B}} = (41 \pm 8)\,\mathrm{h}^{-1}\,\mathrm{suns}^{-1}$. The y-intercept is $b_{\mathrm{Cz:Ga}} = (0.9 \pm 0.8)\,\mathrm{h}^{-1}$ and $b_{\mathrm{FZ:B}} = (6 \pm 5)\,\mathrm{h}^{-1}$. As we mentioned briefly at the end of Section 5.3, carrier injection is a necessary requirement for the defect activation. Naturally, the intercept with the y-axis, b, should therefore be zero. However, we have not collected any data at illumination intensities lower than 0.1 suns, where possible deviations from the linear correlation shown in Fig. 5.18(b) could be visible. We kept b hence fixed at non-zero values.

5.8 Permanent defect deactivation

Apart from the aforementioned temporary (non-permanent) deactivation of the responsible defect by low-temperature illumination (cf. Section 5.3), our experiments show that also a permanent deactivation is possible. Whereas the temporary deactivation requires illumination near room temperature (e.g., 0.5 suns, ~44 °C, see Figs. 5.3, 5.4, and 5.6), the permanent defect deactivation requires a prolonged illumination at high intensity and elevated temperatures (e.g., 1 sun, 135 °C). In Fig. 5.19, several defect activation and (temporary) deactivation cycles are shown for a Cz-Si:Ga sample interrupted by a permanent deactivation step (leading to a lifetime regeneration).

First, the lifetime is cycled between the active and in-active defect state six times by changing the conditions the sample is exposed to between 135 °C and 1 sun and 44 °C and 0.5 suns (Fig. 5.19(a)). After each defect activation at elevated temperature, the exposure to illumination at lower temperature leads to a complete deactivation of the defect. The sample is then exposed for approximately 4 hours to illumination at 135 °C, which leads to a slow recovery of the lifetime (regeneration, Fig. 5.19(b)). A subsequent cycling between both illumination conditions shows that the minimum lifetime now equals the lifetime value after prolonged illumination at 135 °C (Fig. 5.19(c)). This observation clearly supports that a permanent defect deactivation (leading to a lifetime regeneration) is possible.

Please note, however, that the prolonged illumination at 135 °C in Fig. 5.19(b) apparently does not lead to a complete permanent defect deactivation. A temperature dependence of the permanent deactivation is a possible explanation. However, we have not collected enough data on the regeneration behavior to state this as a fact.

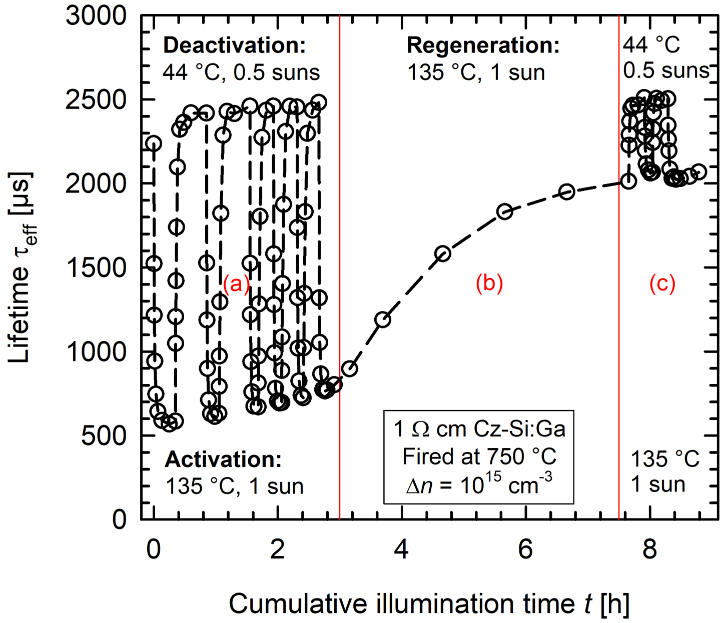

Figure 5.19: Repeated activation/deactivation cycles of the degradation effect in Cz-Si:Ga interrupted by a permanent deactivation step (Regeneration) under prolonged illumination at elevated temperature (i.e., 135 °C). The dashed line serve as guide to the eye.

5.9 Spatially-resolved lifetime measurements

We examine the degradation on an M2-sized (156.75 mm×156.75 mm, pseudo square) wafer spatially-resolved with a photoconductance-calibrated photoluminescence (PL) setup at 25 °C at a laser wavelength of 808 nm. The PL setup and its operating principle are introduced in Section 3.2.

The PL measurements are conducted in the initial state after processing, in the fully degraded states after illumination at 1 sun and temperatures ϑ of 80 °C, 100 °C, 120 °C, and 140 °C, and after (temporary) deactivation at ∼44 °C and 0.5 suns. The degradation at all four temperatures ϑ is conducted on the same Cz-Si:Ga wafer to better compare the results. As we have shown in Section 5.3, the LeTID defect activation is completely reversible by applying different illumination temperatures ϑ. The degraded state is determined by frequent lifetime measurements via PCD at the center position of the wafer in between illumination, analogously to the experiments before in this chapter. The PCD lifetime measurements are shown in Fig. 5.20(a) at a fixed excess carrier concentration of $\Delta n = 10^{15}\,\mathrm{cm}^{-3}$. In Fig. 5.20(b), the corresponding effective defect concentration $N_\mathrm{d}^*(t)$ is shown, as calculated via Eq. (5.1). Whereas the dashed lines in Fig. 5.20(a) serve as guide to the eye, the lines in Fig. 5.20(b) are exponential rise-to-maximum fits using Eq. (5.2).

The temperature-dependent degradation behavior of the Cz-Si:Ga wafer is clearly visible in Fig. 5.20. Furthermore, it is apparent that the PL measurement at a laser wavelength of 808 nm is sufficient to partially reset the LeTID defect activation. Each PL measurement included a total of 100 s of illumination at various laser

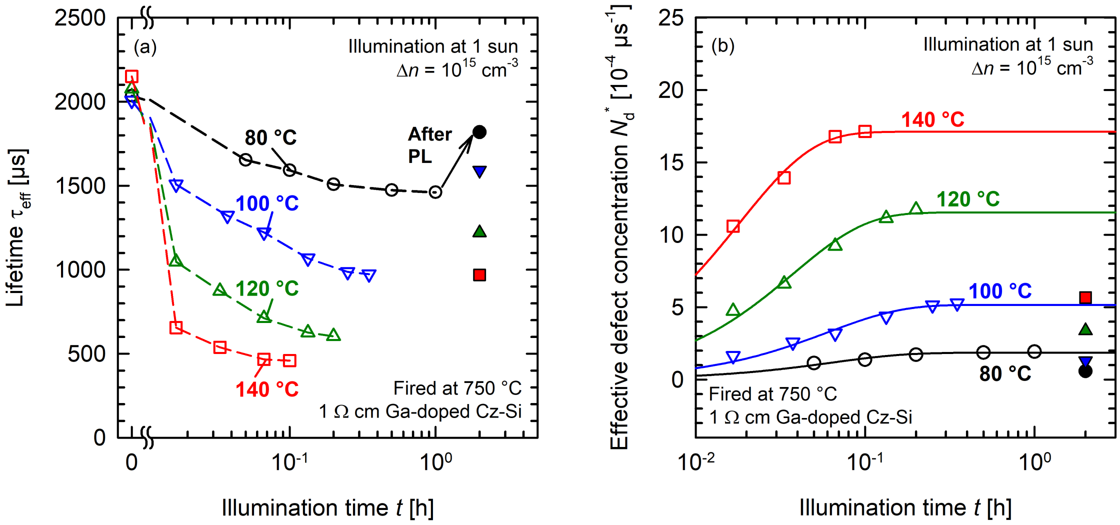

Figure 5.20: (a) Effective lifetime $\tau_\mathrm{eff}(t)$ at $\Delta n = 10^{15}\,\mathrm{cm}^{-3}$ using PCD and (b) the corresponding effective defect concentration $N_\mathrm{d}^*(t)$ measured on the same Cz-Si:Ga wafer illuminated at 1 sun at temperatures ranging from 80 °C to 140 °C (open symbols). The PCD data is measured at the center position of the wafer. The lifetime is measured spatially-resolved using PL before and after degradation at each temperature ϑ. After PL measurement the activated defect is partially recovered by the PL laser (closed symbols). The remaining defect centers are deactivated by low-temperature-illumination at ∼44 °C and 0.5 suns before increasing the temperature. The dashed lines in (a) serve as guide to the eye, the lines in (b) are exponential rise-to-maximum fits using Eq. (5.2).

intensities (cf. Section 3.2). The impact of the PL measurement on the observed LeTID effect will be discussed together with the spatially resolved analysis of $N_\mathrm{d}^*(t)$ later in this section.

Figure 5.21 shows the spatially-resolved lifetime at $\Delta n = 10^{15}\,\mathrm{cm}^{-3}$ after degradation at different temperatures. Note that the lower edge of approximately 1 cm of the pseudo-squared wafer (M2) is not visible in the images. In Fig. 5.21(a), the initial lifetime is shown before starting the degradation at elevated temperatures ranging from 80 °C to 140 °C. The lifetime is relatively homogeneous over the wafer with lifetimes close to 2000 µs, the highest lifetime above 2000 µs is localized in a u-shape around the center of the wafer. The lifetime is decreasing towards the edges within 1 to 2 cm. Figure 5.21(b) shows the lifetime after degradation for 1 h at 80 °C and 1 sun. Whereas the general features of the lifetime distribution remain the same, the lifetime is reduced throughout the wafer compared to the initial state in Fig. 5.21(a). The relative distribution of the degraded lifetime changes after illumination at temperatures higher than 80 °C. This is shown exemplarily after degradation for 6 min at 140 °C and 1 sun in Fig. 5.21(c). The highest lifetime is now located in a strip in the upper center instead of a u-shaped area around the center. In addition, five localized points of higher lifetime are visible. To examine the spatial distribution of the defect responsible for LeTID quantitatively, the effective defect concentration N_d^* is calculated pixelwise using the definition in Eq. (5.1). The corresponding analysis is shown in Fig. 5.22 for degradation at 1 sun and (a) 80 °C for 1 h, (b) 100 °C for 21 min, (c) 120 °C for 12 min, and (d) 140 °C for 6 min. The scaling of N_d^* was chosen logarithmically for better visibility of the different features throughout the four images.

In general, N_d^* increases towards the edges. The shape of this increase is explicitly not rotationally symmetric to the center of the wafer but has a rectangular shape and the difference between the lowest and highest N_d^* is in the range of one order of magnitude for each of the four degradation conditions. It is, however, important to note that the determined N_d^* at the center of the wafer using PL is lower by a factor 3 to 5 compared to N_d^* determined using PCD beforehand. This discrepancy can be attributed completely to a partial deactivation of the responsible LeTID defect by

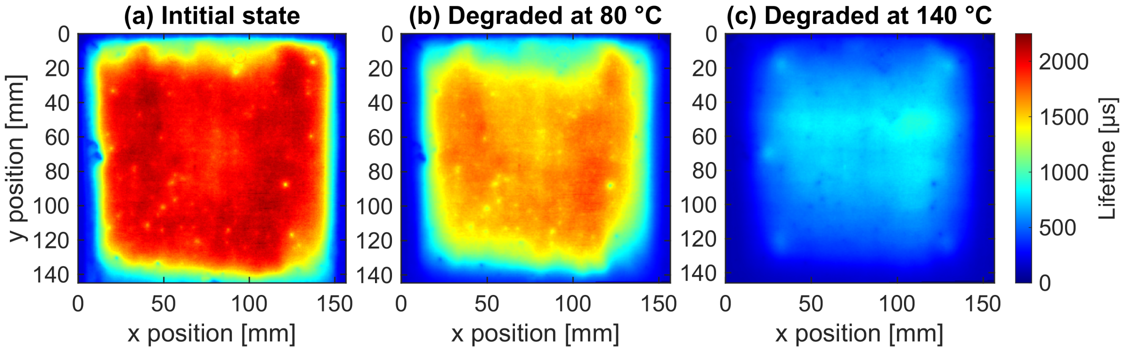

Figure 5.21: Spatially-resolved lifetime at $\Delta n = 10^{15}\,\mathrm{cm}^{-3}$ of an M2-sized Cz-Si:Ga wafer after degradation at different temperatures. (a) Initial state before starting the illumination at elevated temperatures, (b) degraded state after illumination for 1 h at 80 °C and 1 sun, and (c) after illumination for 6 min at 140 °C and 1 sun. The lower edge of approximately 1 cm of the pseudo-squared wafer (M2) is not visible in the images.

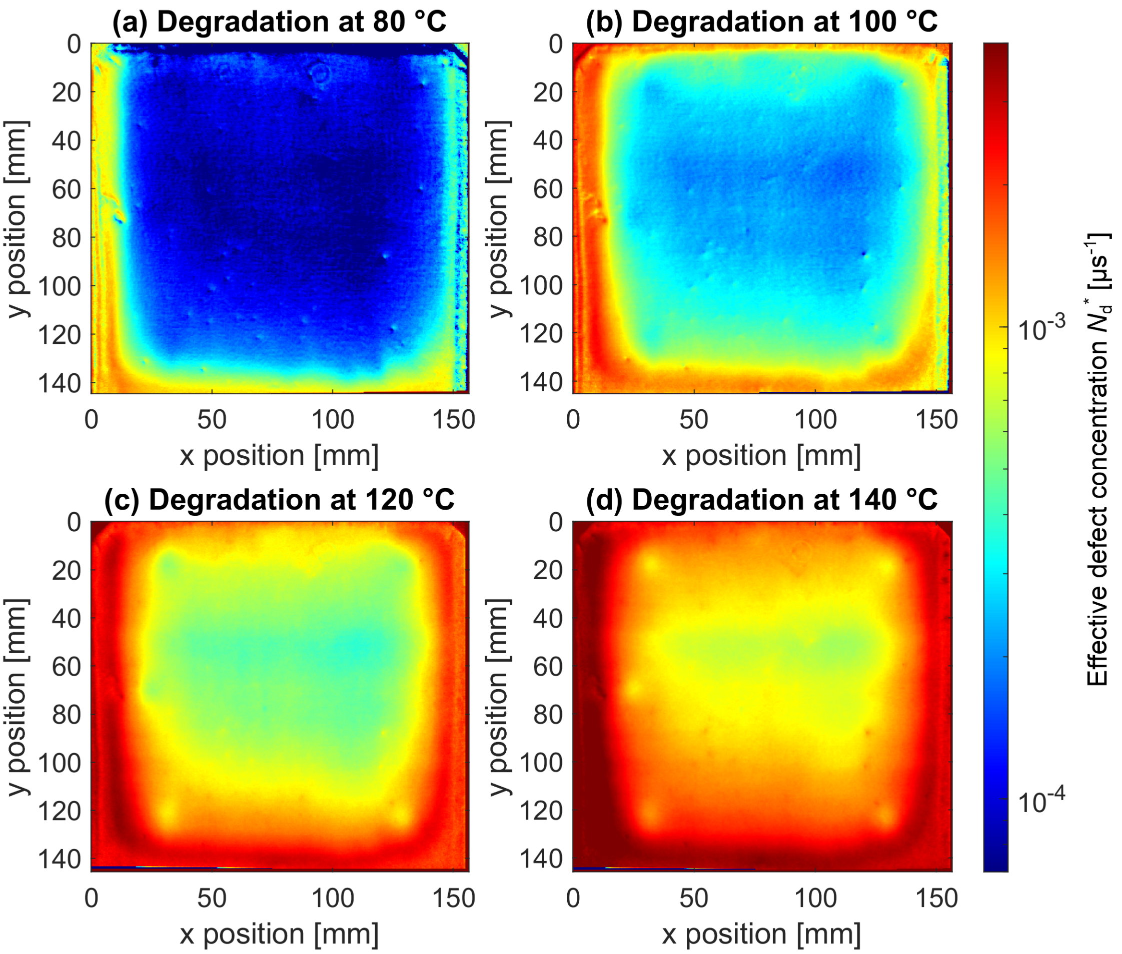

Figure 5.22: Spatially-resolved effective defect concentration N_d^* at $\Delta n = 10^{15}\,\mathrm{cm}^{-3}$ after degradation at 1 sun and (a) 80 °C, (b) 100 °C, (c) 120 °C, and 140 °C determined on the same wafer. The scaling of N_d^* was chosen logarithmically for better visibility of the different features throughout the four images. The lower edge of approximately 1 cm of the pseudo-squared wafer (M2) is not visible in the images.

the PL laser at a wavelength of 808 nm, which we are able to show by comparing PCD measurements before and after PL (cf. Fig. 5.20, open and closed symbols). The partial defect deactivation by the PL laser is similar to the temporary recovery by illumination at ∼44 °C and 0.5 suns typical for LeTID in Cz-Si:Ga. We did not observe any additional changes of the deactivated defect state by the PL laser.

It is important to assess if and how this significant impact of the PL measurement on the defect concentration N_d^* also influences the spatial distribution of N_d^* shown in Fig. 5.22. There are four possible influencing factors, which will be discussed in detail in the following:

(1) Determination of the fully degraded state via PCD at the center position of the wafer only,

(2) Intensity distribution of the PL laser over the wafer area,

(3) Impact of the absolute lifetime on the resulting excess carrier concentration Δn at a given intensity of the PL laser and thus the intensity within the

measurement sequence necessary to obtain $\Delta n = 10^{15}\,\mathrm{cm}^{-3}$ for any given spot on the wafer,

(4) Impact of the absolute lifetime on the resulting Δn at a given intensity of the PL laser assuming a Δn-dependence of the deactivation rate constant R_{de}.

(1) As stated at the beginning of this section, the PCD lifetime measurements to determine when the fully degraded state is reached are conducted at the center position of the wafer (cf. Fig. 5.20). We do not expect any spatial variations of the temperature on the wafer, the spatial variation of the illumination intensity, however, can be up to ±0.1 suns with the highest intensity localized near the center of the wafer. The impact of the illumination intensity on the maximum degradation extent around the intensity of 1 sun is negligible and has been discussed in Section 5.7. However, a lower intensity at the edges of the wafer leads to slower and therefore possibly incomplete degradation at the time of the PL measurement (cf. Section 5.7). Furthermore, since the dependence of the degradation rate constant R_{deg} on the intensity is likely a dependence on the excess carrier concentration Δn, a lower lifetime results in a lower R_{deg} and hence incomplete degradation at the wafer edges. However, the impact would be diametrical to the actually observed increase of N_{d}^{*} towards the edges, since the center of the wafer is evidently in the fully degraded state (cf. Fig. 5.20).
(2) We showed in Section 5.3 that a low temperature illumination (i.e., at ~44 °C and 0.5 sun) deactivates the LeTID defect temporarily (cf. Figs. 5.4 and 5.6). The PL laser at 808 nm does in fact the same. The laser beam is widened and distributed over the measuring area by means of a homogenizer (Focuslight, Off-Axis Beam Shaper IOS000292) to excite the sample. Fig. 5.23(a) shows a typical intensity profile as depicted in the corresponding data sheet [130]. It does depict a rectangular shape, which would indeed result in a decreasing defect concentration N_{d}^{*} towards the edges. However, as exemplarily shown for the y-direction in Fig. 5.23(b), the homogeneous area of highest intensity covers an area of approximately 190 mm × 170 mm and thus encompasses our entire M2-sized (156.75 mm × 156.75 mm) wafer. According to the manufacturer, inhomogeneity for each axis within this area is less than 7.5% (integrated over the other axis) [130]. Furthermore, Fig. 5.23(b) shows that the inhomogeneity is noise-like and does not decrease continuously towards the edges.

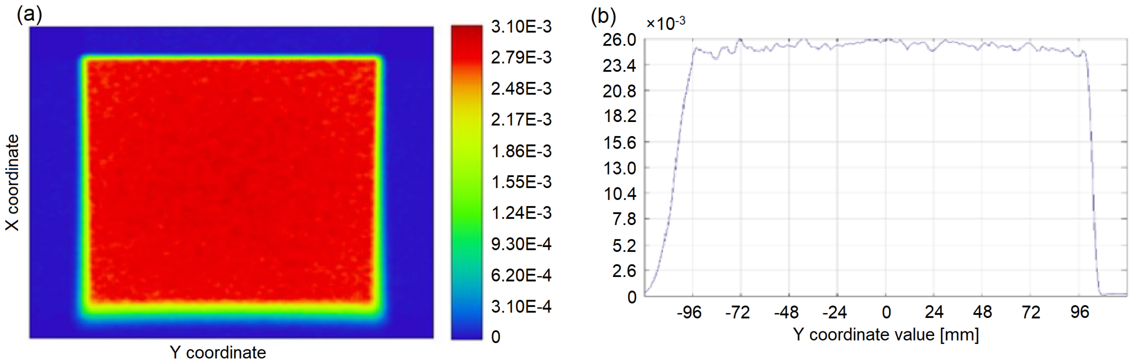

Figure 5.23: (a) Typical intensity profile formed by the laser homogenizer (Off-Axis Beam Shaper, IOS000292). (b) Intensity cross section of the y-direction. Picture and graph adapted from [130].

Therefore, we do not expect this noise-like variation of the laser intensity of less than 7.5% over the wafer area to produce a rectangular shape of increasing defect concentration N_{d}^{*} (cf. Fig. 5.22) by up to one order of magnitude between center and edge of the wafer.
(3) A higher lifetime results in a higher excess carrier concentration Δn at a fixed intensity of the PL laser. Since the lifetime is calculated on the basis of Δn under steady-state conditions, the lifetime directly affects the PL intensity necessary to determine the spatially-resolved lifetime at $\Delta n = 10^{15}\,\mathrm{cm}^{-3}$. To measure the injection-dependent lifetime, the laser power is varied systematically (from 50 to 0.5 W) to generate a step-wise decreasing PL intensity. Areas of higher lifetime mean an earlier stage within the PL measurement and thus a lower impact of the parasitic defect deactivation by the PL laser. As shown in Fig. 5.21, the lifetime decreases generally towards the edges of the wafer. Under the premise of a homogeneous defect concentration N_{d}^{*} we would therefore expect a higher N_{d}^{*} at the center of the wafer than at the edges.
(4) It has been shown that the kinetics of LeTID on mc-Si depend on Δn [74, 75]. In Section 5.7, we have shown that the apparent degradation rate constant R_{deg} increases linearly with the illumination intensity on our Cz-Si:Ga material. It is only logical to assume a similar correlation for the temporary deactivation under illumination at low temperatures or, equivalently, under illumination with the PL laser. Higher lifetimes towards the center of the wafer result in a higher Δn, which would result in a faster deactivation and hence a lower N_{d}^{*} after the PL measurement. However, N_{d}^{*} in Fig. 5.22 does not reflect the general lifetime distribution of the initial state before degradation shown in Fig. 5.21(a), as we would expect under the premise of a homogeneous defect concentration N_{d}^{*}. Hence, the presumed Δn-dependence of the deactivation rate constant R_{de} would only amplify an already existing inhomogeneity of N_{d}^{*}.
Because of the reasoning in (1)–(4), we conclude that the rectangular shape of N_{d}^{*} in Fig. 5.22 has a physical cause of unknown origin and is not generated by our measurement method. We do not expect the Czochralski method to have a dominant impact on the rectangular N_{d}^{*} distribution either, because any impact of the crystal growth process would be rotationally symmetric. There is also no correlation between N_{d}^{*} and the thickness W of the wafer, which is relatively homogeneous over the wafer area with $W = (150 \pm 10)\,\mathrm{\mu m}$. Possible causes could therefore be related to furnace- or cleaning steps or the deposition of the dielectric layers during processing. The five distinct spots of lower N_{d}^{*} visible in Fig. 5.22 besides the decrease towards the edges are related to supporting points of the conveyor belt within the firing furnace (a sixth spot on the right was probably not connected sufficiently). The connection leads to a better heat dissipation and thus likely to a lower peak temperature FT of the supported points of the wafer during the firing step. This locally reduced N_{d}^{*} is in agreement with our results in Section 5.4 regarding the impact of FT on the maximum degradation extent N_{max}^{*}

5.10 Conclusions and model

In this chapter, we have examined degradation phenomena in Cz-Si:Ga material and compared it with FZ-Si:B as the most defect-lean solar cell material available today. We performed a series of carrier lifetime experiments at elevated temperatures between 50 °C and 160 °C and illumination intensities ranging from 0.1 to 1 sun. We observed very similar temperature-dependent degradation effects in Cz-Si:Ga and FZ-Si:B wafers. This is particularly interesting since Cz-Si:Ga is expected to become the most commonly used material in industrial solar cell production in the near future. On basis of our experimental results, we summarize the defect characteristics in a state model for LeTID in both Cz-Si:Ga and FZ-Si:B as shown in Fig. 5.24.

The degradation is caused by illumination at elevated temperatures and fast-firing is a necessary trigger for LeTID to occur. The extent of degradation is strongly dependent on the applied temperature during illumination, with higher temperatures leading to a stronger degradation. The equilibrium state establishing itself between activated (state B) and deactivated (A) state of the defect is dependent on the temperature and the activation and deactivation are reversible processes. A complete (temporary) deactivation of the defect is possible at ∼44 °C and 0.5 suns. A similar behavior at low temperatures has bee reported for LeTID in mc-Si solar cells as well, however, with time constants at least one order of magnitude slower.

The maximum effective defect concentration N^*_{max} seems to be inhomogeneous over the wafer area with an apparent rectangular increase of N^*_{max} by around one order of magnitude toward the edges, which could be inflated, however, by an impact of our measurement method via PL. This indicates a certain influence of cleaning or furnace steps in the processing rather than manufacturing processes of the Cz- and FZ-material alone. For the latter, a central symmetry would be expected for Cz-Si:Ga. However, N^*_{max} is in general also one order of magnitude smaller on FZ-Si

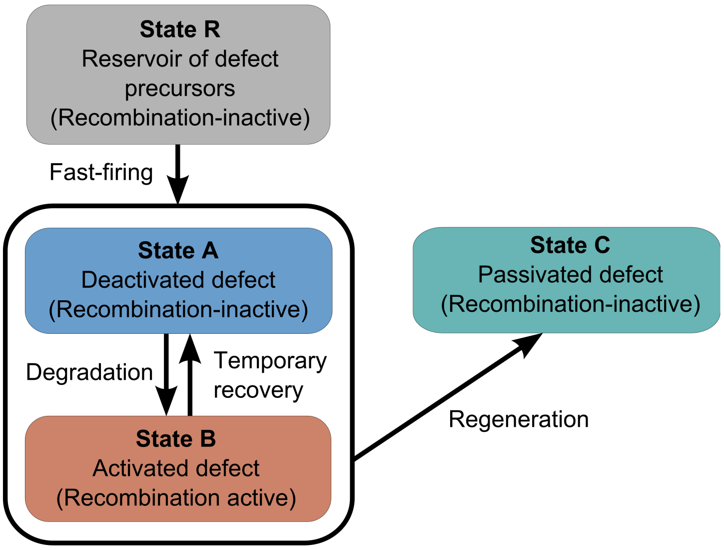

Figure 5.24: State model of the LeTID defect in Cz-Si:Ga and FZ-Si:B based on the experimental results presented in this chapter. Fast-firing is a necessary trigger for LeTID to occur (reservoir state R ↔ defect state A). The defect activation (defect state A ↔ B) is reversible and the equilibrium state between the defect states A and B is dependent on the temperature during illumination, since we do not observe a significant dependence on the illumination intensity aside from the formation rate constant. Through prolonged illumination at elevated temperatures a passivation of the defect is possible (defect state B → C).

material than on identically processed Cz-Si, which is likely related to the amount of impurities present in both materials due to the manufacturing process.

Both the extent of LeTID on Cz-Si:Ga at any given temperature between 80 and 160 °C and the dependence on the applied temperature increase significantly with increasing peak firing temperature FT and band velocity v_{band} of the fast-firing process applied. The latter is likely related to the cooling ramp after the peak firing temperature. However, no LeTID was observed at a measured peak firing temperature of 630 °C. With increasing refractive index of the silicon nitride passivation layers between $n = 2.07$ and 2.37, the LeTID effect in Cz-Si:Ga increases. These results are in agreement with previous studies on LeTID in B-doped multicrystalline and float zone silicon. Hydrogen, which diffuses into the silicon bulk during the fast-firing step, is hence a likely participant in the defect reaction responsible for LeTID in Cz-Si:Ga.

On the FZ-Si:B samples, which show similar temperature-dependent degradation behavior, however, no increase of N^*_{max} is observed with increasing refractive index n of the SiN$_y$ layers deposited prior to fast-firing. Parallel experiments to determine the hydrogen content in both Cz-Si:Ga and FZ-Si:B samples with different refractive indices n of the silicon nitride passivation layer indicate more hydrogen in-diffusion into the silicon bulk with increasing n between 2.07 and 2.37. Since we noted no dependence on the composition of the SiN$_y$ layer for our degradation experiments on FZ-Si:B, our results support the hypothesis of a second participant in the defect reaction of LeTID besides hydrogen, which limits the maximum defect concentration N^*_{max} for FZ-Si. FZ-Si is known to have a significantly reduced amount of impurities compared to Cz-Si due to the different manufacturing processes. Therefore, we expect a reservoir of defect precursors to be present before processing of the materials (state R). More experiments are necessary on Cz-Si:Ga regarding the possible formation of HGa defects to quantitatively extract the hydrogen content within the silicon bulk.

After conducting a thorough uncertainty analysis, we determined the apparent activation energy E_{A} of the LeTID effects in both materials and for all parameter variations to be in the range of (0.55 ± 0.10) eV. We conclude that most likely a specific defect mechanism is responsible for the LeTID effect examined in this study. The examined activation energy is significantly lower than reported in the literature for LeTID on mc-Si material, which are in the range of 1 eV. We hence conclude that the detailed defect physics is different in fired Cz-Si:Ga and FZ-Si:B, although hydrogen is most likely involved in all these degradation effects.

We observe no significant impact of the illumination intensity on N^*_{max}. Importantly, a permanent deactivation (state C) can be achieved by applying prolonged illumination at elevated temperatures ($\geq$135 °C) and light intensities around 1 sun.

6 Light- and elevated-temperature-induced degradation in poly-Si on oxide backjunction solar cells

6.1 Introduction

Light-induced lifetime degradation effects are frequently observed in many silicon-based materials for solar cell production. The most prominent one is the boron-oxygen (BO) defect activated under illumination in boron-doped Czochralski-grown silicon (Cz-Si) [6–8, 93]. Another degradation effect is the so called ”light- and elevated-temperature-induced lifetime degradation” (LeTID) first observed on block-cast multicrystalline silicon (mc-Si) [10, 11, 94]. Unlike the BO-related degradation, LeTID requires a previous fast-firing step at a high peak temperature [14, 66, 95]. LeTID-type effects have been reported in boron-doped Cz-Si [15, 16, 67], in float-zone silicon (FZ-Si) [17, 19, 67] and in n-type Cz-Si [69]. Gallium has been dominating the p-type mono-Si market for only a couple of years. According to data of the International Technology Roadmap for PV, boron as dopant for p-type material disappears in 2023 [22]. This is due to the absence of BO-related lifetime degradation. Several publications showed the significantly more stable performance of Ga-doped solar cells in comparison to B-doped solar cells[23, 97, 98, 131, 132]. However, there are also recent studies reporting lifetime instabilities on Ga-doped Cz-Si wafer materials [96–98, 127, 128, 133], and most recently performance degradation of Ga-doped PERC modules [132].

In Chapter 5, we showed that the temperature, at which the light-induced degradation is performed, has a strong impact on the extent of bulk lifetime degradation in Ga-doped Cz-Si. With increasing temperature the extent of degradation is also increasing. In Section 5.3, we demonstrated that illumination of $1\,\Omega\,\mathrm{cm}$ Ga-doped Cz-Si wafers performed at 140 °C may result in lifetimes in the fully degraded state τ_d of around $\sim 500\,\mu\mathrm{s}$ (initial lifetime τ_0 was $\sim 2300\,\mu\mathrm{s}$), after a fast-firing step is applied at a measured peak temperature of 750 °C and a band velocity of 6.8 m/min. Compared to degradation performed at 90 °C ($\tau_\mathrm{d} = 1300\,\mu\mathrm{s}$), this corresponds to an increase of the corresponding effective defect concentration N_d^* (cf. Eq. (5.1)) by a factor of 5. The reported lifetimes were measured at an excess carrier concentration of $\Delta n = 10^{15}\,\mathrm{cm}^{-3}$.

In this chapter, we examine whether the LeTID effect observed on Ga-doped Cz-Si wafers is also the cause of the existing but small instabilities observed in solar cells made on Ga-doped Cz-Si wafers. We fabricate poly-Si on oxide (POLO) backjunction (BJ) solar cells [53, 54] and perform degradation experiments at an illumination intensity of 1 sun at temperatures ranging from 80 °C to 160 °C.

6.2 Experimental details

Figure 6.1 shows the cell structure of a POLO BJ cell, as developed at ISFH [53, 54]. The process sequence starts with an industrial gallium-doped p-type Cz-Si wafer (M2 size) with a resistivity of 0.8 Ω cm. An (according to ellipsometry measurements) 1.6 nm-thick interfacial silicon oxide layer grown wet-chemically in de-ionized water with diluted ozone is capped by 200 nm of an in-situ phosphorous-doped poly-Si layer deposited by low-pressure chemical vapor deposition (LPCVD). During a high-temperature step at 840 °C in a quartz-tube furnace, the interfacial oxide layer breaks up and forms the POLO contact [25, 26, 134–136]. Simultaneously, 150 nm-thick oxide layers grow on poly-Si layers on both surfaces. The oxide layer on the cell front side is then completely removed. A subsequent KOH-based solution textures the front side, while the poly-Si layer at the cell rear side is protected by the thick oxide layer. We then deposit a stack consisting of 10 nm aluminum oxide (AlO_x) and 80 nm or 60 nm silicon nitride (SiN_y) with a refractive index of $n = 2.05$ on the cell front and rear sides, respectively. At the cell front, we locally open the dielectric stack by a laser to form contact openings. The contacts are realized by aluminum-paste screen printing at the front side and silver-paste screen printing at the rear side followed by a fast-firing process at a set-peak temperature of 810 °C and a band velocity of 6 m/min in an industrial conveyor belt furnace (centrotherm international, DO-FF-8.600-300).

After processing, the finished solar cells are illuminated by 1 sun light intensity (100 mW cm^{-2}) using a halogen lamp on a hotplate at elevated temperatures between 80 °C and 160 °C. We measure the illumination intensity with a calibrated reference silicon solar cell. The lateral variation of the illumination intensity is less than ±0.1 suns, while the temperature during the illumination time is constant within a range of ±2 °C. Depending on the experiment, the cells are either (i) illuminated at the above conditions for up to 1400 h (long-term stability test) or (ii) illuminated at a reduced intensity of 0.5 suns for ∼15 min, resulting in a recovery of the cell parameters after degradation. The cell temperature during this low-temperature

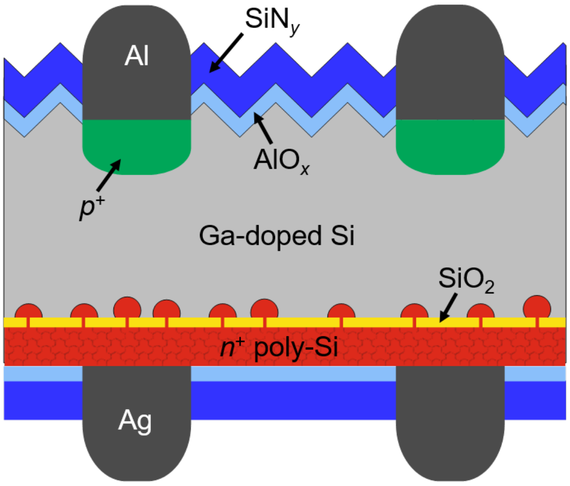

Figure 6.1: Schematic of the cross section of the POLO backjunction solar cell [53, 54] on Ga-doped Cz-Si.

illumination step is (44 ± 4) °C, as induced by the radiative heating of the halogen lamps.

The *IV* measurements are performed under AM1.5G illumination at 25 °C using a LOANA system from pv-tools [61]. Details on the measurement technique can be found in Section 3.4.2.

6.3 Long-term stability test at increased temperature

Figure 6.2 shows the evolution of the measured cell parameters energy conversion efficiency η (Fig. 6.2(a)), open-circuit voltage V_{oc} (Fig. 6.2(b)), fill factor FF together with the pseudo fill factor pFF (Fig. 6.2(c)), and the short-circuit current density J_{sc} (Fig. 6.2(d)) under one-sun illumination at 80 °C for up to 1400 h.

The efficiency η decreases from 22.10% to 21.95% within 10 h of one-sun illumination (Fig. 6.2(a)), before a recovery of η slightly up above the initial efficiency of 22.10% is observed. The maximum degradation extent amounts to ∼ 0.7% relative. Although some degradation is observable, the extent of degradation is very small, in particular when compared to solar cells made on B-doped Cz-Si wafers, where degradation extents of up to $10\%_{rel}$ have been reported [23]. The small LeTID effect visible in Fig. 6.2(a) has its cause in all three parameters shown in Fig. 6.2 (b–d), which are V_{oc}, FF, and J_{sc}. The extent of degradation, however, is only slightly

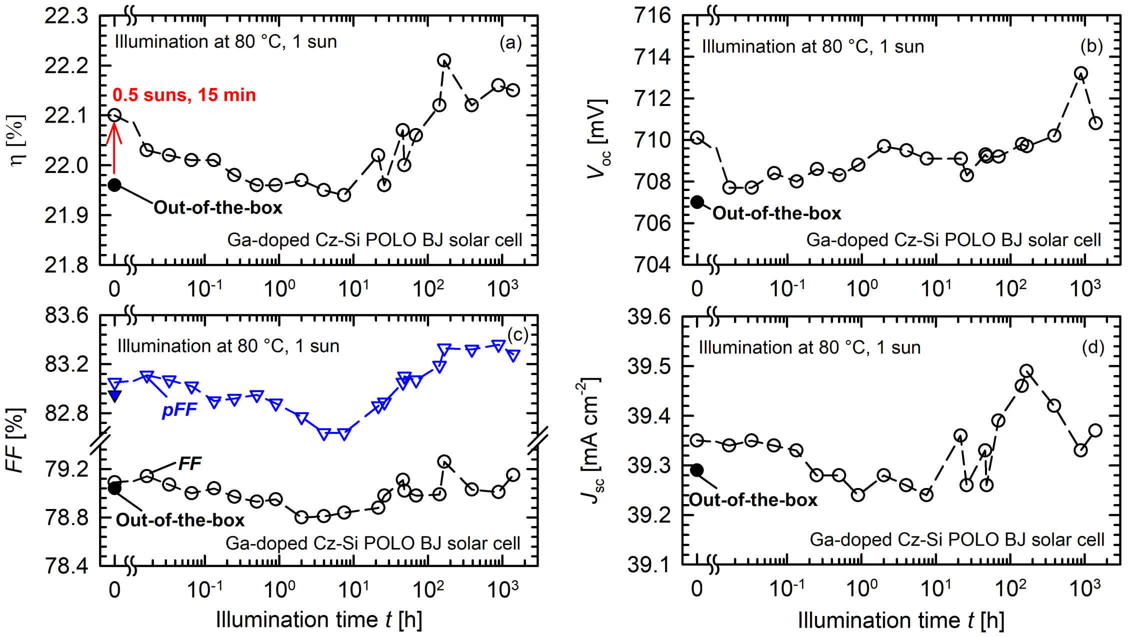

Figure 6.2: Long-term one-sun illumination of a POLO BJ solar cell on Ga-doped Cz-Si at 80 °C for 1400 h. Shown are the measured parameters (a) energy conversion efficiency η, (b) open-circuit voltage V_{oc}, (c) fill factor FF together with the pseudo fill factor pFF, and (d) short-circuit current density J_{sc} versus the illumination time t (open symbols). In addition, the initial values measured directly after fast-firing are shown (closed symbols). Before the experiment starts, the solar cell is illuminated at 0.5 suns for 15 min, increasing the efficiency from its initial value (slightly below 22.0%) to 22.1%.

larger than the initial improvement under illumination at 0.5 suns at ~44 °C for 15 min before increasing the temperature. Whether this is because an additional light-induced defect is activated or the presumed LeTID defect state after fast-firing is already activated and is deactivated again during low-temperature illumination (cf. Section 5.3) remains to be clarified, though lifetime experiments indicate the first option is more likely.

The short-circuit current density (Fig. 6.2(d)) of BJ solar cells is quite sensitive to the bulk lifetime. Minority charge-carriers generated primarily at the front side of the BJ solar cell have to diffuse to the rear side, where they are collected. A more pronounced decrease in J_{sc} is therefore expected for the activation of a bulk defect in back-junction solar cells compared to a conventional front-junction cell. The observed decrease in FF (Fig. 6.2(c), black circles) could be due to the activation of a bulk defect resulting in a pronounced injection dependence of the bulk lifetime thereby increasing the ideality factor n_{ideal} [65]. Please refer to Section 3.4.2 and [65] for more details regarding n_{ideal}. In the following, we will limit the discussion to the FF value. To exclude any influence of the series and contact resistances, the pseudo fill factor pFF is also shown in Fig. 6.2(c) (blue triangles). The pFF is extracted from the J_{sc}-V_{oc} measurement implemented in the LOANA tool [137, 138]. Indeed, less scattering of the data is visible while the general evolution of FF and pFF are the same. We have verified on reference samples that no degradation of the surface passivation occurs during the illuminated annealing treatments due to the relatively low firing temperature applied. Besides, the time constants of surface-related degradation are significantly larger than all time constants observed in the present study [139, 140].

However, changes of the surrounding conditions that have a non-neglectable impact on the IV measurement cannot be ignored during long-term measurements, most prominently the cell temperature T. The parameter mostly affected by changes in temperature T is the open-circuit voltage V_{oc}. Thereby the most relevant effects – beside the temperature dependence of V_{oc} itself as shown in Eq. (3.16) – are the pronounced temperature dependence of n_{i} and of the band gap, which decreases with increasing temperature (empirically described by Varshni [62]). In the relevant temperature range around 300 K, the V_{oc} measurement has an almost linear dependence on T with $\frac{\partial V_{\mathrm{oc}}}{\partial T} \approx -2\,\mathrm{mV/°C}$. This has been discussed in detail e.g., by Green [141] or Löper et al. [63].

Figure 6.3 shows (a) the cell temperature T during the IV measurements together with (b) the implementation of a temperature correction of the V_{oc} evolution of Fig. 6.2(b). The initial drop of V_{oc} from 710 mV to below 708 mV within 1 min of illumination(Fig. 6.3(b), black circles) coincides with an increase of T by 0.7 °C (Fig. 6.3(a)). A second strong deviation from the overall V_{oc} evolution is visible after 900 h of illumination. The V_{oc} value increases for a single measurement by 3 mV to 713.2 mV before dropping again after 1400 h of illumination. This time, it coincides with a rather significant drop in temperature during the IV measurement by almost 2 °C. The cause of this pronounced temperature change is difficult to understand in retrospect but possibly caused by changes in the environment or an insufficient warm-up of the measuring table (chuck). The blue inverse triangles in Fig. 6.3(b) represent an extrapolation of the V_{oc} measurement to 25 °C under the assumption of a linear impact of $\frac{\partial V_{\mathrm{oc}}}{\partial T} = -2\,\mathrm{mV/°C}$. Both the initial improvement of V_{oc} under

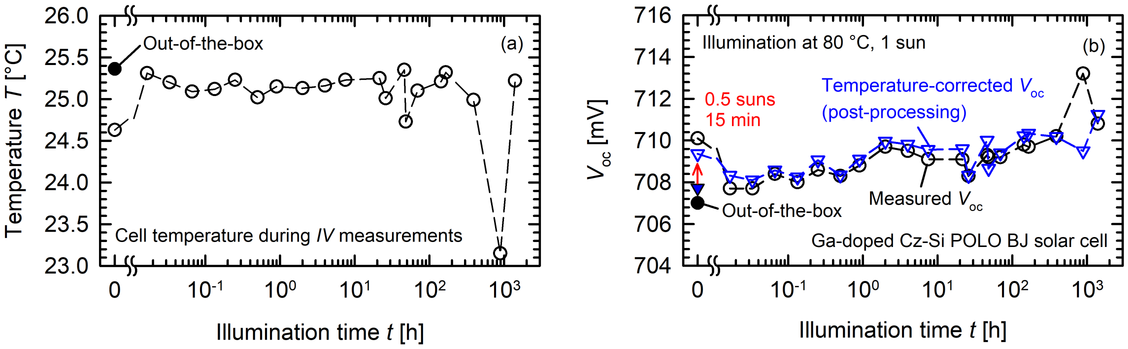

Figure 6.3: Impact of the cell temperature T during IV measurement on the V_{oc} measurement. (a) Cell temperature T of the Ga-doped POLO BJ cell during the IV measurements. (b) V_{oc} measurements already shown in Fig. 6.2(b) together with a temperature-corrected V_{oc} extrapolated to 25 °C.

illumination at 0.5 suns for 15 min and the fast drop under illumination at 80 °C and 1 sun are significantly reduced by the post processing. No significant degradation is evident in V_{oc} for 1400 h, the overall trend, however, shows an improvement of around 2 mV.

While the impact of T on the short-circuit current is caused by the decreasing band gap with increasing T, the fill factor depends on a range of cell parameters, including current and voltage operating levels [141]. However, the impact of T on both the FF and the J_{sc} measurement is significantly lower than on the V_{oc} measurement [141]. Furthermore, the more pronounced temperature fluctuations after 1 min and 900 h (cf. Fig. 6.3(a)), whose impact on the V_{oc} measurement was discussed in the last paragraph, are neither visible in the FF measurement (Fig. 6.2(c)) nor the measurement of J_{sc} (Fig. 6.2(d)), making the cell temperature T an unlikely cause of the observed fluctuations in both parameters.

In summary, we observe a small degradation of the conversion efficiency η of $\sim 0.7\%_{\mathrm{rel}}$ under illumination at 80 °C and 1 sun within 10 h followed by a recovery of η up above the initial efficiency within 100 h. The LeTID effect has its cause in FF and J_{sc}. Changes in V_{oc} are caused by slight instabilities of the temperature T during the IV measurements.

6.4 Temperature-dependent degradation on cell level

In a second step, we examine if the observed small LeTID effect shown in Section 6.3 has a temperature-dependent component and can be attributed to the temperature-dependent LeTID effect in Ga-doped Cz-Si lifetime samples, which we examined in detail in Chapter 5. Figure 6.4 shows a variation of the temperature ϑ during illumination between 80 °C and 160 °C at an illumination intensity of 1 sun. To make comparisons easier, the relative changes of the four cell parameters are depicted instead of the absolute values. Moreover, the data at $\vartheta = 80$ °C is the same as shown in Fig. 6.2. Here, for the sake of clarity, we focus the discussion to the relative data shown in Fig. 6.4. Figure 6.4(a) clearly shows that there is a dependence of the degradation extent on ϑ. Whereas at 80 °C the maximum decrease in conversion efficiency is only $0.15\%_{\text{abs}}$, the decrease at 140 °C is $0.4\%_{\text{abs}}$. This corresponds to an increase in the relative degradation extent from $0.7\%_{\text{rel}}$ to $2\%_{\text{rel}}$ as shown in Fig. 6.4(a). The maximum extent of relative degradation increases approximately linearly with increasing ϑ between 80 °C and 140 °C. For temperatures larger than 140 °C, the relative degradation decreases again, as can be seen in Fig. 6.4(a) (pink diamonds).

The cause of the degradation can be found in all three parameters shown in the Figs. 6.4(b) to 6.4(d). However, the pronounced temperature dependence is caused by the fill factor and the short-circuit current density changes. Whereas FF degrades by $0.4\%_{\text{rel}}$ at 80 °C, this maximum degradation increases to $1\%_{\text{rel}}$ at 140 °C. J_{sc} is reduced by $0.3\%_{\text{rel}}$ in the degraded state at 80 °C compared to its initial value. This degradation increases to $0.6\%_{\text{rel}}$ at 140 °C. Due to relatively small V_{oc} changes in comparison with the scattering of the measurement data, no dependence of the V_{oc} degradation on ϑ is visible in the data. This also does not change by conducting a temperature correction of the V_{oc} measurement, as describe in the previous section in Fig. 6.3. Figure 6.5 shows (a) the cell temperature T during the IV measurements of the temperature variation (denoted by ϑ) under illumination and (b) the temperature-corrected relative V_{oc} changes. No temperature-dependent degradation of V_{oc} is observable due to scattering of the data even after the temperature-dependent data is extrapolated to 25 °C. A possible explanation why the LeTID effect observed on Ga-doped POLO BJ solar cells is not visible in V_{oc} will be given in Section 6.5.

To exclude any influence of series and contact resistances on the temperature-dependent degradation of the fill factor FF in Fig. 6.4(c), the pseudo fill factor

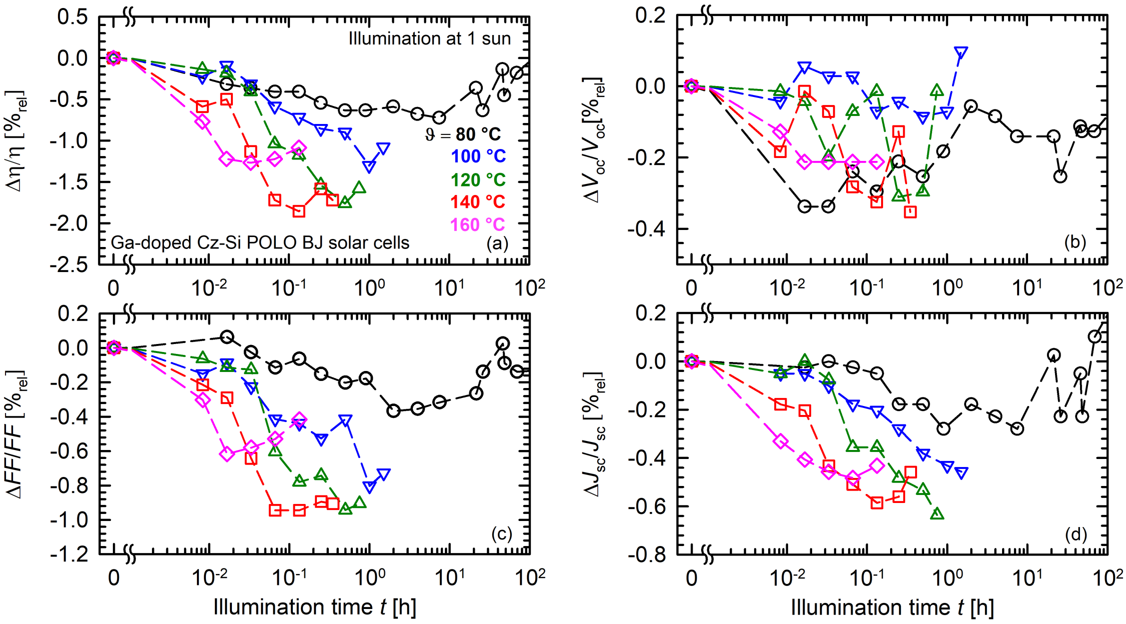

Figure 6.4: Temperature-dependent light-induced degradation of Ga-doped Cz-Si POLO BJ solar cells at 1 sun light intensity and temperatures ranging from 80 °C to 160 °C. Shown are the relative changes in the measured cell parameters (a) energy conversion efficiency η, (b) open-circuit voltage V_{oc}, (c) fill factor FF, and (d) short-circuit current density J_{sc} versus the illumination time t.

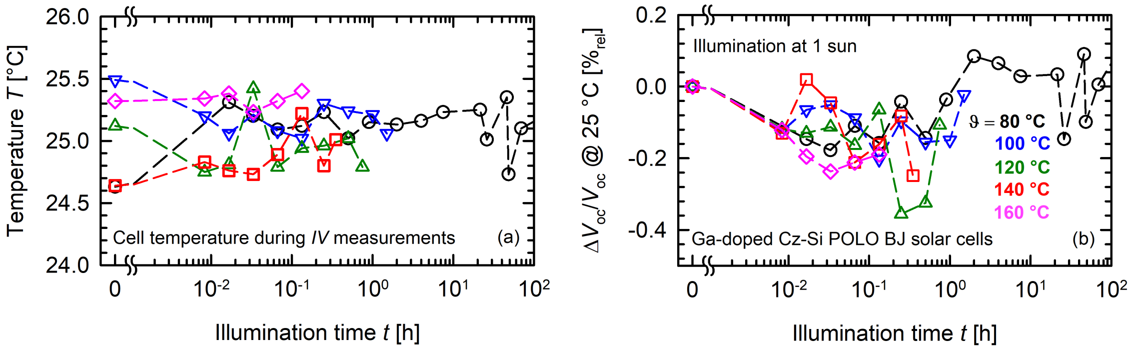

Figure 6.5: Impact of the cell temperature T during IV measurement on the V_{oc} measurement shown in Fig. 6.4(b). (a) Cell temperature T of the Ga-doped POLO BJ cell during the IV measurements of the temperature variation (denoted by ϑ) under illumination. (b) Relative V_{oc} change extrapolated to 25 °C. No temperature-dependent degradation is observable due to scattering of the data.

pFF is shown in Fig. 6.6(a). In Fig. 6.6(b) the relative changes are shown analogously to the representation in Fig. 6.4(c). Both Fig. 6.6(a) and Fig. 6.6(b) confirm the independence of the observed degradation on the series resistance. The degradation extent of pFF increases from $0.5\%_{\mathrm{rel}}$ at 80 °C to $1.2\%_{\mathrm{rel}}$ at 120 °C, before a saturation (140 °C) followed by a decrease (160 °C) of the maximum degradation extent can be observed in Fig. 6.6(b).

Note that the degradation data recorded in the temperature range from 100 °C to 160 °C in Fig 6.4 were actually all measured on the same solar cell. After complete one-sun degradation at different temperatures (100 °C to 160 °C), the cell is illuminated at a lower intensity of 0.5 suns, which corresponds to an illumination temperature of ~44 °C without active heating of the cell. All four parameters η, V_{oc}, FF, and J_{sc} increase again and reach values comparable with the ones before degradation. Afterwards, a degradation at elevated temperature is again possible. The (temporary) recovery takes about 15 to 30 min at 0.5 suns and ~44 °C. Details on the mechanism of temporary recovery at low temperatures, which we only mentioned here briefly, can be found in Section 5.3. In summary, the LeTID effect

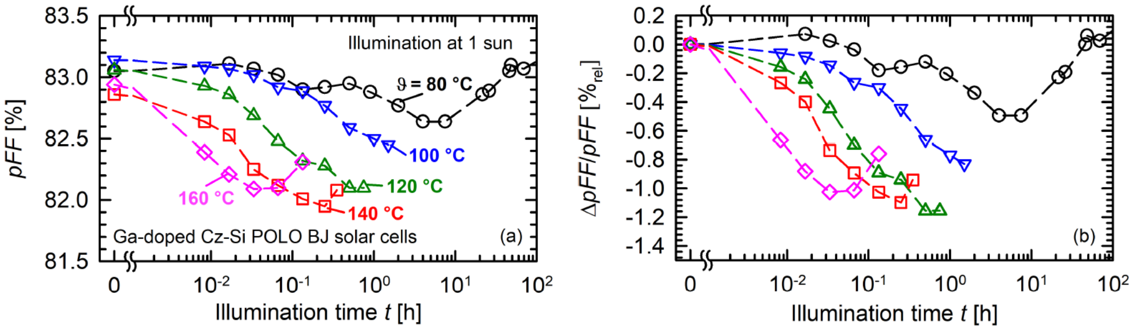

Figure 6.6: Temperature-dependent light-induced degradation of the pseudo fill factor pFF of Ga-doped Cz-Si POLO BJ solar cells at 1 sun light intensity and temperatures ranging from 80 to 160 °C. Shown are (a) the absolute changes and (b) the relative changes versus the illumination time t.

observed in this section is very similar to the temperature-dependent LeTID effect which we characterized on Ga-doped Cz-Si lifetime samples in Chapter 5.

6.5 Ga-doped Cz-Si lifetime reference sample

The measurements on solar cells show very similar behavior as our lifetime measurements performed on Ga-doped Cz-Si wafers in Chapter 5, which is a clear indication that the activation of a bulk defect is responsible for the observed LeTID effect. Figure 6.7 shows the corresponding lifetime measurements performed on a reference Ga-doped Cz-Si wafer with passivated surfaces processed in parallel to the POLO BJ cells (one-sun illumination at 80 °C to 160 °C). The sample corresponds to a solar cell without metalization on the front and rear side. The lifetimes are measured by the photoconductance decay (PCD) method at ∼30 °C using a WCT-120 lifetime tester from Sinton Instruments, the operating principle of which is explained in detail in Section 3.1.

Carrier lifetimes measured at an excess carrier concentration of $\Delta n = 10^{15}\,\mathrm{cm}^{-3}$ are shown in Fig. 6.7(a). After each degradation experiment at constant ϑ, the defect is deactivated at 0.5 suns at 44 °C before increasing the temperature for the next degradation experiment. The temperature dependence of the degradation extent is clearly visible. The effective defect concentration which can be extracted from the lifetime data according to Eq. (5.1) increases by a factor of ∼5 between degradation at 80 °C and 140 °C. As we have shown in Section 5.4, the firing parameters have a significant impact on the extent of degradation. However, the extent of degradation shown in Fig. 6.7 is significantly less pronounced than what we would have expected from our results presented in Section 5.4. If put into perspective with the results

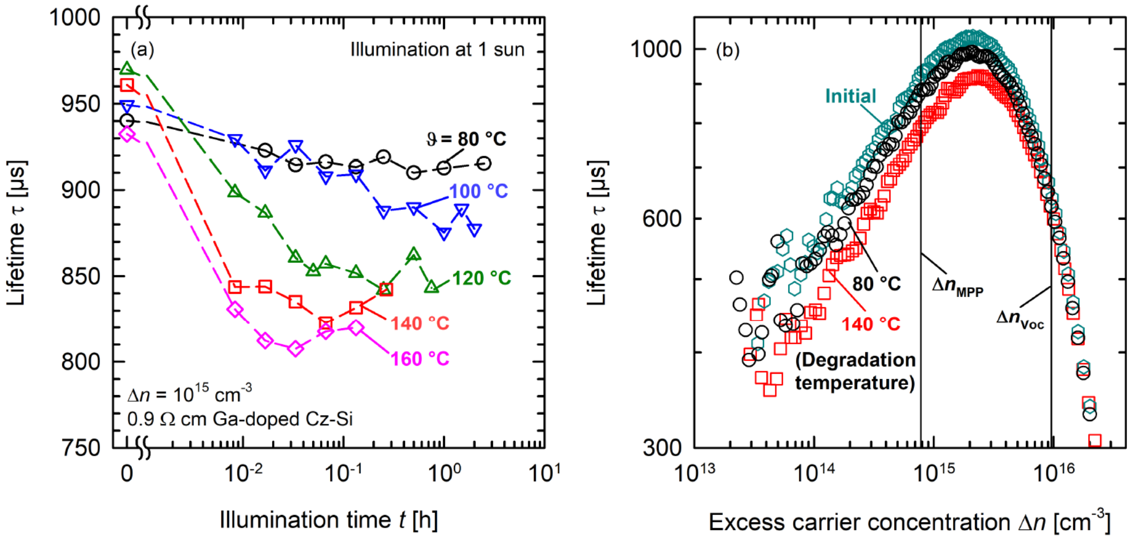

Figure 6.7: Lifetime degradation of a Ga-doped Cz-Si wafer (cell without metalization) during one-sun illumination. Shown is (a) the lifetime degradation at temperatures ranging from 80 to 160 °C at one-sun illumination and (b) the injection-dependent lifetimes before degradation (initial, cyan hexagons) and after degradation for 30 min at 80 °C (black circles) and 4 min at 140 °C (red squares).

shown in Fig. 5.10, the extent of degradation is comparable to the $FT = 680\,^\circ\mathrm{C}$ data in Fig. 5.10(a) or the $v_{\mathrm{band}} = 3.8\,\mathrm{m/min}$ data in Fig. 5.10(b). However, the firing parameter applied in this chapter were $FT = 790\,^\circ\mathrm{C}$ and $v_{\mathrm{band}} = 6.0\,\mathrm{m/min}$. Note, that the measured peak firing temperature FT in this chapter is much closer to the set-peak temperature of 810 °C than in the previous chapters due the the textured front surface, which enables a more efficient heat transfer. The cooling ramp calculated analogously to Fig. 5.11 amounts to 74 °C/s, which puts our lifetime reference sample at the right end of Fig. 5.11(b). Hence, we would expect maximum degradation. An important difference, however, that has to be taken into account is the sample structure with poly-Si on the rear of our lifetime reference sample instead of a symmetrical stack of AlO_x and SiN_y on both wafer surfaces as applied in Section 5.4. Poly-Si is known to has an impurity gettering effect [142–145]. To exactly reveal the causes for the differences between the different lifetime structures in the present chapter and Chapter 5, more specific experiments are required.

Figure 6.7(b) shows the injection-dependent lifetimes before degradation (initial, cyan hexagons) and after degradation for 30 min at 80 °C (black circles) and 4 min at 140 °C (red squares) for our reference lifetime sample. In addition, the approximate excess carrier concentrations are shown for the maximum power point (MPP) Δn_{MPP} and under open-circuit conditions $\Delta n_{V_{\mathrm{MPP}}}$ (black lines). Whereas the difference between the degradation at 80 °C and 140 °C is clearly visible at Δn_{MPP}, it is almost non-existent at the much higher $\Delta n_{V_{\mathrm{MPP}}}$. This explains why the temperature dependence of the defect activation is clearly visible in FF (Fig. 6.4(c)) and pFF (Fig. 6.6), whereas V_{oc} shows mainly scattering (Fig. 6.4(b)).

6.6 Permanent defect deactivation and absolute improvement on device level

A long-term-stable improvement of the cell performance by up to $0.2\%_{\mathrm{abs}}$ is possible by prolonged illumination at elevated temperatures (e.g., at 140 °C and 1 sun for 5 h). Figure 6.8 shows several consecutive defect activation/deactivation cycles on the same solar cell. The experiment has been conducted similarly to that presented in Section 5.8. However, for the sake of clarity and unlike in Figs. 6.2 and 6.4, in Fig. 6.8 only the respective highest and lowest values of each cycle are shown instead of the full degradation curves. The x-axes do show the progress of the experiment from the left to the right by numbering the respective deactivation and activation step consecutively. Each of the four subplots (a–d) in Fig. 6.8 for η, V_{oc}, FF, and J_{sc} is separated into 3 stages (1–3) analogously to Fig. 5.19.

The first stage (1) includes three consecutive cycles of defect deactivation (black circles, upper axis) at ∼44 °C and 0.5 suns and defect activation (red squares, lower axis) at 140 °C and 1 sun. It shows the reversibility of the degradation effect under constant defect activation conditions. Please note, however, that the decreasing trend of the degraded FF in Fig. 6.8(c,1) has no significance. The reason is simply that we chose to display the respective lowest values of the conversion efficiency without taking the scattering in the FF measurement into account.

Stage (2) of each subplot (a–d) in Fig. 6.8 shows the state after a prolonged illumination at 140 °C and 1 sun for 5 h. According to our results on Ga-doped Cz-Si

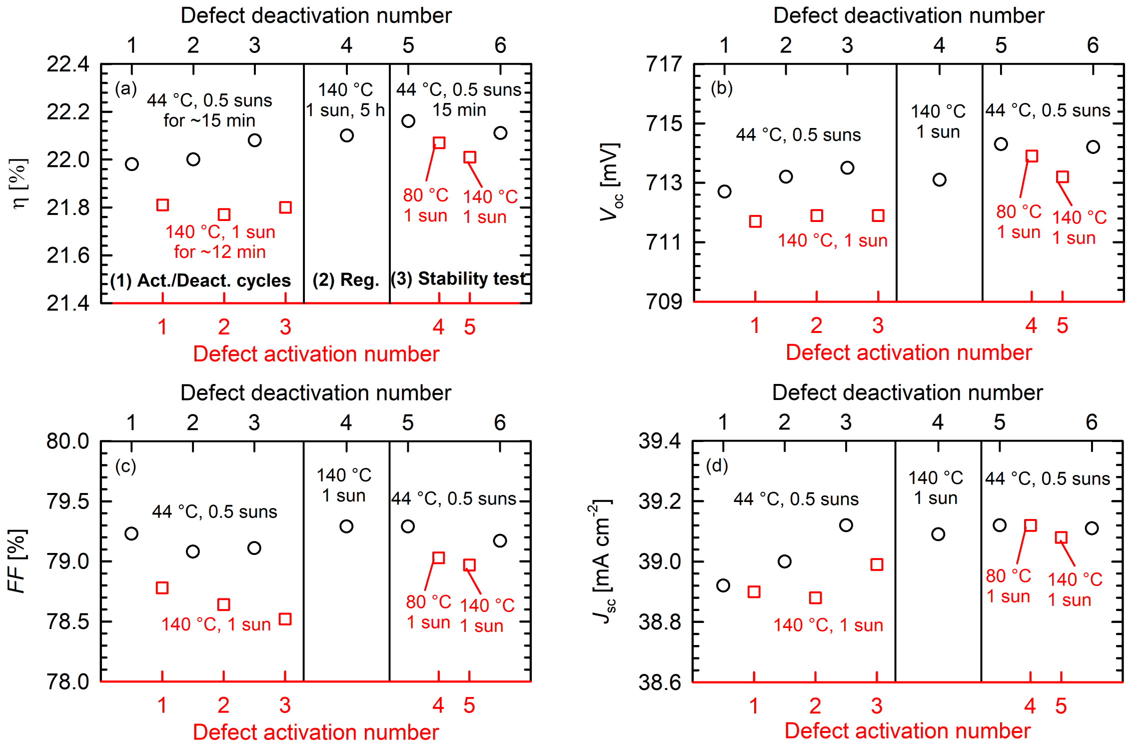

Figure 6.8: (1) Reversibility of a Ga-doped Cz-Si POLO BJ solar cell through consecutive activation (140 °C, 1 sun, 12 min) and deactivation (44 °C, 0.5 suns, 15 min) cycles, (2) regeneration through prolonged illumination at elevated temperatures (140 °C, 1 sun, 5 h), and (3) test of the stability of the regeneration at 80 and 140 °C. Shown are the measured cell parameters (a) energy conversion efficiency η, (b) open-circuit voltage V_{oc}, (c) fill factor FF, and (d) short-circuit current density J_{sc}.

lifetime samples presented in Section 5.8, this treatment results in a permanent defect deactivation which corresponds to a permanent regeneration of the bulk lifetime. The conversion efficiency η in Fig. 6.8(a,2) reaches a value of 22.10%. To test the stability of the regenerated solar cell, we apply in stage (3) another defect deactivation/activation cycle, starting with the low-temperature illumination at 0.5 suns and 44 °C (deactivation). The conversion efficiency η improves further to 22.16%, which is an improvement of $0.2\%_{\mathrm{abs}}$ compared to the initial η of 21.96% at the very beginning of the experiment. This general improvement is visible in the black circles in Fig. 6.8(a) and can be attributed to an increase of both V_{oc} (Fig. 6.8(b)) and J_{sc} (Fig. 6.8(d)). A similar improvement of the cell performance has been reported on Ga-doped Cz-Si PERC solar cells by means of a two-step bias treatment [146]. Subsequently, in stage (3) of Fig. 6.8, the stability of the regenerated cell is tested in a two-step increase of the temperature, first to 80 °C, then to 140 °C at a constant illumination intensity of 1 sun (red squares). A significantly reduced degradation of only $0.15\%_{\mathrm{abs}}$ after illumination at 140 °C and 1 suns is now observed, which is halved compared to the degradation before the regeneration step was applied. Even after maximum degradation at 140 °C an efficiency of 22.0% is obtained. The regeneration treatment can hence be regarded as highly effective and the results are in agreement with our experiment on lifetime samples presented in Section 5.8.

6.7 Conclusions

In this chapter, we have performed illumination experiments at elevated temperatures between 80 °C and 160 °C and 1 sun halogen lamp intensity on POLO BJ cells with Ga-doped Cz-Si base. These solar cells were shown to be relatively stable regarding light-induced degradation, which we have demonstrated through long-term illumination at 80 °C for 1400 h. We observed, however, a slight degradation of the cell performance, the extent of which increases with increasing temperature. Whereas at 80 °C the degradation in energy conversion efficiency is $0.15\%_{\mathrm{abs}}$, the degradation extent is increased to $0.4\%_{\mathrm{abs}}$ under illumination at 140 °C. This corresponds to an increase in the relative degradation extent from $0.7\%_{\mathrm{rel}}$ at 80 °C to $2\%_{\mathrm{rel}}$ at 140 °C. For temperatures larger than 140 °C, the degradation extent decreases again. Through illumination at low temperatures and illumination intensities (i.e., at 44 °C and 0.5 suns) – quite common conditions during operation in the field – the degradation effect can be temporarily reversed. Interestingly, the temperature-dependent degradation of the energy conversion efficiency can be ascribed to a reduction of the short-circuit current density J_{sc} and the fill factor FF, whereas we do not observe any significant temperature-dependent degradation of the open-circuit voltage V_{oc}. This could be explained by the injection dependence of the lifetime of the activated defect, resulting in a more severe degradation of the lifetime for excess carrier concentrations at the maximum-power-point than under open-circuit conditions. J_{sc} is also quite sensitive to the bulk lifetime due to the structure of a BJ solar cell with the collection of the minority carriers (i.e., electrons in our cell) at the rear side of the solar cell. Measurements on a lifetime sample processed in parallel to the solar cells (corresponding to a cell without metalization on the front and rear sides) and the similarities of the degradation trends to the temperature dependence of degradation examined in detail in Chapter 5 clearly indicate that the activation of a bulk defect is responsible for the observed LeTID effect on the Ga-doped Cz-Si solar cells. We ascribed this effect to hydrogen, which diffuses into the silicon bulk during the firing step.

Through prolonged illumination at elevated temperatures (e.g., at 140 °C and 1 sun for 5 h), an improvement of the energy conversion efficiency by up to $0.2\%_{\mathrm{abs}}$ due to an absolute increase of both the open-circuit voltage and the short-circuit current density was observed. During this treatment, a partial permanent deactivation of the defect responsible for degradation takes places, though degradation can still occur after regeneration with half the degradation extent as observed before permanent deactivation. Stable solar cell efficiencies above 22% were measured after regeneration, meaning that within the uncertainty range of the efficiency measurement, the developed cells on Ga-doped Cz-Si can be classified long-term stable after regeneration.

7 Degradation and regeneration of poly-Si on oxide surface passivation quality

7.1 Introduction

Polycrystalline silicon on oxide (POLO) layers have attracted great attention in recent years in the field of photovoltaic research, although first proposals to use them in solar cell production are much older [24]. Highly doped polycrystalline silicon (poly-Si) layers on passivating interfacial silicon oxide represent an advanced method to realize carrier-selective passivated contacts in high-efficiency silicon solar cells. It combines excellent passivation quality with saturation current densities (J_0) down to 0.6 fA/cm^2, as reported on planar test structures [25, 26], in combination with very low contact resistivities (0.6 mΩ cm^2 on n^+ POLO junctions) [27]. Outstanding energy conversion efficiencies of 26.1% for interdigitated back-contact solar cells [147] and 25.8% for double-side-contacted solar cells have already been reported [148]. Fast-firing or, as we call it in this chapter, Rapid thermal annealing (RTA) of POLO is highly relevant for the implementation of poly-Si-based passivating contacts into industrial-type solar cells with screen-printed and fired contacts [149, 150]. This chapter deals with possible instabilities of the silicon bulk as well as the poly-Si-passivated surface that might be caused by an industrial-type firing step, which is already known to cause a series of other mostly bulk-related defects [13, 16]. So far, however, there are only a few studies dealing with the degradation and regeneration of the silicon surface passivation, e.g. by Sperber et al. [29] for dielectric passivation layers and by Yang et al. [151] regarding poly-Si-based surface passivation after a fast-firing step has been applied. In the latter publication [151], the authors report degradation of phosphorus-doped poly-Si surface passivation upon illumination at above 150 °C and an improvement of surface passivation at temperatures above 250 °C upon illumination or dark annealing.

In this chapter, we examine carrier lifetime instabilities due to changes in in-situ phosphorus-doped POLO passivation layers during illumination and annealing in the dark at different temperatures on both boron-doped and phosphorus-doped Cz-Si wafers. We will examine similar samples but with different thermal histories which affects also the structure of the poly-Si layer.

7.2 Experimental details

Symmetrical lifetime samples were processed on random-pyramid-textured 1.7 Ω cm boron-doped p-type Cz-Si and 5.0 Ω cm phosphorus-doped n-type Cz-Si wafers with a wet-chemically ozone-grown interfacial silicon oxide layer (~1.6 nm thick) and 150 nm (on p-type wafers) or 50 nm (on n-type wafers) in-situ doped n^+ poly-Si layers on top deposited by low-pressure chemical vapor deposition (centrotherm international, E1200 LPCVD furnace). Please note that in fact amorphous silicon (a-Si) layers are deposited during LPCVD, which are crystallized to poly-Si layers in a high-temperature (HT) step performed at ~900 °C for ~30 min in a nitrogen atmosphere. If not explicitly mentioned, this HT step is omitted in this study, pursuing the "firing only" approach as presented e.g. by Ingenito et al. [149]. The lifetime samples were capped by 10 nm AlO_x films used as a possible hydrogen source for interface passivation [152, 153] deposited using plasma-assisted atomic layer deposition (Oxford Instruments, FlexAl). Both p- and n-type wafers were exposed afterwards to a low-temperature annealing step at 425 °C (15 min). The entire stack therefore consists of c-Si/SiO_y/poly-Si/AlO_x. The p-type silicon wafers received a fast-firing treatment (referred to as rapid thermal annealing, RTA) at 800 °C set-peak temperature and a belt speed of 7 m/min in an industrial conveyor-belt firing furnace (centrotherm international, DO-FF-8.600-300). The n-type silicon wafers were subdivided into four different groups and exposed to different temperature steps: (a) RTA at 800 °C set-peak temperature at a belt speed of 7 m/min (referred to as RTA-samples), (b) a HT step at 900 °C for 30 min in a quartz-tube furnace performed directly after LPCVD a-Si deposition, and (c) a high-temperature step at 860 °C for 30 min after a-Si deposition plus an RTA step at 800 °C at a belt speed of 7 m/min (HT+RTA). The n-type silicon wafers, which received no additional treatment in addition to the low-temperature annealing step at 425 °C for 15 min, serve as a reference ((d), annealed). After sample processing, we applied two different experimental conditions: (i) Exposure to a 100 mW/cm^2 (1 sun) halogen-lamp illumination at a temperature of 185 °C, and (ii) dark-annealing at three different temperatures (200 °C, 300 °C, and 400 °C) on a hot-plate in ambient environment. Most of the samples annealed in the dark were subsequently illuminated at 80 °C and 1 sun. A summary of the experimental conditions is shown in Table 7.1.

For our experiments, the processed wafers are cut into 5 cm × 5 cm samples using

Table 7.1: Diagram of the conducted experiments sorted by wafer material and thermal history defining the samples. All samples are passivated by n^+ poly-Si on ozone-grown interfacial oxide. The HT step is carried out directly after deposition of a-Si, which is crystallized to poly-Si in the process. The additional capping layers of AlO_x serve as a possible hydrogen source for interface passivation.

Wafer	**Wafer preparation (thermal history)**				**Hot plate treatments & duration**		
p-type	ⓐⓐ		Al_2O_3 + Anneal 425 °C 15 min	Firing 800 °C (**RTA**)	①	Illumination (**1 sun**) 185 °C	1000 h
					②	Dark anneal (**DA**) 200 °C	1000 h
n-type	ⓑ	High temperature anneal 900 °C (**HT**) 30 min	Al_2O_3 + Anneal 425 °C 15 min		③③	Dark anneal (**DA**) 300 °C, 20 h	**1 sun**, 80 °C 1000 h
	ⓒ	High temperature anneal 860 °C (**HT**) 30 min	Al_2O_3 + Anneal 425 °C 15 min	Firing 800 °C (**RTA**)	④	Dark anneal (**DA**) 400 °C, 3 h	
	ⓓ		Al_2O_3 + **Anneal** 425 °C 15 min				

a laser. The effective carrier lifetime $\tau_{\mathrm{eff}}(t)$ is measured as a function of the excess carrier concentration Δn by the photoconductance decay (PCD) method at ~30 °C using a WCT-120 lifetime tester from Sinton Instruments, the operating principle of which is explained in detail in Section 3.1. The τ_{eff} evolution of the p-type samples is analyzed at different Δn values between $2 \times 10^{14}\,\mathrm{cm}^{-3}$ and $3 \times 10^{16}\,\mathrm{cm}^{-3}$ to discriminate between bulk and surface recombination. The effective carrier lifetime of the n-type samples is analyzed at a fixed excess carrier concentration of $\Delta n = 1 \times 10^{15}\,\mathrm{cm}^{-3}$. In addition, the entire injection dependence is examined at selected points in time. The saturation current density J_0 – representing the surface passivation quality – is determined for all samples using the Kane and Swanson approach [45], explained in more detail in Section 2.4.

7.3 POLO passivation quality on fired p-type silicon

In Fig. 7.1, the lifetime evolution of 1.7 Ω cm boron-doped p-type Cz-Si samples is depicted for different Δn values to display the recombination properties at various injection conditions.

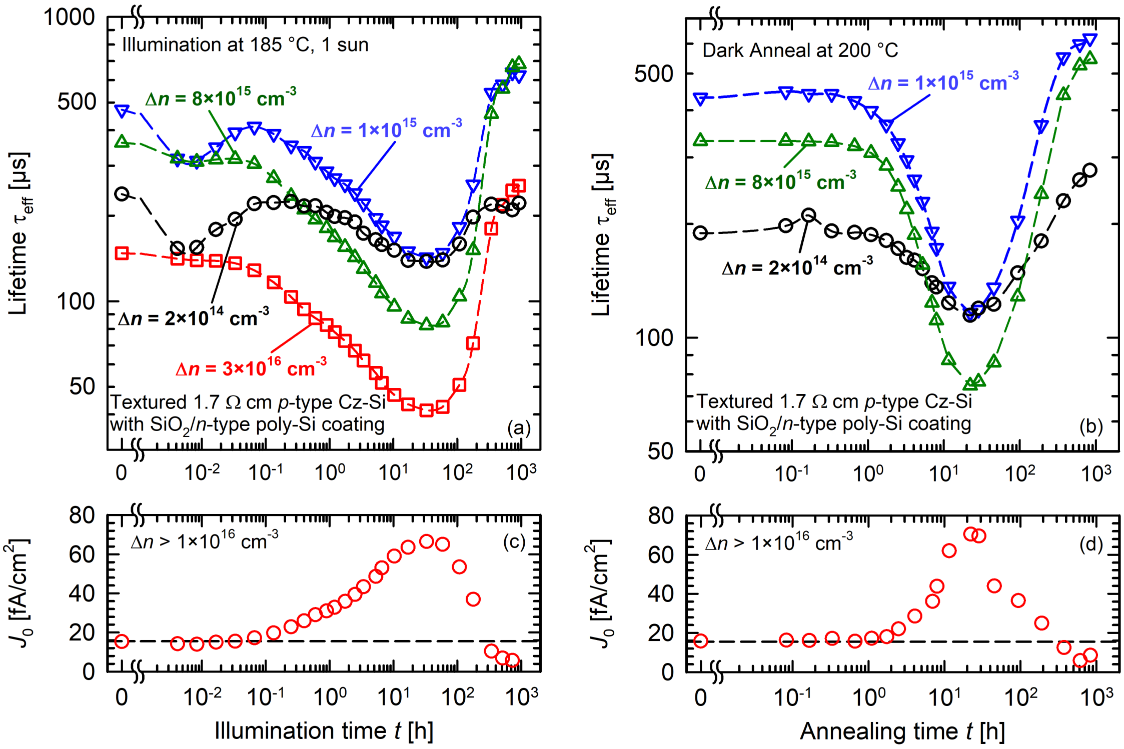

Figure 7.1: Effective carrier lifetime τ_{eff} of poly-Si-passivated p-type Cz-Si samples extracted at different excess carrier concentrations Δn shown as a function of the cumulative exposure time t to illumination or dark annealing. The sample shown in (a) is illuminated at 1 sun at 185 °C and the sample in (b) is annealed in the dark at 200 °C. The graphs (c) and (d) show the change of the saturation current density J_0, extracted from the injection-dependent lifetime at high injection densities ($\geq 10^{16}\,\mathrm{cm}^{-3}$) using the Kane and Swanson method [45]. Whereas the dashed lines in (a) and (b) serve as guide to the eye, the dashed lines in (c) and (d) represent the initial J_0 value in order to illustrate the improvement in J_0 beyond the initial state through prolonged annealing.

Fig. 7.1(a) shows the effective lifetime τ_{eff} as a function of the cumulative exposure time t to 1 sun at 185 °C. At low injection levels, two consecutive degradation and regeneration cycles can be observed on different timescales, whereas at the higher injection level of $\Delta n = 3 \times 10^{16}\,\text{cm}^{-3}$ only one degradation/regeneration cycle is observed. The initial fast degradation (visible in the low-injection curves) is completed after 0.01 h and its full regeneration after 0.1 h. This very fast degradation/regeneration cycle can be attributed to the boron-oxygen (BO) defect known from literature [9, 23, 71]. The subsequent second degradation process reaches a minimum lifetime value after ∼30 h for all injection levels. The relatively flat injection-level dependence of the lifetime in the degraded state at low injection levels (Figs. 7.1(a) and 7.1(b): degraded lifetimes at $\Delta n = 2 \times 10^{14}\,\text{cm}^{-3}$ and $\Delta n = 1 \times 10^{15}\,\text{cm}^{-3}$ are almost identical) and the fact that at high injection levels the degradation is most pronounced points toward a degradation in the surface passivation quality. This is supported by the evolution of the saturation current density J_0 which increases by a factor of ∼4.4, as shown in the Figures 7.1(c) and 7.1(d). J_0 was extracted at injection densities larger than $1 \times 10^{16}\,\text{cm}^{-3}$. Continuing the illumination at 185 °C (Fig. 7.1(a)) leads to a complete regeneration of the surface passivation, saturating at significantly lower J_0 values than in the initial state. In Fig. 7.1(b), τ_{eff} is shown for a sample after annealing at 200 °C in the dark. The initial lifetime degradation/regeneration associated with the BO bulk defect is not observed in the dark annealing experiment, which is consistent with the well-known fact that the BO defect activation needs electron injection (e.g., by illumination). Interestingly, the second degradation and regeneration cycle occurs in the same way in the dark and under illumination. We thus conclude that the second surface-related degradation/regeneration cycle is a purely thermal process. From a practical point of view, our results demonstrate that a simple low-temperature anneal in the dark is sufficient to cure the fired poly-Si surface passivation and to obtain J_0 values $<10\,\text{fA/cm}^2$ after firing.

Although the results of only one experiment are shown here, similar p-type silicon wafers were exposed to higher firing temperatures (up to 880 °C set-peak temperature) and/or other furnace belt speeds (4 m/min to 7 m/min) and show comparable results. Furthermore, the surface-related degradation/regeneration of POLO passivated silicon after firing occurs independent of the base material on 1.0 Ω cm gallium-doped Cz-Si and 2.8 Ω cm boron-doped FZ-Si as well. The use of thermally- instead of wet-chemically-grown silicon oxide also results in comparable degradation with J_0 increasing by a factor as high as 6.

A surface-related degradation/regeneration effect is also observed on the examined 5.0 Ω cm phosphorus-doped n-type Cz-Si material. The J_0 values extracted at $\Delta n \geq 8 \times 10^{15}\,\text{cm}^{-3}$ change by a factor of ∼2.7 from $49\,\text{fA/cm}^2$ to $132\,\text{fA/cm}^2$ during degradation under 1 sun at 185 °C. Because of the significantly lower degradation and regeneration rate (by a factor of ∼6) of the surface-related effect on the examined n-type material, the experiment with the n-type Cz-Si samples was aborted and the results are not shown in this section. Instead, the effect is characterized further at higher temperatures in the Sections 7.4 and 7.5.

7.4 Impact of thermal history on POLO degradation/regeneration on p- and n-type silicon

Different types of lifetime samples of p- and n-type Cz-Si wafers were annealed in the dark at 300 °C (Fig. 7.2(a)) and illuminated afterwards at 1 sun and 80 °C (Fig. 7.2(b)) to compare the evolution of the surface passivation quality under accelerated conditions. The fired boron-doped Cz-Si sample ("p-type, RTA", black circles) is cut from the same wafer as the samples discussed in Section 7.3.

The surface-related degradation/regeneration cycle visible in Fig. 7.2(a) is clearly accelerated compared to Fig. 7.1(b) using the increased dark annealing temperature of 300 °C. In addition, the extent of the lifetime degradation is much smaller at the higher annealing temperature as is the increase in J_0 by a factor of only $\sim$1.5 (Fig. 7.2(c), black circles). The saturated level of J_0 after prolonged annealing, however, is comparable to the results obtained in Section 7.3, i.e. $<$10 fA/cm^2.

A similar, most likely surface-related effect can be observed on phosphorus-doped n-type Cz-Si samples fired at the same conditions as the p-type samples (Fig. 7.2(a),

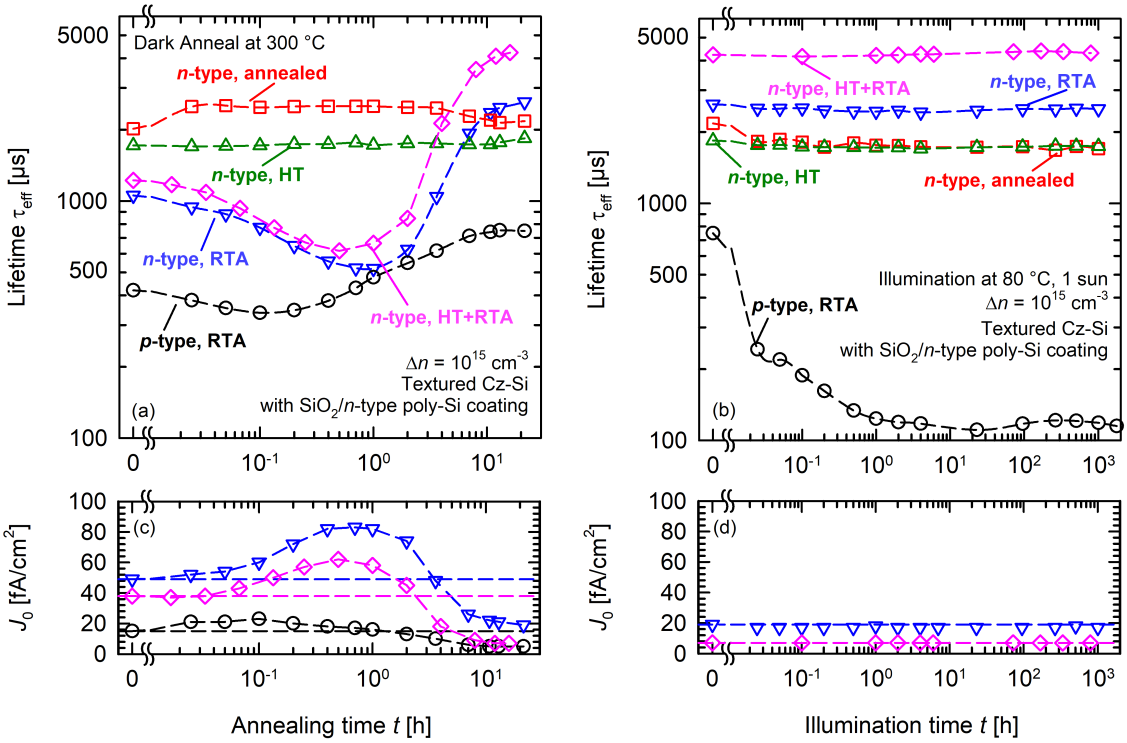

Figure 7.2: Effective carrier lifetime τ_{eff} extracted at $\Delta n = 1\times10^{15}$ cm^{-3} as a function of the cumulative exposure times t to dark annealing and illumination for p- and n-type Cz-Si samples. (a) Five lifetime samples with different thermal history annealed in the dark at 300 °C. (b) The same lifetime samples are subsequently illuminated at 1 sun and 80 °C. The dashed lines in (a) and (b) serve as guide to the eye. The graphs (c) and (d) show the simultaneous change of the saturation current densities J_0, extracted from the injection-dependent lifetime at high injection densities ($\geq 1\times10^{16}$ cm^{-3} for p-type, $\geq 8\times10^{15}$ cm^{-3} for n-type Cz-Si samples). The symbols and colors used match the corresponding graphs in (a) and (b). The dashed lines represent the initial J_0 values to illustrate (c) the improvement under prolonged annealing and (d) the stability of the surface passivation quality under illumination.

“n-type RTA”, blue inverse triangles). The saturation current density J_0 increases by a factor of ∼1.7 (Fig. 7.2(c), blue inverse triangles, extracted at $\Delta n \geq 8 \times 10^{15}\,\mathrm{cm}^{-3}$) during degradation of the lifetime within the first hour of dark annealing. After the degradation, a regeneration of the lifetime to a level higher than the initial value is visible in Fig. 7.2(a). At 300 °C, the regeneration takes ∼20 h and the saturated J_0 value after regeneration amounts to $19\,\mathrm{fA/cm^2}$, an improvement by a factor of ∼2.5 compared to the initial state. Since the thermally activated surface-related effect is not only accelerated but also considerably reduced in its extent at higher annealing temperatures for both p- and n-type silicon samples, the observed surface-related degradation and regeneration are parallel processes.

The same experiment is conducted for similar n-type silicon samples with different thermal histories. Whereas one sample in Fig. 7.2(a) received the high-temperature step at 900 °C for 30 min (“n-type, HT”, green triangles), which is commonly used to crystallize the deposited a-Si layers to poly-Si layers [154], another sample was only annealed at 425 °C for 15 min without any further annealing step (“n-type, annealed”, red squares). Neither of the two samples shows a degradation of the lifetime as observed for the fired samples. Please note, however, that for the HT sample a slight improvement in J_0 from $25\,\mathrm{fA/cm^2}$ to $21\,\mathrm{fA/cm^2}$ is observed, whereas J_0 for the annealed sample remains stable at $13\,\mathrm{fA/cm^2}$ (both not shown in Fig. 7.2). Finally, the last sample shown in Fig. 7.2(a) received both an HT treatment and a subsequent RTA step (“n-type, HT+RTA”, pink diamonds). The same degradation of the surface passivation quality as for all other fired samples is visible. The saturation current density increases by a factor of ∼1.9 (Fig. 7.2(c), pink diamonds). The subsequent regeneration results in a significantly higher lifetime caused by an improvement of the surface passivation quality by a factor of more than 5 to $J_0 = 7\,\mathrm{fA/cm^2}$ compared to the initial state after firing. The RTA and the HT+RTA samples show a very similar behavior of the surface-related degradation effect. Note, however, that for the RTA sample the ‘poly-Si’ layer is mostly in its amorphous state because the thermal budget is not sufficient to fully crystallize the a-Si layer during the ultra-fast thermal step. Therefore, since the structure of the poly-Si is very different for both samples, we assume that hydrogen passivation of the dangling bonds at the Si-SiO$_y$ interface is responsible for the observed interface-related effects. There have been similar reports by Sperber et al. for dielectric passivation layers [30] and by Yang et al. for poly-Si passivation layers [151].

A subsequent illumination of all samples at 1 sun and 80 °C serves to test the stability of the surface passivation quality. The results are shown in Fig. 7.2(b). The lifetime values of the n-type samples remain fully stable up to the maximum applied illumination time of around 1000 h (as do the corresponding J_0 values, see Fig. 7.2(d)). The p-type Cz-Si sample, however, degrades in agreement with the bulk-related activation of the BO defect. The J_0 value after completion of the experiment is $7\,\mathrm{fA/cm^2}$. Please note that no subsequent regeneration of the lifetime is observed within the duration of the experiment (almost 2000 h at 80 °C) as would have been expected for samples without prolonged annealing in the dark beforehand (analogously to the fast initial degradation/regeneration cycle in Fig. 7.1(a)). However, we were able to deactivate the BO defect again by dark annealing at 200 °C for 10 min [6, 155]. The injection dependent lifetime afterwards is virtually identical to the lifetime measured before illumination. We conclude that the surface-related improvement is not affected by the additional dark anneal.

7.5 Effect of increased dark annealing temperature

The surface passivation quality improves for fired p- and n-type Cz-Si samples and so does the lifetime over a broad injection range under prolonged annealing at elevated temperatures. Furthermore, the surface passivation depends on the thermal history of the sample, as we have shown in Section 7.4. To examine the improvement of the surface passivation quality in more detail, the dark annealing temperature was increased to 400 °C. The measured lifetime evolutions are shown in Fig. 7.3(a).
The surface-related degradation discussed in Sections 7.3 and 7.4 is not visible anymore at the higher annealing temperature of 400 °C. The focus of this experiment, however, is on the improvement of the surface passivation quality. Indeed, we observe an increase of the lifetime, for some samples (RTA and HT) even beyond the level already observed in Section 7.4. There is also a significant improvement visible for the HT-sample (green triangles), which was not observed at 300 °C annealing temperature and is possibly related to the early termination of the experiment. The increasing lifetime during annealing can be attributed to a further improvement

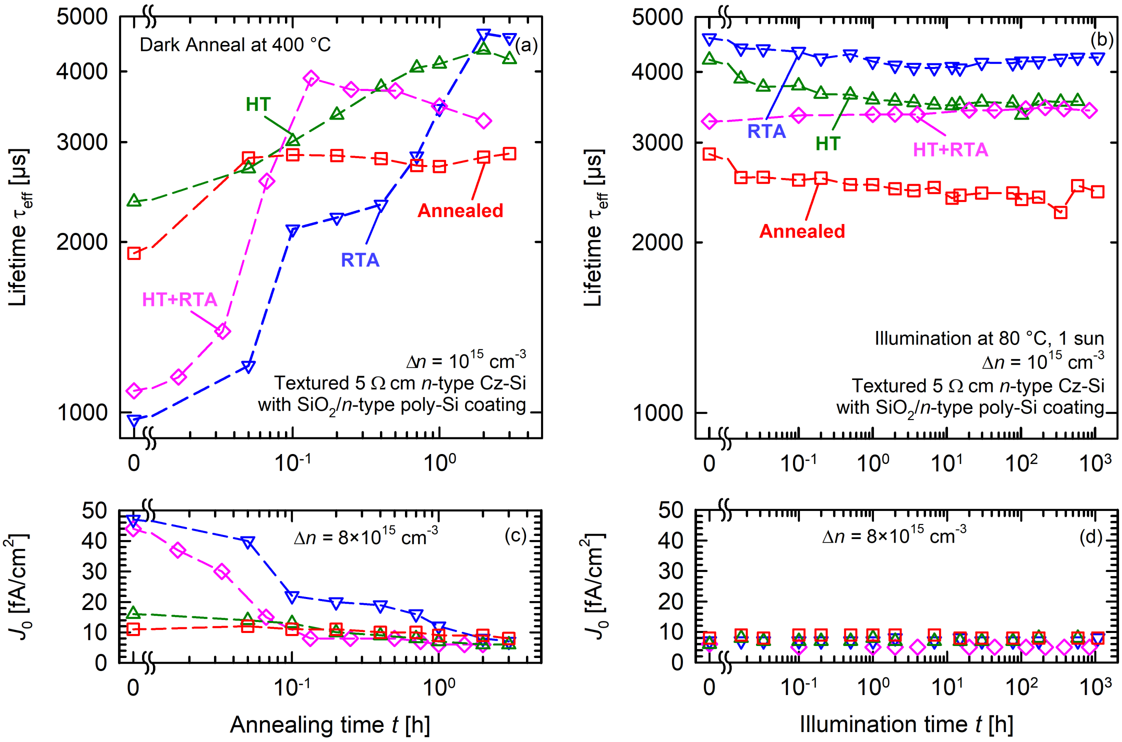

Figure 7.3: Effective carrier lifetime τ_{eff} extracted at $\Delta n = 1\times10^{15}\,\text{cm}^{-3}$ as a function of the cumulative exposure times t to dark annealing and illumination. (a) Four n-type lifetime samples with different thermal history are annealed in the dark at 400 °C. (b) The same lifetime samples are subsequently illuminated at 1 sun and 80 °C. The graphs (c) and (d) show the simultaneous change of the saturation current density J_0, extracted from the injection-dependent lifetime at high injection densities ($8\times10^{15}\,\text{cm}^{-3}$). The symbols and colors used match the corresponding graphs in (a) and (b). The dashed lines serve as guide to the eye.

of the surface passivation quality probably due to a further hydrogenation of the Si-SiO$_y$ interface. This is represented by an additional reduction of the saturation current density J_0 by a factor of $\sim$2 compared to Section 7.4. For all examined samples, J_0 values in the range between 5 and 8 fA/cm^2 are obtained. However, neither the fast improvement of the annealed sample after 3 min at 400 °C (Fig. 7.3(a), red squares) nor the small reduction in lifetime of the HT+RTA sample after 10 min at 400 °C (Fig. 7.3(a), pink diamonds) can be attributed to a change of the surface passivation quality, as shown in Fig. 7.3(c). The cause for these two effects is rather to be found at low injection levels and will be discussed in Fig. 7.4.

The subsequent illumination at 80 °C shown in Fig. 7.3(b) reveals for most samples a decrease in lifetime at $\Delta n = 10^{15}\,\text{cm}^{-3}$. Nevertheless, the lifetime remains stable at a higher level than obtained in Section 7.4 without any change in the corresponding J_0 values (Fig. 7.3(d)).

Fig. 7.4 shows the injection dependent effective lifetimes of the four n-type samples shown in Fig. 7.3. For each sample, the initial lifetime after respective processing (black circles), the highest lifetime (measured at $\Delta n = 10^{15}\,\text{cm}^{-3}$) after annealing in the dark at 400 °C (blue inverse triangles), and the lifetime after illumination at 80 °C and 1 sun for up to 1000 h (red squares) are shown.

A lifetime improvement over the entire examined injection range is clearly visible for all samples. The lifetime changes of the sample annealed during processing (Fig. 7.4(b)) might be explained by an additional iron-gettering effect [142, 156, 157]. The improvement of the fired (RTA, Fig. 7.4(a)), the high-temperature-annealed (HT, Fig. 7.4(c)), and the sample which received both the HT- and the RTA treatment (Fig. 7.4(d)) can only be understood by a significant improvement of the surface passivation quality. The degradation of the effective lifetime of the HT+RTA sample after 10 min at 400 °C (Fig. 7.3(a), pink diamonds) is only present at low injection levels. The lifetime at higher injection levels (and consequently J_0) improves further, as seen in comparison of the blue inverse triangles with the red squares in Fig. 7.4(d). The slight decrease of the lifetime for almost all samples (Fig. 7.3(b)) under long-term illumination at 80 °C is mainly limited to the low injection levels (compare Fig. 7.4, red squares), which indicates some instabilities in the bulk lifetime of our samples. The high-injection lifetimes and the corresponding J_0 values remain unchanged, i.e. the surface passivation quality has reached a stable level.

The improvement of the surface passivation quality can be achieved under illumination at the same temperature as it was observed during dark annealing, resulting in the same characteristics as described in this section.

7.6 Conclusions

In this chapter, we performed a series of carrier lifetime experiments after annealing at elevated temperatures under illumination and in the dark to examine possible instabilities of the silicon bulk as well as of the surface passivation quality. Our samples were symmetrically processed random-pyramid-textured p- and n-type Cz-Si samples passivated by n^+ poly-Si on interfacial silicon oxide layers. We observed a lifetime instability on all examined samples after an industrial-type firing step, which we attribute to a degradation of the surface passivation quality. The saturation current density J_0 of 1.7 Ω cm POLO-passivated p-type Cz-Si increased by a

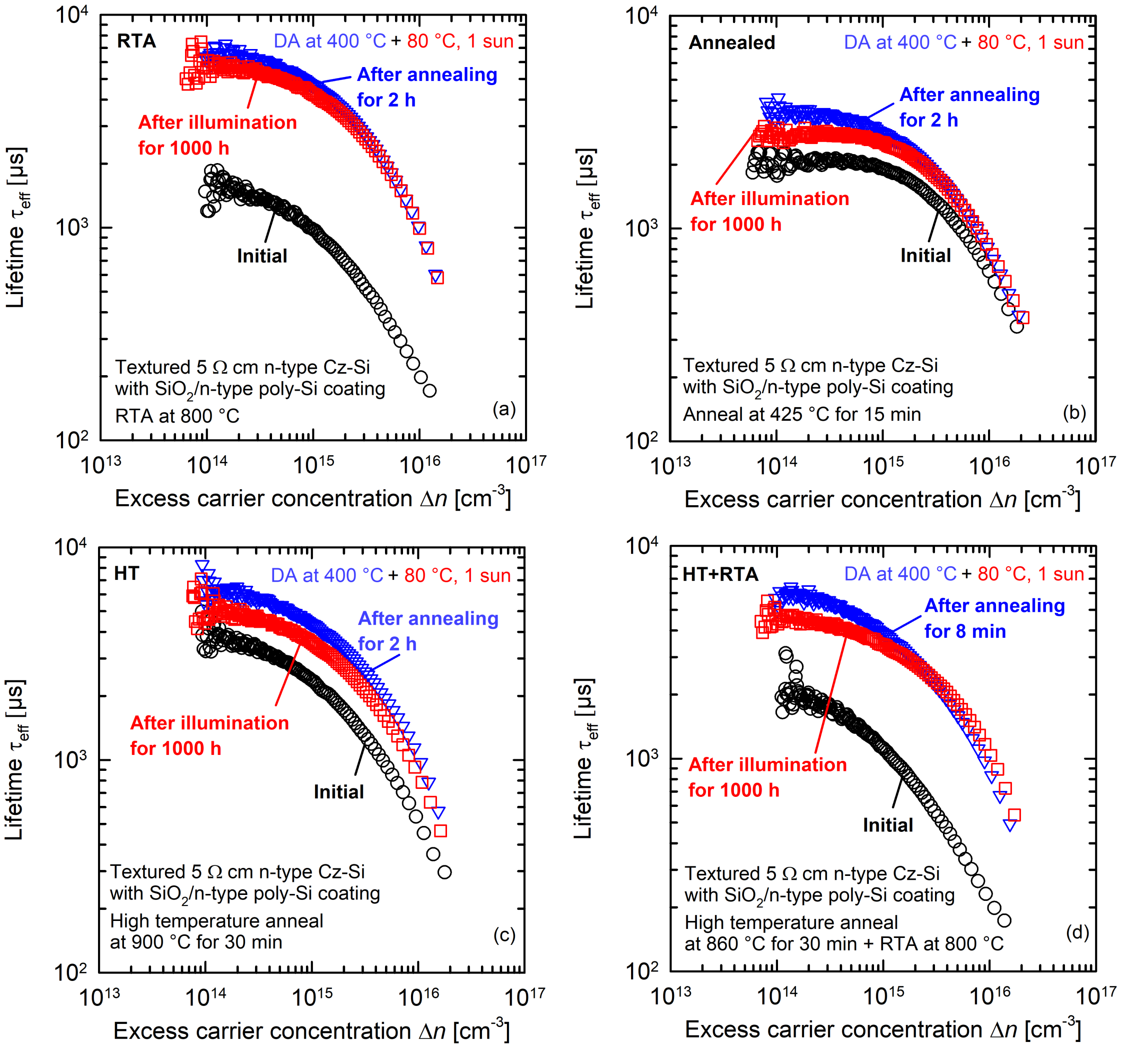

Figure 7.4: Injection dependent effective lifetime $\tau_{\text{eff}}(\Delta n)$ for the four n-type samples shown in Fig. 7.3. Each sample has a different defining step during processing: (a) RTA at 800 °C, (b) Anneal at 425 °C for 15 min, (c) HT anneal at 900 °C for 30 min, (d) HT anneal at 860 °C for 30 min followed by an RTA treatment at 800 °C. The initial lifetime (black cycles) represents the state of the samples after processing. Afterwards, the samples are annealed in the dark at 400 °C for up to several hours. The injection dependent lifetime with the highest value measured at $\Delta n = 1 \times 10^{15}\,\text{cm}^{-3}$ in Fig. 7.3(a) is shown in each case (blue inverse triangles). The red squares represent the state of the samples after illumination at 80 °C and 1 sun for up to 1000 h.

factor of ~4.4 under annealing for 30 h at temperatures around 185 °C. Under the same condition, the J_0 value of 5.0 Ω cm n-type Cz-Si increased by a factor of ~2.7 within 200 h. The degradation was followed by a regeneration of the lifetime to a level beyond the initial state under prolonged annealing for ~1000 h. Please note that we do not expect a change of the junction resistivity by our post-processing annealing treatments because the temperatures are too low to change the crystal structure of our poly-Si layers or to increase the in-diffusion of dopant atoms from the poly-Si layer into the crystalline silicon. We can also exclude an additional growth of the interfacial oxide layer as we do not expect further oxygen diffusion to the interface nor that the RTA is sufficient for an additional oxide growth beyond the already existing ∼1.6 nm SiO_y layers. Therefore, though we did not measure it, we expect the junction resistivity to be as low as previously published [27].

As the non-fired poly-Si layers show a good stability during annealing, the origin for the instability in the surface passivation quality for both p- and n-type silicon samples was identified to be the firing step, which is attractive to replace the more time-consuming usual high-temperature treatment and to allow for the implementation of screen-printed and fired contacts. The standard prolonged high-temperature treatment is performed much closer to a thermal equilibrium situation than a conveyor-belt furnace process, where in particular the cooling is very fast. Therefore, the hydrogen passivation of the dangling bonds is most likely in a different configuration after RTA than after a conventional high-temperature process. Through prolonged annealing after firing, the configuration of the hydrogen passivation at the Si-SiO_y interface changes further, which results first in a degradation and subsequently in an improvement of the surface passivation quality. We showed that a degradation of the surface passivation quality can also be observed on samples which received both the HT- and the RTA-treatment. The fact that the structure of the poly-Si is very different for RTA (mostly a-Si) and HT+RTA (a-Si crystallized to poly-Si during HT step) samples supports the supposed localization of the surface degradation/regeneration at the Si-SiO_y interface.

Although we have examined the firing-triggered surface degradation/regeneration in this chapter at relatively high temperatures $\geq$185 °C, the degradation is observable at low treatment temperatures of 80 °C as well, with a correspondingly low degradation rate constant. The J_0 value of POLO-passivated 1.7 Ω cm p-type Cz-Si increases by a factor of 4 during an anneal at 80 °C for 1000 h.

We measured a significant improvement of the surface passivation quality manifesting itself under prolonged annealing for 3 h at increased temperatures around 400 °C for all examined samples which received either HT or RTA treatments. Saturation current densities J_0 between 5 and 8 fA are obtained on textured surfaces, which amounts to an improvement through annealing by up to a factor of 6 for the fired samples in particular.

8 Summary and outlook

In this thesis, we have examined different carrier lifetime instabilities in crystalline silicon wafers that are triggered by fast-firing in a conveyor belt furnace. The fast-firing process is used to form screen-printed and fired contacts on the front and rear side of industrially produced silicon solar cells. We have examined lifetime instabilities in the bulk of boron- and gallium-doped monocrystalline silicon solar cell materials. Through variations of processing parameters and by exposing the lifetime samples to different experimental conditions (i.e., illumination intensities and temperatures during illumination), we were able to identify critical parameters which affect the extent of bulk lifetime degradation. Hydrogen, which diffuses during the fast-firing process from hydrogen-rich silicon nitride passivation layers (SiN_y:H) into the silicon bulk, is identified as a key participant in the defect formation of the observed "light- and elevated-temperature-induced degradation" (LeTID) effect. In addition, we have examined the impact of LeTID on the solar cell performance of poly-Si on oxide (POLO) backjunction (BJ) solar cells fabricated on gallium-doped Czochralski-grown silicon (Cz-Si:Ga). We were among the first to observe thermally-induced degradation of the surface passivation of phosphorus-doped POLO passivation layers after fast-firing.

On boron-doped Czochralski-grown silicon (Cz-Si:B) that has been fired in a standard conveyor belt furnace, we showed that the lifetime under illumination is dominated by the activation of the well-known boron-oxygen (BO) defect. The impact of LeTID was found to increase, if the amount of hydrogen in Cz-Si:B is increased by coating the wafers with very silicon-rich SiN_y layers (refractive index n of 2.4) instead of applying SiN_y layers with the standard stoichiometry of refractive index $n = 2.05$. We determined capture time constant ratios Q outside the margin reported for the BO defect in the literature (~ 10), which indicates the increasing impact of the LeTID defect with a higher Q value (~ 23).
We introduced a method to separate the BO and the LeTID defect formation in Cz-Si:B through BO defect activation/deactivation cycles by alternating an illumination and a dark annealing (DA) step. Comparing lifetime measurements on non-fired and fired lifetime samples, we were able to show that, besides the BO LID, a second degradation effect is indeed occurring in the bulk of fired Cz-Si:B samples, although the BO LID remains dominant. The LeTID effect occurs not only at elevated temperatures (80 °C, 1 sun), but is even more pronounced at low temperatures (30 °C) and low illumination intensities (0.1 suns). The LeTID effect on mc-Si:B, however, seems to be temporarily deactivated by illumination at low temperatures near room temperature [20, 91]. Furthermore, the time constants (the inverse of the degradation rate constant R_{deg}) of LeTID in Cz-Si:B and mc-Si:B differ by a factor of ~4 with LeTID in mc-Si:B being the slower process. We showed that the LeTID effect in mc-Si:B, unlike in Cz-Si:B, is strongly influenced by the

DA steps, as has also been reported by Fung et al. [19], who attributed the increasing of the LeTID-limited lifetime with repeating DA and illumination cycles to a hydrogen-reservoir state. We observed no such behavior on our Cz-Si:B samples. Nevertheless, since the LeTID effects on both mc-Si:B and Cz-Si:B are clearly triggered by fast-firing, it is most likely that both degradation effects are hydrogen-related, however, the detailed defect physics seem to be different.

On both gallium-doped Cz-Si (Cz-Si:Ga) and boron-doped float-zone silicon (FZ-Si:B) wafers we observed a strongly temperature-dependent degradation of the bulk lifetime under illumination. The trigger for degradation to occur in both materials is the fast-firing step. The equilibrium state establishing itself between activated (recombination-active) and deactivated (recombination-inactive) states of the defect is dependent on the temperature and the activation and deactivation are reversible processes. Although the time constants of these LeTID effects in Cz-Si:Ga and FZ-Si:B differ by at least a factor of 10 from LeTID in mc-Si:B, a temporary deactivation by illumination at low temperatures near room temperature has been reported before on mc-Si:B [20, 91] and FZ-Si:B [19]. We were the first to observe a pronounced temperature dependence of LeTID on Cz-Si:Ga wafers and the first to systematically examine the impact of the temperature over a large range between ∼44 and 160 °C on both Cz-Si:Ga and FZ-Si:B.
We identified hydrogen as a participant in the LeTID defect reaction in Cz-Si:Ga. The peak firing temperature FT and the band velocity v_{band} (related to the cooling ramp after the firing peak) of the fast-firing process, and the composition of the SiN_y layers deposited prior to fast-firing are key parameters that determine the amount of hydrogen available for defect reactions in the bulk of the silicon. We have shown conclusively throughout this thesis that the LeTID extent in Cz-Si:Ga increases with FT, v_{band}, and the refractive index of SiN_y layers on the wafer surfaces, as does the hydrogen content. These results are in agreement with the literature on LeTID in mc-Si:B and FZ-Si:B. However, we observe no increase of LeTID with increasing refractive index n of the SiN_y layers on our reference FZ-Si:B samples. Furthermore, the maximum effective defect concentration N^*_{max} is in general one order of magnitude smaller in the defect-lean FZ-Si:B than on identically processed Cz-Si:Ga. Both results support the hypothesis of a second participant in the defect reaction of LeTID besides hydrogen.
We were the first to state an (apparent) activation energy E_{A} of the LeTID effect in Cz-Si:Ga of $(0.55 \pm 0.10)\,\mathrm{eV}$, which is significantly lower compared to the E_{A} value reported for LeTID in mc-Si:B (∼1 eV). It does, however, coincide with the E_{A} value determined on our reference FZ-Si:B wafers.
We observed no significant impact of the illumination intensity on N^*_{max} between 0.1 suns and 1 sun. A partial permanent deactivation can be achieved by applying prolonged illumination at elevated temperatures (135 °C) and light intensities around 1 sun.

We were able to show that the temperature-dependent LeTID effect examined in detail on Cz-Si:Ga lifetime samples is also the cause of observed degradation of POLO BJ solar cells fabricated on Cz-Si:Ga. Under one-sun illumination at elevated temperatures between 80 °C and 140 °C, the degradation extent of the energy

conversion efficiency η was found to increase from 0.15%$_{\mathrm{abs}}$ to 0.4%$_{\mathrm{abs}}$, which corresponds to a maximum relative degradation extent of 2%$_{\mathrm{rel}}$ at 140 °C and 1 sun. At the typical operation temperatures, POLO BJ cells are remarkably stable regarding light-induced degradation, which we have demonstrated through long-term illumination at 80 °C for 1400 h. The LeTID effect observed in our POLO BJ cells can be ascribed mainly to losses in short-circuit current density J_{sc} and fill factor FF. We conclude that the J_{sc} and FF losses are caused by the injection dependence of the lifetime of the activated bulk defect in conjunction with the structure of a BJ solar cell, collecting minority carriers at the rear side. The open-circuit voltage V_{oc}, however, shows mainly scattering, which we attribute to the almost non-existent LeTID at the relatively high excess carrier concentrations Δn at V_{oc}.
Through prolonged illumination at elevated temperatures (1 sun, 140 °C) an improvement of the energy conversion efficiency by up to 0.2%$_{\mathrm{abs}}$ and a partial permanent deactivation of the LeTID defect are possible.

In addition to bulk degradation, we discovered thermally-induced instabilities of the phosphorus-doped POLO passivation layers after fast-firing. At temperatures of around 200 °C, a degradation of the saturation current density J_0 followed by a regeneration to a level lower than after firing is observable, both under illumination and in the dark. As non-fired poly-Si on oxide layers show a very good stability at low J_0 values, the trigger of the surface-related degradation is the fast-firing step. Due to the fact that the structure of the POLO passivation has no impact on the degradation behavior, we were able to attribute the surface degradation and regeneration with high probability to the hydrogen passivation of states at the Si-SiO$_2$ interface.
With increasing treatment temperature after firing (i.e., >200 °C) the degradation extent decreases and vanishes at treatment temperatures of around 400 °C. Degradation and improvement of the surface passivation quality are parallel processes, which strongly dependent on the treatment temperature after firing.

Looking ahead, to identify the second participant of the LeTID defect reaction a targeted contamination of Cz-Si:Ga wafers with eligible metallic impurities would be a promising objective. To examine the electronic properties of LeTID, a systematic variation of the doping and hence the hole concentration in the material could be a worthwhile approach, as could be the examination of LeTID in n-type silicon materials.
But most importantly, since Cz-Si:Ga and solar cells made thereof seem to be remarkably stable against LeTID under standard operation temperatures (<80 °C), the long-term stability of solar cells and hence PV modules requires a more detailed examination of degradation of surface passivation layers (POLO and dielectric passivation layers), especially on textured surfaces, and their impact on solar cell performance.

Bibliography

[1] International Energy Agency, "World Energy Outlook 2023," 2023.

[2] ——, "Renewables 2022: Analysis and forecast to 2027," 2022.

[3] G. M. Wilson, M. Al-Jassim, W. K. Metzger, S. W. Glunz, P. Verlinden, G. Xiong, L. M. Mansfield, B. J. Stanbery, K. Zhu, Y. Yan, J. J. Berry, A. J. Ptak, F. Dimroth, B. M. Kayes, A. C. Tamboli, R. Peibst, K. Catchpole, M. O. Reese, C. S. Klinga, P. Denholm, M. Morjaria, M. G. Deceglie, J. M. Freeman, M. A. Mikofski, D. C. Jordan, G. TamizhMani, and D. B. Sulas-Kern, "The 2020 photovoltaic technologies roadmap," *Journal of Physics D: Applied Physics*, vol. 53, no. 49, p. 493001, 2020. [Online]. Available: http://dx.doi.org/10.1088/1361-6463/ab9c6a

[4] L. J. Geerligs and D. Macdonald, "Dynamics of light-induced FeB pair dissociation in crystalline silicon," *Applied Physics Letters*, vol. 85, no. 22, pp. 5227–5229, 2004.

[5] J. Schmidt, "Effect of dissociation of iron-boron pairs in crystalline silicon on solar cell properties," *Progress in Photovoltaics: Research and Applications*, vol. 13, no. 4, pp. 325–331, 2005.

[6] J. Schmidt, A. G. Aberle, and R. Hezel, "Investigation of Carrier Lifetime Instabilities In CZ Grown Silicon," *Conference Record of the Twenty Sixth IEEE Photovoltaic Specialists Conference, Anaheim, CA, USA*, pp. 13–18, 1997.

[7] S. W. Glunz, S. Rein, W. Warta, J. Knobloch, and W. Wettling, "On the degradation of Cz-silicon solar cells," *Proceedings of the 2nd World Conference on Photovoltaic Solar Energy Conversion, Vienna, Austria*, pp. 1343–1346, 1998.

[8] J. Schmidt and K. Bothe, "Structure and transformation of the metastable boron- and oxygen-related defect center in crystalline silicon," *Physical Review B*, vol. 69, no. 2, p. 024107, 2004.

[9] K. Bothe and J. Schmidt, "Electronically activated boron-oxygen-related recombination centers in crystalline silicon," *Journal of Applied Physics*, vol. 99, no. 1, p. 013701, 2006.

[10] K. Ramspeck, S. Zimmermann, H. Nagel, A. Metz, Y. Gassenbauer, B. Birkmann, and A. Seidl, "Light Induced Degradation of Rear Passivated mc-Si Solar Cells," *Proceedings of the 27th EU PVSEC, Frankfurt, Germany*, pp. 861–865, 2012.

[11] K. Krauss, F. Fertig, D. Menzel, and S. Rein, "Light-induced Degradation of Silicon Solar Cells with Aluminiumoxide Passivated Rear Side," *Energy Procedia*, vol. 77, pp. 599–606, 2015.

[12] F. Kersten, P. Engelhart, H.-C. Ploigt, A. Stekolnikov, T. Lindner, F. Stenzel, M. Bartzsch, A. Szpeth, K. Petter, J. Heitmann, and J. W. Müller, "Degradation of multicrystalline silicon solar cells and modules after illumination at elevated temperature," *Solar Energy Materials and Solar Cells*, vol. 142, pp. 83–86, 2015.

[13] D. Bredemeier, D. Walter, S. Herlufsen, and J. Schmidt, "Lifetime degradation and regeneration in multicrystalline silicon under illumination at elevated temperature," *AIP Advances*, vol. 6, no. 3, p. 035119, 2016.

[14] K. Nakayashiki, J. Hofstetter, A. E. Morishige, T.-T. A. Li, D. B. Needleman, M. A. Jensen, and T. Buonassisi, "Engineering Solutions and Root-Cause Analysis for Light-Induced Degradation in p-Type Multicrystalline Silicon PERC Modules," *IEEE Journal of Photovoltaics*, vol. 6, no. 4, pp. 860–868, 2016.

[15] F. Fertig, R. Lantzsch, A. Mohr, M. Schaper, M. Bartzsch, D. Wissen, F. Kersten, A. Mette, S. Peters, A. Eidner, J. Cieslak, K. Duncker, M. Junghänel, E. Jarzembowski, M. Kauert, B. Faulwetter-Quandt, D. Meißner, B. Reiche, S. Geißler, S. Hörnlein, C. Klenke, L. Niebergall, A. Schönmann, A. Weihrauch, F. Stenzel, A. Hofmann, T. Rudolph, A. Schwabedissen, M. Gundermann, M. Fischer, J. W. Müller, and D. Jeong, "Mass production of p -type Cz silicon solar cells approaching average stable conversion efficiencies of 22 %," *Energy Procedia*, vol. 124, pp. 338–345, 2017.

[16] D. Chen, M. Kim, B. V. Stefani, B. J. Hallam, M. D. Abbott, C. E. Chan, R. Chen, D. N. Payne, N. Nampalli, A. Ciesla, T. H. Fung, K. Kim, and S. R. Wenham, "Evidence of an identical firing-activated carrier-induced defect in monocrystalline and multicrystalline silicon," *Solar Energy Materials and Solar Cells*, vol. 172, pp. 293–300, 2017.

[17] D. Sperber, A. Herguth, and G. Hahn, "A 3-state defect model for light-induced degradation in boron-doped float-zone silicon," *physica status solidi (RRL) - Rapid Research Letters*, vol. 11, no. 3, p. 1600408, 2017.

[18] T. Niewelt, M. Selinger, N. E. Grant, W. Kwapil, J. D. Murphy, and M. C. Schubert, "Light-induced activation and deactivation of bulk defects in boron-doped float-zone silicon - 1.4983024," *Journal of Applied Physics*, vol. 121, p. 185702, 2017.

[19] T. Niewelt, F. Schindler, W. Kwapil, R. Eberle, J. Schön, and M. C. Schubert, "Understanding the light-induced degradation at elevated temperatures: Similarities between multicrystalline and floatzone p-type silicon," *Progress in Photovoltaics: Research and Applications*, vol. 26, no. 8, pp. 533–542, 2018.

[20] F. Kersten, P. Engelhart, H.-C. Ploigt, F. Stenzel, K. Petter, T. Lindner, A. Szpeth, M. Bartzsch, A. Stekolnikov, M. Scherff, J. Heitmann, and J. W.

Müller, “A new light induced volume degradation effect of mc-Si solar cells and modules,” *Proceedings of the 31th European Photovoltaic Solar Energy Conference and Exhibition, Hamburg, Germany*, pp. 1830–1834, 2015.

[21] VDMA, “International Technology Roadmap for Photovoltaics (ITRPV), 8th Edition,” 2017.

[22] ——, “International Technology Roadmap for Photovoltaics (ITRPV), 14th Edition,” 2023.

[23] J. Schmidt, “Light-Induced Degradation in Crystalline Silicon Solar Cells,” *Solid State Phenomena*, vol. 95-96, pp. 187–196, 2004.

[24] J. Y. Gan and R. M. Swanson, “Polysilicon emitters for silicon concentrator solar cells,” in *IEEE Conference on Photovoltaic Specialists.* IEEE, 21-25 May 1990, pp. 245–250.

[25] U. Römer, R. Peibst, T. Ohrdes, B. Lim, J. Krügener, T. Wietler, and R. Brendel, “Ion Implantation for Poly-Si Passivated Back-Junction Back-Contacted Solar Cells,” *IEEE Journal of Photovoltaics*, vol. 5, no. 2, pp. 507–514, 2015.

[26] R. Peibst, Y. Larionova, S. Reiter, M. Turcu, R. Brendel, D. Tetzlaff, J. Krügener, T. Wietler, U. Höhne, J.-D. Kähler, H. Mehlich, and S. Frigge, “Implementation of n+ and p+ Poly Junctions on Front and Rear Side of Double-Side Contacted Industrial Silicon Solar Cells: 5 pages / 32nd European Photovoltaic Solar Energy Conference and Exhibition; 323-327,” *Proceedings of the 32th European Photovoltaic Solar Energy Conference and Exhibition, Munich, Germany*, 2016.

[27] M. Rienacker, M. Bossmeyer, A. Merkle, U. Römer, F. Haase, J. Krügener, R. Brendel, and R. Peibst, “Junction Resistivity of Carrier-Selective Polysilicon on Oxide Junctions and Its Impact on Solar Cell Performance,” *IEEE Journal of Photovoltaics*, vol. 7, no. 1, pp. 11–18, 2017.

[28] B. Veith, F. Werner, D. Zielke, R. Brendel, and J. Schmidt, “Comparison of the thermal stability of single Al2O3 layers and Al2O3/SiNx stacks for the surface passiviation of silicon,” *Energy Procedia*, vol. 8, pp. 307–312, 2011.

[29] D. Sperber, A. Herguth, and G. Hahn, “Instability of Dielectric Surface Passivation Quality at Elevated Temperature and Illumination,” *Energy Procedia*, vol. 92, pp. 211–217, 2016.

[30] D. Sperber, A. Graf, D. Skorka, A. Herguth, and G. Hahn, “Degradation of Surface Passivation on Crystalline Silicon and Its Impact on Light-Induced Degradation Experiments,” *IEEE Journal of Photovoltaics*, vol. 7, no. 6, pp. 1627–1634, 2017.

[31] D. Sperber, A. Heilemann, A. Herguth, and G. Hahn, “Temperature and Light-Induced Changes in Bulk and Passivation Quality of Boron-Doped Float-Zone Silicon Coated With SiNx:H,” *IEEE Journal of Photovoltaics*, vol. 7, no. 2, pp. 463–470, 2017.

[32] T. Trupke, M. A. Green, P. Würfel, P. P. Altermatt, A. Wang, J. Zhao, and R. Corkish, "Temperature dependence of the radiative recombination coefficient of intrinsic crystalline silicon," *Journal of Applied Physics*, vol. 94, no. 8, p. 4930, 2003.

[33] A. Hangleiter and R. Häcker, "Enhancement of Band-to-Band Auger Recombination by Electron-Hole Correlations," *Physical Review Letters*, vol. 65, no. 2, pp. 215–218, 1990.

[34] P. P. Altermatt, J. Schmidt, G. Heiser, and A. G. Aberle, "Assessment and parameterisation of Coulomb-enhanced Auger recombination coefficients in lowly injected crystalline silicon," *Journal of Applied Physics*, vol. 82, no. 10, pp. 4938–4944, 1997.

[35] J. Schmidt, M. Kerr, and P. P. Altermatt, "Coulomb-enhanced Auger recombination in crystalline silicon at intermediate and high-injection densities," *Journal of Applied Physics*, vol. 88, no. 3, 2000.

[36] A. Richter, S. W. Glunz, F. Werner, J. Schmidt, and A. Cuevas, "Improved quantitative description of Auger recombination in crystalline silicon," *Physical Review B*, vol. 86, no. 16, p. 187, 2012.

[37] T. Niewelt, B. Steinhauser, A. Richter, B. Veith-Wolf, A. Fell, B. Hammann, N. E. Grant, L. Black, J. Tan, A. Youssef, J. D. Murphy, J. Schmidt, M. C. Schubert, and S. W. Glunz, "Reassessment of the intrinsic bulk recombination in crystalline silicon," *Solar Energy Materials and Solar Cells*, vol. 235, no. 1, p. 111467, 2022.

[38] W. Shockley and W. T. Read, "Statistics of the recombination of holes and electrons," *Physical Review*, vol. 87, no. 5, pp. 835–842, 1952.

[39] R. N. Hall, "Electron-Hole Recombination in Germanium," *Physical Review*, vol. 87, no. 2, p. 387, 1952.

[40] J. D. Murphy, K. Bothe, R. Krain, V. V. Voronkov, and R. J. Falster, "Parameterisation of injection-dependent lifetime measurements in semiconductors in terms of Shockley-Read-Hall statistics: An application to oxide precipitates in silicon," *Journal of Applied Physics*, vol. 111, no. 11, p. 113709, 2012.

[41] J. Schmidt, B. Veith, and R. Brendel, "Effective surface passivation of crystalline silicon using ultrathin Al2O3 films and Al2O3/SiNx stacks," *Phys. Status Solidi RRL*, vol. 3, pp. 287–289, 2009.

[42] A. B. Sproul, "Dimensionless solution of the equation describing the effect of surface recombination on carrier decay in semiconductors," *Journal of Applied Physics*, vol. 76, no. 5, pp. 2851–2854, 1994.

[43] K. R. McIntosh and L. E. Black, "On effective surface recombination parameters," *Journal of Applied Physics*, vol. 116, no. 1, p. 014503, 2014.

[44] J. A. del Alamo and R. M. Swanson, "The physics and modeling of heavily doped emitters," *IEEE Transactions on Electron Devices*, vol. 31, no. 12, pp. 1878–1888, 1984.

[45] D. Kane and R. Swanson, "Measurement of the emitter saturation current by a contactless photoconductivity decay method," *18th IEEE Photovoltaic Specialists Conference*, pp. 578–583, 1985.

[46] R. A. Sinton and A. Cuevas, "Contactless determination of current–voltage characteristics and minority-carrier lifetimes in semiconductors from quasi-steady-state photoconductance data," *Applied Physics Letters*, vol. 69, no. 17, pp. 2510–2512, 1996.

[47] L. Helmich, "Improved understanding of boron-oxygen-related carrier lifetime degradation and regeneration in crystalline silicon solar cells," Ph.D. dissertation, Leibniz University, Hannover, 2022.

[48] P. P. Altermatt, J. Schmidt, M. Kerr, G. Heiser, and A. G. Aberle, "Exciton-enhanced Auger recombination in crystalline silicon under intermediate and high injection conditions," *Proceedings of the 16th EU PVSEC, Glasgow, UK*, pp. 243–246, 2000.

[49] H. Nagel, C. Berge, and A. G. Aberle, "Generalized analysis of quasi-steady-state and quasi-transient measurements of carrier lifetimes in semiconductors," *Journal of Applied Physics*, vol. 86, no. 11, p. 6218, 1999.

[50] S. Herlufsen, J. Schmidt, D. Hinken, K. Bothe, and R. Brendel, "Photoconductance-calibrated photoluminescence lifetime imaging of crystalline silicon," *physica status solidi (RRL) - Rapid Research Letters*, vol. 2, no. 6, pp. 245–247, 2008.

[51] ——, "Camera-based photoluminescence lifetime imaging of crystalline silicon wafers," *Proceedings of the 24th EUPVSEC, Hamburg, Germany*, pp. 913–917, 2009.

[52] Napson Corporation, "Four point probe resistivity/sheet resistance unit - User manual."

[53] R. Brendel, C. Kruse, A. Merkle, H. Schulte-Huxel, F. Haase, and R. Peibst, "Screening carrier selective contact combinations for novel crystalline Si cell structures," *Proceedings of the 35th EU PVSEC, Brussels, Belgium*, pp. 39–46, 2018.

[54] B. Min, N. Wehmeier, H. Schulte-Huxel, R. Witteck, T. Brendemuehl, T. Daschinger, F. Haase, Y. Larionova, L. Nasebandt, K. Tsuji, M. Dhamrin, R. Peibst, and R. Brendel, "Approaching 23% with p-type back junction solar cells featuring screen-printed Al front grid and passivating rear contacts," *Proceedings of the 38th EU PVSEC, WIP, Munich*, 2021.

[55] R. Brendel and R. Peibst, "Contact Selectivity and Efficiency in Crystalline Silicon Photovoltaics," *IEEE Journal of Photovoltaics*, vol. 6, no. 6, pp. 1413–1420, 2016.

[56] S. Reiter, N. Koper, R. Reineke-Koch, Y. Larionova, M. Turcu, J. Krügener, D. Tetzlaff, T. Wietler, U. Höhne, J.-D. Kähler, R. Brendel, and R. Peibst, “Parasitic Absorption in Polycrystalline Si-layers for Carrier-selective Front Junctions,” *Energy Procedia*, vol. 92, no. 2, pp. 199–204, 2016.

[57] B. Min, M. R. Vogt, T. Wietler, R. Reineke-Koch, B. Wolpensinger, E. Köhnen, D. Tetzlaff, C. Schinke, R. Brendel, and R. Peibst, “Increasing the photogenerated current in solar cells with passivating contacts by reducing the poly-Si deposition temperature,” *AIP Conference Proceedings*, vol. 1999, p. 040015, 2018.

[58] A. Ingenito, G. Nogay, J. Stuckelberger, P. Wyss, L. Gnocchi, C. Allebe, J. Horzel, M. Despeisse, F.-J. Haug, P. Loper, and C. Ballif, “Phosphorous-Doped Silicon Carbide as Front-Side Full-Area Passivating Contact for Double-Side Contacted c-Si Solar Cells,” *IEEE Journal of Photovoltaics*, vol. 9, no. 2, pp. 346–354, 2019.

[59] H. J. Hovel, R. K. Willardson, and A. C. Beer, *Semiconductors and semimetals.* New York: Academic Press, 1975, vol. 11.

[60] M. A. Green, *Silicon solar cells: Advanced principles & practice.* Sydney: Centre for Photovoltaic Devices and Systems Univ. of New South Wales, 1995.

[61] PV tools, “LOANA solar cell analysis system - User manual: version 02.2017,” 2017. [Online]. Available: http://www.pv-tools.de/products/loana-system/loana-start.html

[62] Y. P. Varshni, “Temperature dependence of the energy gap in semiconductors,” *Physica*, vol. 34, no. 1, pp. 149–154, 1967. [Online]. Available: https://www.sciencedirect.com/science/article/pii/0031891467900626

[63] P. Löper, D. Pysch, A. Richter, M. Hermle, S. Janz, M. Zacharias, and S. W. Glunz, “Analysis of the Temperature Dependence of the Open-Circuit Voltage,” *Energy Procedia*, vol. 27, pp. 135–142, 2012.

[64] M. A. Green, “Solar cell fill factors: General graph and empirical expressions,” *Solid State Electronics*, vol. 24, no. 8, pp. 788–789, 1981.

[65] J. Schmidt, A. Cuevas, S. Rein, and S. W. Glunz, “Impact of Light-induced Recombination Centres on the Current-Voltage Characteristic of Czochralski Silicon Solar Cells,” *Progress in Photovoltaics: Research and Applications*, vol. 9, no. 9, pp. 249–255, 2001.

[66] D. Bredemeier, D. C. Walter, and J. Schmidt, “Lifetime degradation in multicrystalline silicon under illumination at elevated temperature: Indications for the involvement of hydrogen,” *AIP Conference Proceedings, Lausanne, Switzerland*, p. 130001, 2018.

[67] A. Graf, A. Herguth, and G. Hahn, “Determination of BO-LID and LeTID Related Activation Energies in Cz-Si and FZ-Si using Constant Injection Conditions,” *AIP Conference Proceedings, Leuven, Belgium*, p. 140003, 2019.

[68] H. C. Sio, H. Wang, Q. Wang, C. Sun, W. Chen, H. Jin, and D. Macdonald, "Light and elevated temperature induced degradation in p-type and n-type cast-grown multicrystalline and mono-like silicon," *Solar Energy Materials and Solar Cells*, vol. 182, pp. 98–104, 2018.

[69] D. Chen, P. G. Hamer, M. Kim, T. H. Fung, G. Bourret-Sicotte, S. Liu, C. E. Chan, A. Ciesla, R. Chen, M. D. Abbott, B. J. Hallam, and S. R. Wenham, "Hydrogen induced degradation: A possible mechanism for light- and elevated temperature- induced degradation in n-type silicon," *Solar Energy Materials and Solar Cells*, vol. 185, pp. 174–182, 2018.

[70] C. Chan, T. H. Fung, M. Abbott, D. Payne, A. Wenham, B. Hallam, R. Chen, and S. Wenham, "Modulation of Carrier-Induced Defect Kinetics in Multi-Crystalline Silicon PERC Cells Through Dark Annealing," *Solar RRL*, vol. 1, no. 2, p. 1600028, 2017.

[71] A. Herguth, G. Schubert, M. Kaes, and G. Hahn, "A New Approach to Prevent the Negative Impact of the Metastable Defect in Boron Doped CZ Silicon Solar Cells," in *Conference record of the 2006 IEEE 4th World Conference on Photovoltaic Energy Conversion.* IEEE Operations Center, 2006, pp. 940–943.

[72] D. C. Walter, B. Lim, K. Bothe, V. V. Voronkov, R. Falster, and J. Schmidt, "Effect of rapid thermal annealing on recombination centres in boron-doped Czochralski-grown silicon," *Applied Physics Letters*, vol. 104, no. 4, p. 042111, 2014.

[73] S. Wilking, S. Ebert, A. Herguth, and G. Hahn, "Influence of short high temperature steps on the regeneration of boron-oxygen related defects," *Proceedings of the 28th European Photovoltaic Solar Energy Conference and Exhibition, Paris, France*, pp. 34–38, 2013.

[74] D. Bredemeier, D. Walter, and J. Schmidt, "Light-induced lifetime degradation in high-performance multicrystalline silicon: Detailed kinetics of the defect activation: 6th International Conference on Silicon Photovoltaics, SiliconPV 2016," *Solar Energy Materials and Solar Cells*, vol. 173, pp. 2–5, 2017.

[75] W. Kwapil, T. Niewelt, and M. C. Schubert, "Kinetics of carrier-induced degradation at elevated temperature in multicrystalline silicon solar cells," *Solar Energy Materials and Solar Cells*, vol. 173, pp. 80–84, 2017.

[76] A. Herguth, "Concepts and techniques for the analysis of defect reactions in crystalline silicon," Ph.D. dissertation, University of Konstanz, Konstanz, 2023.

[77] B. Lim, F. Rougieux, D. Macdonald, K. Bothe, and J. Schmidt, "Generation and annihilation of boron–oxygen-related recombination centers in compensated p- and n-type silicon," *Journal of Applied Physics*, vol. 108, no. 10, 2010.

[78] M. Forster, E. Fourmond, F. E. Rougieux, A. Cuevas, R. Gotoh, K. Fujiwara, S. Uda, and M. Lemiti, “Boron-oxygen defect in Czochralski-silicon co-doped with gallium and boron,” *Applied Physics Letters*, vol. 100, no. 4, 2012.

[79] P. Hamer, N. Nampalli, Z. Hameiri, M. Kim, D. Chen, N. Gorman, B. Hallam, M. Abbott, and S. Wenham, “Boron-Oxygen Defect Formation Rates and Activity at Elevated Temperatures,” *Energy Procedia*, vol. 92, no. 17, pp. 791–800, 2016.

[80] A. Graf, A. Herguth, and G. Hahn, “Investigation on the dependence of degradation rate on hole concentration during boron-oxygen related light-induced degradation in crystalline silicon,” *AIP Advances*, vol. 8, no. 8, p. 404, 2018.

[81] A. Herguth and G. Hahn, “Kinetics of the boron-oxygen related defect in theory and experiment,” *Journal of Applied Physics*, vol. 108, no. 11, 2010.

[82] V. Steckenreiter, D. C. Walter, and J. Schmidt, “Kinetics of the permanent deactivation of the boron-oxygen complex in crystalline silicon as a function of illumination intensity,” *AIP Advances*, vol. 7, no. 3, p. 404, 2017.

[83] V. V. Voronkov, R. J. Falster, J. Schmidt, K. Bothe, and A. Batunina, “(Invited) Lifetime Degradation in Boron Doped Czochralski Silicon,” *ECS Transactions*, vol. 33, no. 11, pp. 103–112, 2010.

[84] A. E. Morishige, M. A. Jensen, D. B. Needleman, K. Nakayashiki, J. Hofstetter, T.-T. A. Li, and T. Buonassisi, “Lifetime Spectroscopy Investigation of Light-Induced Degradation in p-type Multicrystalline Silicon PERC,” *IEEE Journal of Photovoltaics*, vol. 6, no. 6, pp. 1466–1472, 2016.

[85] D. Bredemeier, D. Walter, S. Herlufsen, and J. Schmidt, “Understanding the Light-induced Lifetime Degradation and Regeneration in Multicrystalline Silicon,” *Energy Procedia*, vol. 92, pp. 773–778, 2016.

[86] J. Schmidt and A. Cuevas, “Electronic properties of light-induced recombination centers in boron-doped Czochralski silicon,” *Journal of Applied Physics*, vol. 86, no. 6, pp. 3175–3180, 1999.

[87] S. Rein and S. W. Glunz, “Electronic properties of the metastable defect in boron-doped Czochralski silicon: Unambiguous determination by advanced lifetime spectroscopy,” *Applied Physics Letters*, vol. 82, no. 7, pp. 1054–1056, 2003.

[88] D. Bredemeier, D. C. Walter, R. Heller, and J. Schmidt, “Impact of Hydrogen–Rich Silicon Nitride Material Properties on Light–Induced Lifetime Degradation in Multicrystalline Silicon,” *physica status solidi (RRL) – Rapid Research Letters*, vol. 31, p. 1900201, 2019.

[89] M. Kim, D. Chen, M. Abbott, S. Wenham, and B. Hallam, “Role of hydrogen: Formation and passivation of meta-stable defects due to hydrogen in silicon,” *AIP Conference Proceedings, Lausanne, Switzerland*, p. 130010, 2018.

[90] L. Helmich, D. C. Walter, D. Bredemeier, and J. Schmidt, "Atomic–Layer–Deposited Al2O3 as Effective Barrier against the Diffusion of Hydrogen from SiNx:H Layers into Crystalline Silicon during Rapid Thermal Annealing," *physica status solidi (RRL) – Rapid Research Letters*, vol. 14, no. 12, p. 2000367, 2020.

[91] W. Kwapil, J. Schon, T. Niewelt, and M. C. Schubert, "Temporary Recovery of the Defect Responsible for Light- and Elevated Temperature-Induced Degradation: Insights Into the Physical Mechanisms Behind LeTID," *IEEE Journal of Photovoltaics*, vol. 10, no. 6, pp. 1591–1603, 2020.

[92] T. H. Fung, C. E. Chan, B. J. Hallam, D. N. Payne, M. D. Abbott, and S. R. Wenham, "Impact of annealing on the formation and mitigation of carrier-induced defects in multi-crystalline silicon," *Energy Procedia*, vol. 124, pp. 726–733, 2017.

[93] T. Saitoh, X. Wang, H. Hashigami, T. Abe, T. Igarashi, S. W. Glunz, W. Wettling, A. Ebong, B. M. Damiani, A. Rohatgi, I. Yamasaki, T. Nunoi, H. Sawai, H. Ohtuka, Y. Yazawa, T. Warabisako, J. Zhao, and M. A. Green, "Light degradation and control of low-resistivity Cz-Si solar cells - an international joint research," *Technical Digest of the 11th International Photovoltaic Science and Engineering Conference, Sapporo, Japan*, pp. 553–556, 1999.

[94] F. Kersten, F. Fertig, K. Petter, B. Klöter, E. Herzog, M. B. Strobel, J. Heitmann, and J. W. Müller, "System performance loss due to LeTID," *Energy Procedia*, vol. 124, pp. 540–546, 2017.

[95] C. E. Chan, D. N. R. Payne, B. J. Hallam, M. D. Abbott, T. H. Fung, A. M. Wenham, B. S. Tjahjono, and S. R. Wenham, "Rapid Stabilization of High-Performance Multicrystalline P-type Silicon PERC Cells," *IEEE Journal of Photovoltaics*, vol. 6, no. 6, pp. 1473–1479, 2016.

[96] W. Kwapil, J. Dalke, T. Niewelt, and M. C. Schubert, "LeTID and (extended) BO-related degradation and regeneration in B- and Ga-doped monocrystalline silicon during dark and illuminated anneals," *Proceedings of the 37th EU PVSEC, WIP, Munich*, pp. 152–155, 2020.

[97] N. E. Grant, J. R. Scowcroft, A. I. Pointon, M. Al-Amin, P. P. Altermatt, and J. D. Murphy, "Lifetime instabilities in gallium doped monocrystalline PERC silicon solar cells," *Solar Energy Materials and Solar Cells*, vol. 206, p. 110299, 2020.

[98] N. E. Grant, P. P. Altermatt, T. Niewelt, R. Post, W. Kwapil, M. C. Schubert, and J. D. Murphy, "Gallium–Doped Silicon for High–Efficiency Commercial Passivated Emitter and Rear Solar Cells," *Solar RRL*, vol. 7, p. 2000754, 2021.

[99] F. Kersten, J. Heitmann, and J. W. Müller, "Influence of Al2O3 and SiNx Passivation Layers on LeTID," *Energy Procedia*, vol. 92, pp. 828–832, 2016.

[100] C. Vargas, K. Kim, G. Coletti, D. Payne, C. Chan, S. Wenham, and Z. Hameiri, “Carrier-Induced Degradation in Multicrystalline Silicon: Dependence on the Silicon Nitride Passivation Layer and Hydrogen Released During Firing,” *IEEE Journal of Photovoltaics*, vol. 8, no. 2, pp. 413–420, 2018.

[101] R. Eberle, W. Kwapil, F. Schindler, M. C. Schubert, and S. W. Glunz, “Impact of the firing temperature profile on light induced degradation of multicrystalline silicon,” *physica status solidi (RRL) - Rapid Research Letters*, vol. 10, no. 12, pp. 861–865, 2016.

[102] F. Maischner, S. Maus, J. Greulich, S. Lohmüller, E. Lohmüller, P. Saint-Cast, D. Ourinson, H. Vahlman, K. Hergert, S. Riepe, S. Glunz, and S. Rein, “LeTID mitigation via an adapted firing process in p–type PERC cells from SMART cast–monocrystalline, Czochralski and high–performance multicrystalline silicon,” *Progress in Photovoltaics: Research and Applications*, vol. 30, no. 2, pp. 123–131, 2022.

[103] L. Helmich, D. C. Walter, R. Falster, V. V. Voronkov, and J. Schmidt, “Impact of hydrogen on the boron-oxygen-related lifetime degradation and regeneration kinetics in crystalline silicon,” *Solar Energy Materials and Solar Cells*, vol. 232, p. 111340, 2021.

[104] A. van Wieringen and N. Warmoltz, “On the permeation of hydrogen and helium in single crystal silicon and germanium at elevated temperatures,” *Physica*, vol. 22, no. 6, pp. 849–865, 1956.

[105] M. J. Binns, S. A. McQuaid, R. C. Newman, and E. C. Lightowlers, “Hydrogen solubility in silicon and hydrogen defects present after quenching,” *Semicond. Sci. Technol.*, vol. 8, no. 10, pp. 1908–1911, 1993.

[106] S. Kleekajai, F. Jiang, M. Stavola, V. Yelundur, K. Nakayashiki, A. Rohatgi, G. Hahn, S. Seren, and J. Kalejs, “Concentration and penetration depth of H introduced into crystalline Si by hydrogenation methods used to fabricate solar cells,” *Journal of Applied Physics*, vol. 100, no. 9, p. 831, 2006.

[107] A. Hara, “Diffusion Coefficient of Hydrogen in Silicon at an Intermediate Temperature,” *Japanese Journal of Applied Physics*, vol. 46, no. 3A, pp. 962–964, 2007.

[108] B. Hammann, N. Aßmann, J. Schön, W. Kwapil, F. Schindler, S. Roder, E. V. Monakhov, and M. C. Schubert, “Understanding the impact of the cooling ramp of the fast-firing process on light- and elevated-temperature-induced degradation,” *Solar Energy Materials and Solar Cells*, vol. 259, p. 112462, 2023. [Online]. Available: https://www.sciencedirect.com/science/article/pii/S0927024823002830

[109] K. R. McIntosh and R. A. Sinton, “Uncertainty in photoconductance lifetime measurements that use an inductive-coil detector,” *Proceedings of the 23rd European Photovoltaic Solar Energy Conference and Exhibition, Valencia, Spain*, pp. 77–82, 2008.

[110] J. Hong, W. M. M. Kessels, W. J. Soppe, A. W. Weeber, W. M. Arnoldbik, and M. C. M. van de Sanden, “Influence of the high-temperature “firing” step on high-rate plasma deposited silicon nitride films used as bulk passivating antireflection coatings on silicon solar cells,” *Journal of Vacuum Science & Technology B: Microelectronics and Nanometer Structures*, vol. 21, no. 5, p. 2123, 2003.

[111] B. J. Hallam, S. R. Wenham, P. G. Hamer, M. D. Abbott, A. Sugianto, C. E. Chan, A. M. Wenham, M. G. Eadie, and G. Xu, “Hydrogen Passivation of B-O Defects in Czochralski Silicon,” *Energy Procedia*, vol. 38, no. 8, pp. 561–570, 2013.

[112] D. Chen, P. Hamer, M. Kim, C. Chan, A. Ciesla nee Wenham, F. Rougieux, Y. Zhang, M. Abbott, and B. Hallam, “Hydrogen-induced degradation: Explaining the mechanism behind light- and elevated temperature-induced degradation in n- and p-type silicon,” *Solar Energy Materials and Solar Cells*, vol. 207, p. 110353, 2020.

[113] V. V. Voronkov and R. Falster, “Formation, dissociation, and diffusion of various hydrogen dimers in silicon,” *physica status solidi (b)*, vol. 254, no. 6, p. 1600779, 2017.

[114] R. E. Pritchard, J. H. Tucker, R. C. Newman, and E. C. Lightowlers, “Hydrogen molecules in boron-doped crystalline silicon,” *Semiconductor Science and Technology*, vol. 14, no. 1, pp. 77–80, 1999.

[115] D. C. Walter, D. Bredemeier, R. Falster, V. V. Voronkov, and J. Schmidt, “Easy-to-apply methodology to measure the hydrogen concentration in boron-doped crystalline silicon,” *Solar Energy Materials and Solar Cells*, vol. 200, no. 1–4, p. 109970, 2019.

[116] J. Simon, A. Herguth, and G. Hahn, “Quantitative analysis of boron–hydrogen pair dynamics by infrared absorption measurements at room temperature,” *Journal of Applied Physics*, vol. 131, no. 23, p. 235703, 2022.

[117] Y. Acker, J. Simon, and A. Herguth, “Formation Dynamics of BH and GaH–Pairs in Crystalline Silicon during Dark Annealing,” *physica status solidi (a)*, vol. 219, no. 17, p. 2200142, 2022.

[118] J. Simon, A. Herguth, L. Kutschera, and G. Hahn, “The Dissociation of Gallium–Hydrogen Pairs in Crystalline Silicon during Illuminated Annealing,” *physica status solidi (RRL) – Rapid Research Letters*, vol. 124, p. 2200297, 2022.

[119] D. C. Walter, V. V. Voronkov, R. Falster, D. Bredemeier, and J. Schmidt, “On the kinetics of the exchange of hydrogen between hydrogen–boron pairs and hydrogen dimers in crystalline silicon,” *Journal of Applied Physics*, vol. 131, no. 16, p. 165702, 2022.

[120] A. R. Brown, M. Claybourn, R. Murray, P. S. Nandhra, R. C. Newman, and J. H. Tucker, “Enhanced thermal donor formation in silicon exposed to a hydrogen plasma,” *Semiconductor Science and Technology*, vol. 3, no. 6, pp. 591–593, 1988.

[121] H. J. Stein and S. K. Hahn, “Hydrogen–accelerated thermal donor formation in Czochralski silicon,” *Applied Physics Letters*, vol. 56, no. 1, pp. 63–65, 1990.

[122] H. J. Stein and S. Hahn, “Depth Profiles for Hydrogen–Enhanced Thermal Donor Formation in Silicon: Spreading Resistance Probe Measurements,” *Journal of The Electrochemical Society*, vol. 142, no. 4, pp. 1242–1247, 1995.

[123] E. Simoen, Y. L. Huang, Y. Ma, J. Lauwaert, P. Clauws, J. M. Rafí, A. Ulyashin, and C. Claeys, “What Do We Know about Hydrogen-Induced Thermal Donors in Silicon?” *Journal of The Electrochemical Society*, vol. 156, no. 6, p. H434, 2009.

[124] W. Götz, G. Pensl, W. Zulehner, R. C. Newman, and S. A. McQuaid, “Thermal donor formation and annihilation at temperatures above 500 °C in Czochralski-grown Si,” *Journal of Applied Physics*, vol. 84, no. 7, pp. 3561–3568, 1998.

[125] K. Torigoe and T. Ono, “Formation of thermal donor enhanced by oxygen precipitation in silicon crystal,” *AIP Advances*, vol. 10, no. 4, p. 045019, 2020.

[126] C. Vargas, G. Coletti, C. Chan, D. Payne, and Z. Hameiri, “On the impact of dark annealing and room temperature illumination on p-type multicrystalline silicon wafers: Solar Energy Materials and Solar Cells,” *Solar Energy Materials and Solar Cells*, vol. 189, pp. 166–174, 2019.

[127] S. Jafari and Z. Hameiri, “Investigation of Light-Induced Degradation in Ga- and In-Doped Cz Silicon,” in *2021 IEEE 48th Photovoltaic Specialists Conference (PVSC)*. IEEE, 20.06.2021 - 25.06.2021, pp. 0814–0817.

[128] D. Lin, Z. Hu, L. Song, D. Yang, and X. Yu, “Investigation on the light and elevated temperature induced degradation of gallium-doped Cz-Si,” *Solar Energy*, vol. 225, pp. 407–411, 2021.

[129] B. C. Reed, “Linear least–squares fits with errors in both coordinates,” *American Journal of Physics*, vol. 57, no. 7, pp. 642–646, 1989.

[130] Focuslight, “Data sheet of the Off-Axis Beam Shaping Module IOS000292,” 2022. [Online]. Available: https://www.focuslight.com/product/laser-optics-component/micro-lens-array-assembly/optical-module-assembly/off-axis-beam-shaper/

[131] B. Vicari Stefani, M. Kim, M. Wright, A. Soeriyadi, D. Andronikov, I. Nyapshaev, S. Abolmasov, K. Emtsev, A. Abramov, and B. Hallam, “Stability Study of Silicon Heterojunction Solar Cells Fabricated with Gallium– and Boron–Doped Silicon Wafers,” *Solar RRL*, vol. 228, p. 2100406, 2021.

[132] C. Chen, H. Wang, J. Wang, J. Lv, and H. Yang, “Performance degradation of commercial Ga–doped passivated emitter and rear cell solar modules in the field,” *Progress in Photovoltaics: Research and Applications*, vol. 30, no. 3, pp. 300–309, 2022.

[133] W. Kwapil, J. Dalke, R. Post, and T. Niewelt, “Influence of Dopant Elements on Degradation Phenomena in B– and Ga–Doped Czochralski–Grown Silicon,” *Solar RRL*, vol. 5, no. 5, p. 2100147, 2021.

[134] G. R. Wolstenholme, N. Jorgensen, P. Ashburn, and G. R. Booker, “An investigation of the thermal stability of the interfacial oxide in polycrystalline silicon emitter bipolar transistors by comparing device results with high-resolution electron microscopy observations,” *Journal of Applied Physics*, vol. 61, no. 1, pp. 225–233, 1987.

[135] J. C. Bravman, G. L. Patton, and J. D. Plummer, “Structure and morphology of polycrystalline silicon-single crystal silicon interfaces,” *Journal of Applied Physics*, vol. 57, no. 8, pp. 2779–2782, 1985.

[136] T. Maeda, M. Higashizono, H. Momose, and J. Matsunaga, “Poly Si-Si interfacial oxide ball-up mechanism and its control for 0.8 mu m BiCMOS VLSIs,” in *Proceedings of the Bipolar Circuits and Technology Meeting.* IEEE, 18-19 Sept. 1989, pp. 102–105.

[137] R. A. Sinton and A. Cuevas, “A quasi-steady-state open-ciruit voltage method for solar cell characterizsation,” *Proceedings of the 16th EU PVSEC, Glasgow, UK*, pp. 1152–1155, 2000.

[138] M. Wolf and H. Rauschenbach, “Series resistance effects on solar cell measurements,” *Advanced Energy Conversion*, vol. 3, pp. 455–479, 1963.

[139] D. Sperber, A. Herguth, and G. Hahn, “On improved passivation stability on highly-doped crystalline silicon and the long-term stability of regenerated Cz-Si,” *Solar Energy Materials and Solar Cells*, vol. 185, pp. 277–282, 2018.

[140] M. Winter, S. Bordihn, R. Peibst, R. Brendel, and J. Schmidt, “Degradation and Regeneration of n+ -Doped Poly-Si Surface Passivation on p-Type and n-Type Cz-Si Under Illumination and Dark Annealing,” *IEEE Journal of Photovoltaics*, vol. 10, no. 2, pp. 423–430, 2020.

[141] M. A. Green, “General temperature dependence of solar cell performance and implications for device modelling,” *Progress in Photovoltaics: Research and Applications*, vol. 11, no. 5, pp. 333–340, 2003.

[142] J. Krügener, F. Haase, M. Rienäcker, R. Brendel, H. Osten, and R. Peibst, “Improvement of the SRH bulk lifetime upon formation of n-type POLO junctions for 25% efficient Si solar cells,” *Solar Energy Materials and Solar Cells*, vol. 173, pp. 85–91, 2017.

[143] M. Hayes, B. Martel, G. W. Alam, H. Lignier, S. Dubois, E. Pihan, and O. Palais, “Impurity Gettering by Boron– and Phosphorus–Doped Polysilicon

Passivating Contacts for High–Efficiency Multicrystalline Silicon Solar Cells," *physica status solidi (a)*, vol. 216, no. 17, p. 1, 2019.

[144] Z. Wang, Z. Liu, M. Liao, D. Huang, X. Guo, Z. Rui, Q. Yang, W. Guo, J. Sheng, C. Shou, B. Yan, Z. Yuan, Y. Zeng, and J. Ye, "Effective gettering of in-situ phosphorus-doped polysilicon passivating contact prepared using plasma-enhanced chemical-vapor deposition technique," *Solar Energy Materials and Solar Cells*, vol. 206, p. 110256, 2020.

[145] A. Liu, Z. Yang, F. Feldmann, J.-I. Polzin, B. Steinhauser, S. P. Phang, and D. Macdonald, "Understanding the impurity gettering effect of polysilicon/oxide passivating contact structures through experiment and simulation," *Solar Energy Materials and Solar Cells*, vol. 230, no. 5, p. 111254, 2021.

[146] L. Song, Z. Hu, L. Fang, Y. Cai, S. He, H. Huang, W. Hsu, X. Yu, and D. Yang, "Performance Improvement of Gallium–Doped Passivated Emitter and Rear Cells by Two–Step Bias Application," *Solar RRL*, vol. 5, no. 12, p. 2100738, 2021.

[147] F. Haase, C. Hollemann, S. Schäfer, A. Merkle, M. Rienäcker, J. Krügener, R. Brendel, and R. Peibst, "Laser contact openings for local poly-Si-metal contacts enabling 26.1%-efficient POLO-IBC solar cells," *Solar Energy Materials and Solar Cells*, vol. 186, pp. 184–193, 2018.

[148] A. Richter, J. Benick, F. Feldmann, A. Fell, M. Hermle, and S. W. Glunz, "n-Type Si solar cells with passivating electron contact: Identifying sources for efficiency limitations by wafer thickness and resistivity variation," *Solar Energy Materials and Solar Cells*, vol. 173, pp. 96–105, 2017.

[149] A. Ingenito, G. Nogay, Q. Jeangros, E. Rucavado, C. Allebé, S. Eswara, N. Valle, T. Wirtz, J. Horzel, T. Koida, M. Morales-Masis, M. Despeisse, F.-J. Haug, P. Löper, and C. Ballif, "A passivating contact for silicon solar cells formed during a single firing thermal annealing," *Nature Energy*, vol. 3, no. 9, pp. 800–808, 2018.

[150] A. Merkle, S. Seren, H. Knauss, B. Min, J. Steffens, B. Terheiden, R. Brendel, and R. Peibst, "Atmospheric Pressure Chemical Vapor Deposition of In-Situ Doped Amorphous Silicon Layers for Passivating Contacts: 7 pages / 35th European Photovoltaic Solar Energy Conference and Exhibition; 785-791," *Proceedings of the 35th European Photovoltaic Solar Energy Conference and Exhibition*, pp. 785–791, 2018.

[151] Y. Yang, P. P. Altermatt, Y. Cui, Y. Hu, D. Chen, L. Chen, G. Xu, X. Zhang, Y. Chen, P. Hamer, R. S. Bonilla, Z. Feng, and P. J. Verlinden, "Effect of carrier-induced hydrogenation on the passivation of the poly-Si/SiOx/c-Si interface," *AIP Conference Proceedings 1999*, p. 040026, 2018.

[152] B. Nemeth, D. L. Young, M. R. Page, V. LaSalvia, S. Johnston, R. Reedy, and P. Stradins, "Polycrystalline silicon passivated tunneling contacts for high efficiency silicon solar cells," *Journal of Materials Research*, vol. 31, no. 6, pp. 671–681, 2016.

[153] A. Mewe, M. Stodolny, J. Anker, M. Lenes, X. Pagès, Y. Wu, K. Tool, B. Geerligs, and I. Romijn, "Full wafer size IBC cell with polysilicon passivating contacts," *AIP Conference Proceedings, Lausanne, Switzerland*, pp. pp. 040 014–1–040 014–4, 2018.

[154] R. Peibst, U. Römer, K. R. Hofmann, B. Lim, T. F. Wietler, J. Krügener, N.-P. Harder, and R. Brendel, "A Simple Model Describing the Symmetric I-V Characteristics of p Polycrystalline Si/n Monocrystalline Si, and n Polycrystalline Si/p Monocrystalline Si Junctions," *IEEE Journal of Photovoltaics*, vol. 4, no. 3, pp. 841–850, 2014.

[155] H. Fischer and W. Pschunder, "Investigation of photon and thermal induced changes in silicon solar cells," *10th IEEE Photovoltaic Specialists Conference*, pp. 404–4011, 1973.

[156] A. Y. Liu and D. Macdonald, "Impurity gettering effect of atomic layer deposited aluminium oxide films on silicon wafers," *Applied Physics Letters*, vol. 110, no. 19, p. 191604, 2017.

[157] C. Gemmel, J. Hensen, N. Folchert, F. Haase, R. Peibst, S. Kajari-Schröder, and R. Brendel, "9 ms carrier lifetime in kerfless epitaxial wafers by n-type POLO gettering," *AIP Conference Proceedings, Lausanne, Switzerland*, pp. pp. 130 005–1–130 005–7, 2018.

List of Publications

Publications arising from the work in this thesis:

Peer-reviewed Journal Papers

1. M. Winter, D. Walter, D. Bredemeier, and J. Schmidt, “Light-induced lifetime degradation effects at elevated temperature in Czochralski-grown silicon beyond boron-oxygen-related degradation”, Solar Energy Materials and Solar Cells, vol. 201, p. 110060, 2019.
2. M. Winter, S. Bordihn, R. Peibst, R. Brendel, and J. Schmidt, “Degradation and Regeneration of n^+-Doped Poly-Si Surface Passivation on p-Type and n-Type Cz-Si Under Illumination and Dark Annealing”, IEEE Journal of Photovoltaics, vol. 10, no. 2, pp. 423–430, 2020.
3. M. Winter, D. C. Walter, and J. Schmidt, “Carrier Lifetime Degradation and Regeneration in Gallium- and Boron-Doped Monocrystalline Silicon Materials”, IEEE Journal of Photovoltaics, vol. 11, no. 4, pp. 866–872, 2021.
4. M. Winter, D. C. Walter, B. Min, R. Peibst, R. Brendel, and J. Schmidt, “Light and elevated temperature induced degradation and recovery of gallium-doped Czochralski-silicon solar cells”, Scientific Reports, vol. 12, p. 8089, 2022.
5. M. Winter, D. C. Walter, and J. Schmidt, “Impact of Fast-Firing Conditions on Light- and Elevated-Temperature-Induced Degradation (LeTID) in Ga-Doped Cz-Si”, IEEE Journal of Photovoltaics, vol. 13, no. 6, pp. 849–857, 2023.

Conference Proceedings

1. M. Winter, L. Helmich, D. C. Walter, and J. Schmidt, “Firing-triggered LID (FT-LID) of the carrier lifetime in Cz-Si”, Proceedings of the 37th EU PVSEC, WIP, Munich, pp. 462–467, 2020.

List of Figures

List of Tables

Abbreviations

Acronym	Description
Al-BSF	Aluminum back surface field
ALD	Atomic layer deposition
AM1.5G	Air mass 1.5 global spectrum
a-Si	Amorphous silicon
BJ	Backjunction
BO	Boron-oxygen
Cz-Si	Czochralski-grown silicon
Cz-Si:B	Boron-doped Cz-Si
Cz-Si:Ga	Gallium-doped Cz-Si
DA	Dark anneal
FeB	Iron-boron
FT	Measured peak firing temperature
FZ-Si	Float-zone silicon
FZ-Si:B	Boron-doped FZ-Si
HT	High-temperature
IV	Current-voltage
LeTID	Light- and elevated-temperature-induced degradation
LID	Light induced degradation
LPCVD	Low-pressure chemical vapor deposition
mc-Si	Multicrystalline silicon
mc-Si:B	Boron-doped mc-Si
mono-Si	Monocrystalline silicon
MPP	Maximum power point
PCD	Photoconductance decay
PECVD	Plasma-enhanced chemical vapor deposition
PERC	Passivated emitter and rear cell
PL	Photoluminescence
POLO	Polycrystalline silicon on oxide
Poly-Si	Polycrystalline silicon
PV	Photovoltaic
QSSPC	Quasi steady-state photoconductance
RCA	Wet-chemical cleaning process
RF	Radio frequency
RTA	Rapid thermal annealing
Si CCD	Silicon charge-coupled device
SRH	Shockley-Read-Hall
SSPC	Steady-state photoconductance

Arabic symbols

Symbol	Description	Unit
B_{rad}	Coefficient of radiative recombination	$\mathrm{cm^3\,s^{-1}}$
C_{n}, C_{p}	Coefficients of Auger recombination for electrons/holes	$\mathrm{cm^6\,s^{-1}}$
C^*_{n}, C^*_{p}	Coefficients of Auger recombination for electrons/holes with Coulomb interaction	$\mathrm{cm^6\,s^{-1}}$
C_{ϑ}	Temperature coefficient for resistivity	$\mathrm{°C^{-1}}$
D	Diffusion constant of excess carriers	$\mathrm{cm^2\,s^{-1}}$
e	Elementary charge	C
E_{A}	Activation energy	eV
E_{c}, E_{v}	Energy of the conduction/valence band edge	eV
E_{g}	Silicon band gap energy	eV
E_{t}	Defect energy level	eV
FF	Fill factor	%
FF_{sh}	Fill factor determined with negligible series but non-negligible shunt resistance	%
FF_0	Ideal fill factor value	%
FT	Measured peak firing temperature	°C
G	Generation rate	$\mathrm{cm^{-3}\,s^{-1}}$
g_{eeh}, g_{ehh}	Enhancement factors of Coulomb interaction for electrons/holes	-
G_{th}	Thermal generation rate	$\mathrm{cm^{-3}\,s^{-1}}$
h	Planck constant	eV s
I_{ill}	Illumination intensity	suns
I_{PL}	PL signal intensity	cts/s
J	Current density	$\mathrm{mA/cm^2}$
J_{L}	Light-generated current density	$\mathrm{mA/cm^2}$
J_{sc}	Short-circuit current density	$\mathrm{mA/cm^2}$
$J_{\mathrm{sc,1sun}}$	Short-circuit current density under one-sun illumination	$\mathrm{A/(cm^2\,sun)}$
J_0	Saturation current density	$\mathrm{fA/cm^2}$
k_{B}	Boltzmann constant	eV/K
n	Total electron concentration	$\mathrm{cm^{-3}}$
n	Refractive index	-
n_1, n_2	Shockley-Read-Hall densities	$\mathrm{cm^{-3}}$
N_{c}, N_{v}	Effective density of states in conduction/valence band	$\mathrm{cm^{-3}}$
N^*_{d}	Effective defect concentration	$\mathrm{µs^{-1}}$
N_{dop}	Doping concentration	$\mathrm{cm^{-3}}$

Symbol	Description	Unit
n_{ideal}	Ideality factor	-
N^*_{max}	Maximum effective defect concentration	μs^{-1}
N_{t}	Concentration of defect/recombination centers	cm^{-3}
n^+	Highly phosphorus-doped layer	-
n_0	Electron concentration in thermal equilibrium	cm^{-3}
n_{i}	Intrinsic carrier concentration	cm^{-3}
p	Total hole concentration	cm^{-3}
P_{in}	Power of the incident light	W/cm^2
P_{MPP}	Power at the maximum power point	W/cm^2
p_0	Hole concentration in thermal equilibrium	cm^{-3}
pFF	Pseudo fill factor	%
Q	Capture time constant ratio	-
R_{808}	Reflectivity at a laser wavelength of 808 nm	-
R_{de}	Deactivation rate constant	h^{-1}
R_{deg}	Degradation rate constant	h^{-1}
R_{reg}	Regeneration rate constant	h^{-1}
R_{s}	Series resistance	$\Omega\,\text{cm}^2$
R_{sh}	Shunt resistance	$\Omega\,\text{cm}^2$
s	Scale factor to subsume the Δn-dependence of degradation and regeneration rate constants	-
S	Surface recombination velocity	cm/s
t	Time	s, h
T	Absolute temperature	K
T	Cell temperature during current-voltage measurement	°C
T	Measured temperature on the silicon wafer surface during fast-firing	°C
T_{eff}	Effective transmission	-
U	Net recombination rate	$\text{cm}^{-3}\,\text{s}^{-1}$
U_{Auger}	Rate of Auger recombination	$\text{cm}^{-3}\,\text{s}^{-1}$
U_{intr}	Rate of intrinsic recombination	$\text{cm}^{-3}\,\text{s}^{-1}$
U_{rad}	Rate of radiative recombination	$\text{cm}^{-3}\,\text{s}^{-1}$
U_{tot}	Total recombination rate	$\text{cm}^{-3}\,\text{s}^{-1}$
V	Voltage	mV
v_{band}	Band velocity of the firing furnace	m/min
V_{oc}	Open-circuit voltage	mV
v_{oc}	Open-circuit voltage normalized to the thermal voltage	-
v_{th}	Thermal carrier velocity	cm/s
W	Wafer thickness	µm

Greek symbols

Symbol	Description	Unit
Δn	Excess carrier concentration	$\mathrm{cm^{-3}}$
$\Delta\sigma$	Photoconductance generated by flash lamp	Ω^{-1}
η	Energy conversion efficiency	%
ϑ	Temperature during illumination	°C
$\vartheta_{\mathrm{meas}}$	Measurement temperature	°C
μ_{n}, μ_{p}	Electron/hole mobility	$\mathrm{cm^2\,V^{-1}\,s^{-1}}$
ν	Frequency	$\mathrm{s^{-1}}$
ρ	Resistivity	$\Omega\,\mathrm{cm}$
ρ_{meas}	Measured resistivity	$\Omega\,\mathrm{cm}$
$\rho_{25\,^{\circ}\mathrm{C}}$	Resistivity at 25 °C	$\Omega\,\mathrm{cm}$
σ	Conductance	Ω^{-1}
σ_{p}, σ_{n}	Capture cross sections for holes/electrons	$\mathrm{cm^2}$
σ_0	Photoconductance in the dark	Ω^{-1}
τ_{Auger}	Carrier lifetime of Auger recombination	ms
τ_{d}	Lifetime in the activated defect state	µs
τ_{eff}	Effective carrier lifetime	µs, ms
τ_{intr}	Carrier lifetime of intrinsic recombination	ms
τ_{p0}, τ_{n0}	Capture time constants for holes/electrons	ms
τ_{rad}	Carrier lifetime of radiative recombination	ms
τ_{SRH}	SRH lifetime	ms
$\tau_{\mathrm{SRH,def}}$	SRH lifetime of the activated defect	µs
τ_{surf}	Carrier lifetime of surface-related recombination	ms
τ_0	Lifetime in the deactivated defect state	µs
Φ	Photon flux	$\mathrm{cm^{-2}\,s^{-1}}$

Chemical formula

Formula	**Compound**
Ag	Silver
Al	Aluminum
AlO_x	Aluminum oxide
H_2	Hydrogen dimer
HB	Hydrogen-boron pair
HF	Hydrogen fluoride
KOH	Potassium hydroxide
Si	Silicon
SiN_y	Silicon nitride
SiN_y:H	Hydrogen-rich/hydrogenated silicon nitride
SiO_2	Silicon oxide
SiO_y	Silicon oxide

Danksagung

Abschließend möchte ich mich bei allen bedanken, die zum Gelingen dieser Arbeit beigetragen haben:

Prof. Dr. Jan Schmidt für eine sehr gute und intensive wissenschaftliche Betreuung mit überaus lehrreichen Diskussionen im Rahmen von Experimenten und Hilfe beim Erstellen wissenschaftlicher Publikationen,

Prof. Dr. Tobias Wietler und **Prof. Dr. Michael Seibt** für die bereitwillige Übernahme der Korreferate und

Prof. Dr. Holger Frahm für die Übernahme des Vorsitzes der Promotionskommission.

Ein besonderer Dank gilt außerdem **Dr. Dominic C. Walter** und **Dr. Lailah Helmich** für die hilfreichen Diskussionen und Anregungen, sowohl für die Anfertigung von Veröffentlichungen als auch für das experimentelle Arbeiten.

Ebenso möchte ich mich bei **Conny Marquardt** für die tolle Unterstützung bei der Probenprozessierung bedanken, seien es die Reinigungen, die Diffusionen oder die Oberflächenpassivierung von Wafern auf dem Weg zu Lebensdauerproben gewesen.

Außerdem möchte ich mich bei allen **KollegInnen am ISFH** bedanken für die außergewöhnlich kollegiale angenehme Arbeitsatmosphäre und die Unterstützung beim experimentellen Arbeiten, insbesondere der Gruppe „Materialforschung“.

Nicht zuletzt gilt mein besonderer Dank meiner **Familie**, die mich während meines Studiums immer großartig unterstützt hat.

Curriculum vitae

Persönliche Daten

Name	Michael Winter
Anschrift	Heinrichstr. 14 31785 Hameln
Geburtsdaten	27. November 1990 in Hildesheim

Anstellung

seit 01/2018	Wissenschaftlicher Mitarbeiter im Rahmen eines Promotionsstudiums Institut für Solarenergieforschung Hameln (ISFH) Abteilung: Photovoltaik, Arbeitsgruppe: Materialforschung

Studium

2018–2023	Promotionsstudium Physik, Leibniz Universität Hannover Promotionsarbeit am Institut für Festköperphysik
2014–2017	Masterstudiengang Physik, Leibniz Universität Hannover Masterarbeit am Albert-Einstein-Institut Hannover
2011–2014	Bachelorstudiengang Physik, Leibniz Universität Hannover Bachelorarbeit am Albert-Einstein-Institut Hannover

Zivildienst

2010–2011	CJD Jugendhilfeverbund Elze

Schulbildung

2001–2010	Gymnasium CJD Elze, Abschluss: Abitur
1997–2001	Astrid-Lindgren-Grundschule Elze